SYNTHESIS AND CHARACTERIZATION OF Bi_2O_3 NANO-POWDER PRODUCED BY MICROWAVE ASSISTED COMBUSTION METHOD (MWC)

BY

ABDULMAJEED HASAN YAHYA HENDI

A Thesis Presented to the
DEANSHIP OF GRADUATE STUDIES

KING FAHD UNIVERSITY OF PETROLEUM & MINERALS
DHAHRAN, SAUDI ARABIA

In Partial Fulfillment of the
Requirements for the Degree of

MASTER OF SCIENCE

In

PHYSICS

April, 2012

KING FAHD UNIVERSITY OF PETROLEUM & MINERALS
DHAHRAN 31261, SAUDI ARABIA

DEANSHIP OF GRADUATE STUDIES

This thesis, written by **ABDULMAJEED HASAN YAHYA HENDI** under the direction of his thesis advisor and approved by his thesis committee, has been presented to and accepted by the Dean of Graduate Studies, in partial fulfillment of the requirements for the degree of **MASTER OF SCIENCE IN PHYSICS**.

Thesis Committee

Thesis Advisor
Dr. Saleh I. Al-Quraishi

Member
Dr. Zain H. Yamani

Member
Prof. Khalil A. Ziq

Member
Prof. Mohammed F. Al-Kuhaili

M. A. Gondal
Member
Prof. Mohammad A. Gondal

Department Chairman
Dr. Abdul-Aziz Al-Jalal

Dean of Graduate Studies
Dr. Salam A. Zummo

19/5/12
Date

DEDICATED

_TO_

To my beloved parents, lovely wife and daughters who are behind my happiness and success

ACKNOWLEDGMENT

All thanks and praise are due to Allah (azzawajal) who created me, blessed me with health, as well as provided me with patience and ambition to achieve this research.

I acknowledge deeply my thesis advisor Dr. Saleh I. Al-Quraishi who guided me in this research. I actually learned from him patience, insistence, and repetition of efforts. The long hours we spent together in his lab searching for results about my research will not be forgotten. I shall remain grateful for him forever, I pray to Allah for his success and happiness in his whole life.

I would like to extend my thanks to my thesis committee, including Dr. Zain Yamani, the director of Center of Research Excellence in Nanotechnology (CENT) for his cooperation, encouragement, feedback and continuous support; Prof. Khalil Ziq who kept his lab open and allowed me to use the facilities all the time. His great and useful discussions related to my research proved all the time fruitful; Prof. Mohammad Al-Kuhaili, for his continuous advices and beneficial discussions as well as for providing me with access to the facilities available in his laboratory and Prof. Mohammad A. Gondal who was always concerned with progress and followed my whole research work. His strong encouragement during my work is also greatly appreciated.

Thanks are extended to Dr. Abbas Hakeem for carrying out the FESEM analysis, Mr. Mohammad Saeed for carrying out the XRD and XPS measurements and Mr. Mohammad Dastageer who executed the UV-visible measurements.

I also wish to express my gratitude and thanks to my teachers Dr. F. Z. Khiari, Dr. M. S. Musazay, for the nice discussions with them in different topics related to my work and their encouragement.

I owe a debt of gratitude to Physics Department, and the chairman Dr. Abdul-Aziz Al-Jalal for his encouragement.

No words can thank my colleagues Qasem Drmoosh, Esam Al- Nahari, Mojeeb Al-Rhman Al-Khiaty, Adnan Mahdi, Amran Al-Aghbari, Faez Al-Qarni and Mohammed Dhan Qasem for their unlimited help, encouragement and support.

The support and prayers of all my friends in Yemen specially Mr. Hasan Mawaz, Dr. Yahya Jarad, Mr. Ali Ergan, Mr. Khaled Webri, Mr. Naser Al-A'asemi, and Mr. M. Al-Saeedi are deeply appreciated .

Finally, I can't express the amount of gratitude and indebtedness that I feel, from all of the tremendous love, prayers and support that I have received from my parents, my loving wife, my darling daughters, my brothers (especially my brother Hafez), and all my sisters.

TABLE OF CONTENTS

LIST OF FIGURES

LIST OF TABLES

ABSTRACT

Name: **Abdulmajeed Hasan Yahya Hendi**

Title: **Synthesis and Characterization of Bi_2O_3 Nano-Powder Produced by Microwave Assisted Combustion Method (MWC)**

Major Field: **Physics**

Date of degree: **April, 2012**

In this study, Bi_2O_3 nano-powders were synthesized using microwave assisted combustion method (MWC). A microwave setup was modified along with fabrication of specially designed SiC composite microwave heater (susceptor) which was used to evaporate metal bismuth and oxidize it in the ambient atmosphere of the microwave cavity. We have investigated the effect of three different experimental parameters; synthesis temperature, carrier gases namely - nitrogen, argon and helium - and their flow rates on the structural, optical, morphological and chemical properties of the as-synthesized bismuth oxide nano-powders. Using the MWC method, we are able to decrease the size of the nanoparticles with controlling the flow rate of the carrier gas and the synthesis temperature. The X-ray diffraction (XRD) analysis suggests that all the as-synthesized samples were of polycrystalline α and β phases of Bi_2O_3 with predominance of β-phase. It was observed that the concentration of each phase varied with the synthesis temperatures. For samples synthesized with N_2 as carrier gas, the average grain size was in the range of 19 - 86 nm while those synthesized with Ar and He as carrier gases were having average size in the range of 25 - 175 nm and 18 - 133 nm, respectively. The direct band gap values of the samples were found to increase with the increase of the range of flow rates of the carrier gases due to the decrease in the grain size. These values were in the range of 3.38 - 3.67 eV when N_2 was used as carrier gas. However, in the case of Ar and He, they were in the range of 3.29 - 3.65 e V and 3.25 - 3.64 eV, respectively.

The morphology of the as-synthesized Bi_2O_3 powders was investigated by field emission scanning electron microscopy (FESEM) that revealed the formation of plate-like Bi_2O_3 particles at fixed synthesis temperature and different flow rates of the carrier gases. The energy dispersion X-ray spectroscopy (EDS) analysis confirmed the purity of the product which contains only Bi and O. The oxidation state was investigated by the X-ray photoelectron spectroscopy (XPS) that confirmed the formation of Bi_2O_3. The binding energies of the examined samples components were found to be close to each other suggesting no remarkable shift with the variation of the type and flow rates of the carrier gas.

ملخص الرسالة

الاســــــم: **عبدالمجيد حسن يحي هندي**

عنوان الرسالة: ***إنتاج وفحص أكسيد البزموث ذو البنية النانوية بواسطة الإحتراق بمساعدة الميكرويف***

التخصـــــص: **فيزياء**

تاريخ التخــرج: **إبريل 2012م**

في هذه الدراسة، تم إنتاج أكسيد البزموث ذو البنية النانونية باستخدام طريقة الاحتراق بالميكرويف. و للقيام بذلك، تم تعديل جهاز الميكرويف المستخدم في المنازل وكذلك تصميم مسخَّن من مادة كربيد السيليكون (SiC) يسمى الماصّ (susceptor). حيث تم تبخير معدن البزموث داخل الماص، و الذي له قدرة عالية على امتصاص طاقة الميكرويف و تحويلها إلى حرارة لتسخين المعدن إلى درجة حرارة عالية فيتبخر و يحترق عند خروجه من الماصّ و ملامسته للهواء الموجود في فجوة الميكرويف مكونا أكسيد البزموث (Bi_2O_3).

بعد ذلك، قمنا بفحص و دراسة تأثير ثلاثة متغيرات تجريبية مختلفة على هيئة و شكل الجسيمات النانونية المنتجة بهذه الطريقة، و على خواصها البصرية و الكيميائية. هذه المتغيرات التجريبية هي حرارة الإنتاج وثلاثة غازات حاملة (النيتروجين و الأرجون و الهيليوم) و معدل تدفق كل غاز من هذه الغازات الحاملة. لقد وجدنا أننا باستخدام طاقة الميكرويف قادرين على إنقاص حجم الجسيمات النانوية المنتجة من خلال التحكم بنوع الغاز و معدل تدفق الغاز الحامل و حرارة الإنتاج.

تم استخدام جهاز الحيود السيني (XRD) لدراسة البنية البلورية للأكسيد (Bi_2O_3)، حيث أثبتت نتيجة الفحص ان الأكسيد المنتج عبارة عن أكسيد عديد التبلور في حالتين أو طورين مختلفين هما: الطور الأول (β-Bi_2O_3) و الطور الثاني (α-Bi_2O_3) مع هيمنة الطور الأول (β-Bi_2O_3). كما لاحظنا أن تركيز كل طور يتغير مع تغير درجة حرارة الإنتاج.

العينات المنتجة من أكسيد البزموث ذات البنية النانونية كانت في المعدل من 19– 86 نانومتر عند استخدام النيتروجين كغاز حامل، بينما عند استخدام الأرجون كغاز حامل كان متوسط السمك بين 25– 175 نانومتر ، و من 18 – 133 نانومتر عند استخدام الهيليوم كغاز حامل.

وجدنا أن قيم فجوة الطاقة المباشرة للعينات المنتجة من الأكسيد تتزايد مع زيادة تدفق الغازات الحاملة، و ذلك بسبب نقصان سمك الجسيمات النانونية. حيث وجدنا أنها في المدى 3.38– 3.67 إلكترون فولت في حالة استخدام النيتروجين كغاز حامل، بينما كانت تتراوح من 3.29– 3.65 إلكترون فولت في حالة الأرجون و من 3.25– 3.64 إلكترون فولت في حالة الهيليوم .

كما تم فحص شكل العينات المنتجة عند درجة حرارة ثابتة و معدل تدفقات مختلفة للغازات الحاملة باستخدام الميكروسكوب الإلكتروني الماسح الذي يعمل وفق مبدأ إنبعاث للمجال الكهربائي (FESEM)، حيث أظهر الفحص أن المنتج عبارة عن جسيمات على شكل صفائح.

تم التأكد من نقاوة المنتج باستخدام جهاز مطياف تشتيت طاقة الأشعة السينية (EDS) حيث وجد أن الأكسيد المنتج يتكون من بزموث و أكسجين فقط. أما حالة الأكسدة فقد درست بإستخدام مطياف الأشعة السينية الإلكتروضوئي (XPS)، و الذي أكد لنا تشكُّل أكسيد البزموث (Bi_2O_3)، بالإضافة إلى عدم وجود تأثير يذكرعلى طاقات الربط لمكونات الأكسيد مع تغير نوع و مقدار تدفقات الغازات الحاملة عند درجة حرارة إنتاج ثابتة، حيث وجدنا أن طاقات الربط لمكونات الأكسيد متقاربة جدا في القيمة.

CHAPTER 1

INTRODUCTION

1.1. Nanomaterials: an overview

A nanometer, labled nm, is one billionth of a meter, or 10^{-9} m. One nanometer is the length equivalent of about five silicon or ten hydrogen atoms aligned in a line. Nanomaterials are defined as materials on a size scale of approximately 1 to 100 nm. Nanotechnology includes the area of synthesis, characterization, production and application of structures, devices and systems by controlling shape and size at the nanometer scale.

In 1959, Physicist Richard Feynman delivered a lecture titled "There's Plenty of Room at the Bottom" describing a process for fabricating the materials by manipulating individual atoms [1]. In 1974, Professor Norio Taniguchi of Tokyo Science University, defined for the first time the term of "nanotechnology" as follows: "Nano-technology mainly consists of the processing, separation, consolidation, and deformation of materials by one atom or by one molecule" [2]. The basic idea of the nanotechnology definition was explored in depth by Dr. K. Eric Drexler in the 1980s. Eric, through his books "Engines of Creation": The Coming Era of Nanotechnology (1986) and Nanosystems*:* Molecular Machinery, Manufacturing, and Computation, promoted the technological significance of nano-scale phenomena and devices [3]. The invention of scanning tunnel microscopy (STM) in 1981, and the atomic force microscopy (AFM) presented the starting point of practical nanotechnology.

Nanomaterials have unique properties that are significantly different from those of corresponding bulk materials such as high surface energy, large proportion of surface atoms, i.e. a high surface-to-volume ratio, and reduced imperfections [4]. The high surface-to-volume ratio with size effects make nanomaterials exhibit many unique physical, chemical, mechanical, magnetic, and optical properties. For example, the melting point of gold has been found to be reduced as a function of decreasing particle size [5]. The hardness of spherical silicon nanoparticles is approximately four times greater than the corresponding bulk material [6]. It was also found that the thermal conductivity of fluids increases by mixing very small concentrations of nanoparticles. For example, by suspending copper oxide nanocrystalline in fluids such as deionized water and oil, the thermal conductivity of the particle-fluid mixtures was enhanced by 60% compared to fluids without nanoparticles [7]. In absorption of light by bulk metals the visible part of the spectrum doesn't contain absorption peaks that are seen in the spectra of nanometal films [8].

Nanomaterials can be classified into four types: zero dimension (clusters), one dimension (nanotubes and nanorods), two dimension (films) or in three dimension (polycrystals materials) [8].

1.2. Synthesis methods of nanomaterials

The growing use of nanomaterials in a wide variety of different applications requires the development of synthesis methods of nanoparticles by various techniques. Basically, these methods can be grouped into four categories: mechanical methods, wet chemical methods, form-in-place methods and gas phase synthesis [9].

1.2.1. Mechanical methods

In these methods bulk materials can be mechanically broken down into smaller particles. The basic idea of these techniques can be summarized as follows: powder with mean size from 200 to 5 nm can be produced by grinding the material of interest in grinding equipment - such as horizontally rotating cylinder - along with hard steel or tungsten carbide ball [8]. These techniques are simple with low-cost equipments. However, they produce particles with a broad size distribution and contamination from the milling machinery is often a problem.

1.2.2. Form-in-place methods

These methods include, spray coatings, chemical vapor deposition and physical vapor deposition. Nanocrystalline layers and thin films can be produced via these techniques.

Spray coating is a process for coating a surface with a liquid spray of fluid. In this process, a fine aerosol is produced by forcing the fluid through a small nozzle. A carrier gas is used in directing the aerosol at the surface to be coated [10].

Chemical vapor deposition (CVD) is a process in which a chemical reaction transforms gas phase precursor into solid material that can be deposited on a substrate in the form of a thin solid film [11]. Due to the chemical reaction conditions such as operating pressure, CVD processes can be grouped into: CVD processes at atmospheric pressure, CVD processes at low pressure and CVD processes at very low pressure. The advantages of this method include producing uniform and reproducible films at low or high rates [12].

Physical vapor deposition is a process of transforming a material (source) into a vapor and deposits it on a substrate. In this method the thickness of the deposited material can vary from angstrom to millimeters. Generally, this method can be classified into two groups: evaporation in which the deposited material is removed from the source by thermal means, and sputtering that involves gaseous ions (plasma) to remove atoms or molecules from solid target [4].

1.2.3. Wet chemical methods

These methods include chemical reduction, sol-gel, and chemical precipitation. Basically, these processes can be achieved by mixing different ionic solutions in well defined quantities. Controlling heat and pressure, insoluble compounds can be formed and precipitate out of the solution. The precipitates are collected by means of filters to produce a dry powder. One of the benefits of these methods is fabrication of a large variety of compounds including some metals. In addition, size and morphology can be controlled by varying species and synthetic conditions.

In chemical reduction process, nano-scale metals can be produced by reducing metallic salts or acids using reducing agent such as alkaline borohydride. The choice of a reducing agent depends on the chemical reactivity of the metal. This method has been used in preparing bismuth and bismuth oxide nanoparticles [13].

Sol-gel processing has also been extensively used for synthesizing nanomaterials. This technique involves the transition of a system from liquid (sol) into a solid phase (gel) so it requires long processing steps: sol formation, gelling, drying curing and sintering. Precursors used in the preparation are usually inorganic metal salts or metal organic compounds. Typically, formation of a colloidal suspension involves a series of hydrolysis reactions. Further processing of the colloidal suspension leads to formation the desired materials (thin films, nanocomposites or nanoparticles). Typical sizes of nanoparticles produced by this method are 5-30 nm. Some advantages of this technique are low processing temperatures, high homogeneity and purity of products [14].

Chemical precipitation is also widely used to synthesize nanometer-sized oxide powders. In this process, salts are dissolved in a liquid medium. The solution is then mixed with a solution of dissolved precipitating agent, such as ammonium hydroxide, in order to precipitate the hydroxides. The final crystalline oxide is then obtained by firing the precipitates at a higher temperature. A significant problem in such a process is the agglomeration of the particles in the solution. This problem can be overcome by adding dispersants in the reaction process to provide repulsive (electrostatic or steric) interactions between the particles to prevent them from adhering to each other. Organic solvents such as ethanol may be added in the final washing step to replace water adsorbed on the powder surface. This method has some advantages such as technical simplicity, low manufacturing cost, high reproducibility and fine particle size whereas the difficulty to control the final chemical composition of the products represents significant disadvantage. Moreover, it is considered a time-consuming method due to the repeated washing and separation steps needed for precipitation [14].

1.2.4. Gas phase synthesis

Gas phase synthesis techniques have received a great attention and developed remarkably within the last few years. These techniques include gas condensation processing (GPC) laser pyrolysis (LP), pulsed laser ablation (PLA) and microwave heat treatment methods.

Gas condensation process (GPC) is considered one of the most widely used methods in the recent years for fabrication of nanomaterials. In this process, precursor- metal or inorganic material is vaporized using thermal evaporation sources such as electron beam heating devices [15] and sputtering sources [16]. With heating the precursor under high vacuum conditions, the atoms leave the source in straight line paths to settle on a low heated solid surface leading to film growth. This technique is suitable for fabrication of metal nanoparticles, since many metals evaporate at rates of attainable temperature. Metal oxide can be produced by including a reactive gas such as O_2 [11]. One of the benefits of this method is that the improved control of particle sizes by adjusting the flow rate of the inert gas [17]. However, it gives a broad particle size distribution [17, 18]. (PLA) is a surface process which can be used to evaporate a plume of material from a solid surface by irradiating the surfaces with laser beam. The vaporized material condenses to form nanoparticles. Even though this method can produce only small amount of nanoparticles, it can vaporize materials that cannot be evaporated by other techniques [11].

LP is also a frequently used method for the synthesis of nanopowders. In such method, heating the precursors is achieved by absorption of adequate laser energy. Compared to heating the gases in a furnace, this method allows highly localized heating and rapid cooling since only a portion of the gas is heated. Heating is generally achieved by using an infrared (CO_2) laser [11].

Finally, microwave heat treatment techniques have lately gained more attention by many researchers due to some of their advantages such as synthesis of high quality nanomaterials in a short time. The general idea for obtaining nanostructured material by using these techniques is to exploit the microwave radiation for heating precursors.

1.3. Microwaves processing of materials

1.3.1. Microwaves

Microwaves are defined as electromagnetic radiation with wavelength ranging from 1m down to 1mm corresponding to frequencies between 0.3 to 300 GHz. Fig. (1.1) shows the microwave region of the electromagnetic spectrum. The home-cooking microwave ovens are designed to operate at 2.45 GHz (12.25 cm wavelength) [19].

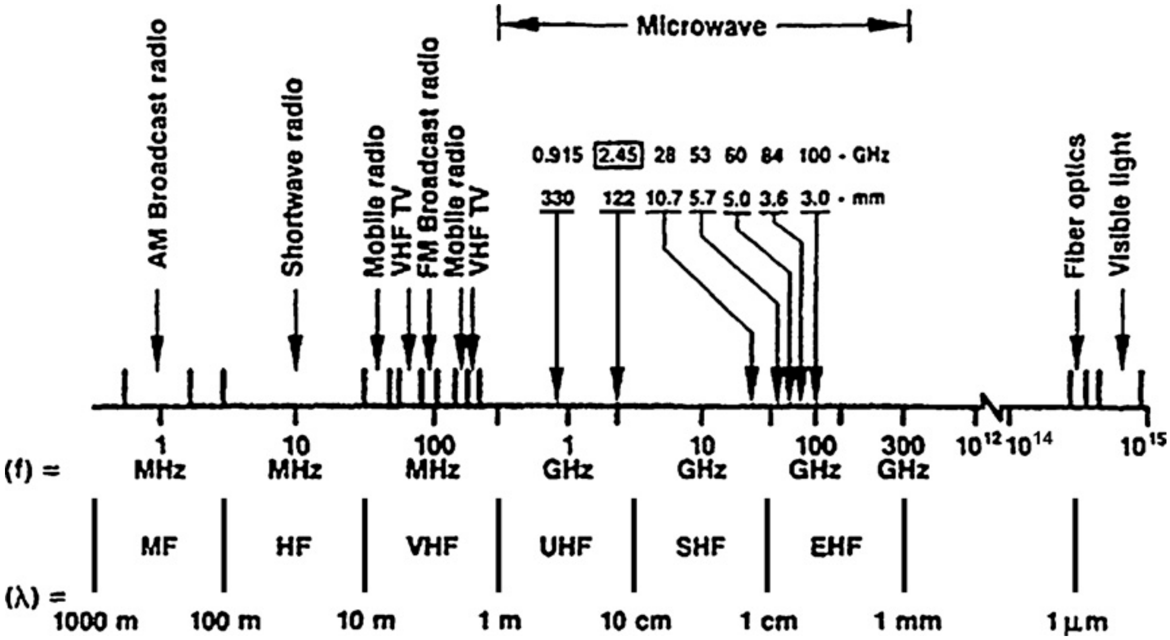

Fig. 1.1. Region of microwave frequencies in the electromagnetic spectrum [20].

Microwave heating process is fundamentally different from conventional heating. In the microwave heating process, the heating is generated internally within the material by interaction of the microwave radiation with the material instead of heat transfer to the material from an outer source as in conventional heating.

There are several advantages for microwave heating compared to conventional heating such as rapid heating, selective heating [20], and improved physical and mechanical properties [21]. In addition, the microwave - synthesized materials exhibit some properties that are better than those of the conventionally - synthesized ones such as better crystallinity (high peak intensities), and catalytic activity [22].

1.3.2. Microwaves-material interactions

Generally, materials can be classified with respect to its interaction with the microwaves into three distinctive groups as shown in Fig. (1.2): transparent materials (insulators) - that have low-dielectric loss factor - microwaves pass through with little losses; reflective materials (conductors) in which microwaves are reflected and do not penetrate; and absorbing materials (high-dielectric loss materials) that absorb the microwaves depending on the value of the dielectric loss factor. There is a fourth type of interaction called mixed absorber. This latest type is observed in composite or multi-phase materials where one of the phases is high-loss material whereas the other is low-loss material and in this case the process is called microwave hybrid heating (MHH) [21].

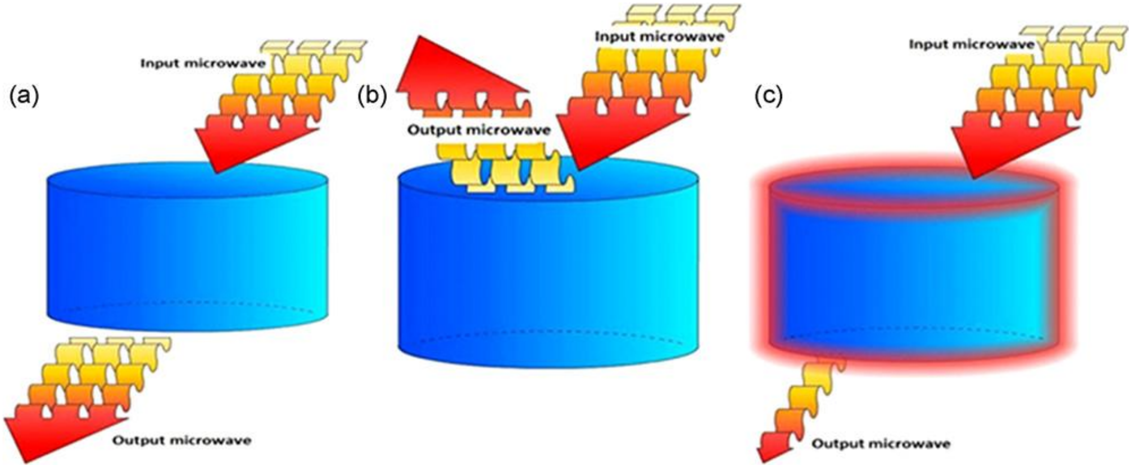

Fig. 1.2. Three types of materials due to the interaction with microwaves: (a) transparent, (b) opaque (conductor) and (c) absorber.

1.4. Nano-structured bismuth oxide (Bi_2O_3)

Nanostructured bismuth oxide (Bi_2O_3) has attracted a great attention due to its importance in modern solid state technology [23]. There exist five main crystalline polymorphs of Bi_2O_3: α-Bi_2O_3 (monoclinic), δ-Bi_2O_3 (face centered cube), γ-Bi_2O_3 (body-centered cube) β-Bi_2O_3 (tetragonal) and ω-Bi_2O_3 (triclinic). The α-Bi_2O_3 phase transforms into the δ-Bi_2O_3 phase at 729 °C [23-24], which remains the structure until the melting point, at 824 °C. When cooled, the δ-Bi_2O_3 phase transforms into the β-Bi_2O_3 phase at 650°C or to the γ-Bi_2O_3 phase at 639 °C. The high-temperature δ-Bi_2O_3 phase and low-temperature α-Bi_2O_3 phase are stable but the other phases are metastable at high temperature [23, 25]. For the ω-Bi_2O_3 phase, it can be obtained at 800 °C on a BeO substrate and only its XRD pattern has been reported so far [24].

Bi_2O_3 exhibits remarkable properties, such as wide band gap, high dielectric permittivity, high refractive index, photoconductivity, high oxygen-ion conductivity and photoluminescence [26-31]. These special properties recommend it for a wide range of applications, such as gas sensor [32], solar cells [33], ceramic glass manufacturing [34], and catalysis [35]. In particular, the wide band gap and high chemical stability of Bi_2O_3 enable it to serve as a water-splitting photocatalyst [36], microwave integrated circuits [37] and optoelectronics [38]. Furthermore, unlike most of the heavy metal oxide, Bi_2O_3 has low toxicity [39]. Hence, it is safer to be used in medical applications compared to other heavy elements such as lead and its oxide and other toxic metals [40]. Nanostructured Bi_2O_3 can be incorporated with polymers for bone implants, surgical instruments and in plastics for easy X-ray detection without deteriorating the physical properties of the matrix material because of Bi_2O_3 submicron size [41-42].

Several techniques were reported to synthesize Bi_2O_3 such as chemical method [43], microemulsion method [44], oxidative metal vapor phase deposition method [23, 45], metal- organic chemical vapor deposition (MOCDV) [46] and microwave irradiation (MW) [47]. Substantial efforts have been devoted by researchers to develop simple nanoparticle synthesis techniques that enable them to control the size and size distribution of the nanoparticles.

In this work, we modified a domestic microwave oven and specially designed SiC composite microwave heater (susceptor) to be utilized for synthesizing Bi_2O_3 nano-powder. The basic idea of this method can be summarized as follows: elemental bismuth is placed into a cavity situated within a microwave susceptor made from silicon carbide (SiC) composite material. The susceptor is thermally shielded with fibrous alumina. Alumina is very high refractory and microwave transparent material. Upon subjecting the susceptor to the microwave radiation, the susceptor will absorb the radiation and convert the radiation energy to heat. Accordingly, the absorbed energy will be transmitted to the metal inside the susceptor and melting it as the susceptor temperature reaches or exceeds the metal melting temperature. At elevated temperature the metal will evaporate. A horizontal channel was used to inject gas carrier to the susceptor cavity, where it is mixed with evaporated metal and exits the cavity through a vertical channel to oxygen rich environment. As a result, it will be oxidized and the metal oxide nanoparticles produced will be collected by a filter. Fig. (1.3) shows the setup used in this work, which is based on the technique patented by Dr. S. A. Al-Quraishi [48].

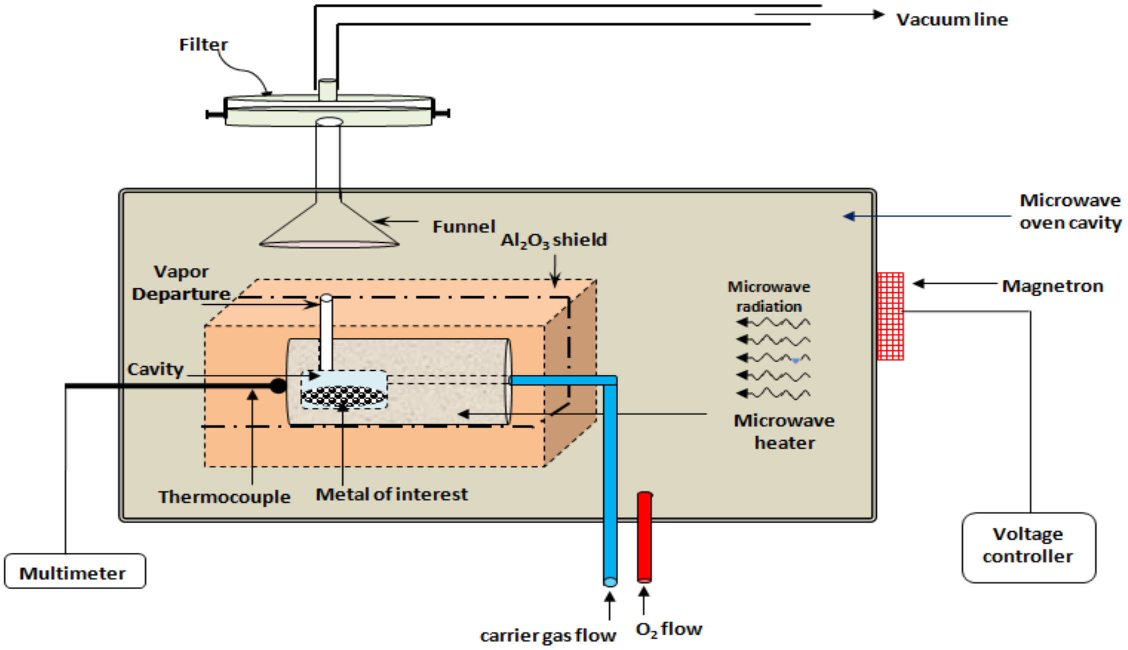

Fig. 1.3. A schematic diagram of the modified microwave set up.

The main advantages of this method are:

1. Fast method for fabricating of nano-metal oxide.
2. High production yield.
3. Simple heating
4. Clean method.
5. Low cost method.
6. Availability of several controlling parameters such as gas flow rate, synthesis temperature and type of the carrier gas that can be used to control the oxidation of the synthesized material and alter its size.

1.5. Objectives

The main objectives of this work are:

1. To modify a domestic MW oven and fabricate specially designed SiC composite MW heater (susceptor) that can be used in the synthesis of metal oxide nanoparticles.
2. To synthesize Bi_2O_3 nano-powder.
3. To characterize Bi_2O_3 nanopowder using different analytical techniques such as x-ray diffraction (XRD), x-ray photoelectron spectroscopy (XPS) and field emission scanning electron microscopy (FESEM).
4. To study the effect of different parameters such as gas flow rate, synthesis temperature and type of the carrier gas on the size of the production yield.
5. To study the optical properties (band gap) of the as-synthesized Bi_2O_3 nano-powder.

1.6. Importance of the study

This study is important for two reasons:

a) In applications, Bi_2O_3 nanostructure powder can be used :

1. As a membrane in solid oxide full cell since it has high oxygen-ion conductivity.

   2. For water treatment as a photocatalyst.

b) As a substitute of lead in many medical applications since it has lower toxicity.

CHAPTER 2

LITERATURE REVIEW

Owing to the peculiar characteristics and wide applications, Bi_2O_3 has gained special interest of numerous workers. This special interest explains the substantial efforts devoted to synthesis and characterization of Bi_2O_3 nanoparticles over the past decades. This chapter will survey various techniques used to synthesize and this material.

It has been reported by Mädler and Pratsinis that nanostructured Bi_2O_3 particle were prepared via the flame spray pyrolysis (FSP) of bismuth nitrate. They have found that the type of solvent affects strongly the morphology and homogeneity of the synthesized material. Using ethanol and nitric acid as solvents, they prepared hollow and sintered dense spheres whereas they synthesized solid nanoparticles when they used acetic acid as solvent. The average crystallite size of the product was in the range of 50-100 nm [49].

W. Li has synthesized spherical monodisperse Bi_2O_3 nanoparticles from $Bi(NO_3)_3$ homogenous solution in the presence of polyethylene glycol (PEG) using a precipitation method [50]. In his work, Bi_2O_3 nanomaterials large product, uniform shape and narrow distributions were obtained under optimized parameters such as concentration of $Bi(NO_3)_3$ and reaction temperature. By varying the experimental parameters, he also found that the average crystallite size of the yield was decreased from 67 to 60 nm.

Microemulsion method is another technique that can be used to synthesize nanoparticles. This technique has been exploited by Dong et al. to synthesize stearic acid coated Bi_2O_3 nanoparticles in the range of 5-13 nm. The synthesized product showed strong photoluminescence (PL) at 397 and 420 nm and the absorption edge of Bi_2O_3 nanoparticles showed a blue shift of ~0.45 eV compared to that of bulk Bi_2O_3 [44].

Citrate gel method was used for synthesizing Bi_2O_3 nanoparticles with an average size range between 50-80 nm by M. Anilkumar et al. [51]. In their process, mixing bismuth nitrate solution with citric acid resulted in forming a yellowish gel after heating on water bath at 373 K. Then, the gel was decomposed at 400 °C producing nanocrystalline Bi_2O_3 nanoparticles.

López-Salinas et al. synthesized nanostructured powders of Bi_2O_3, BiOCl and Bi by a simple aqueous precipitation method using elemental bismuth as a precursor and varying some experimental conditions. The particle size of Bi_2O_3 nanopowders as was found by transmission electronic microscopy (TEM) was about 50 nm and the band gap of as-synthesized material was found to be 2.3 eV [52].

Using atmospheric pressure chemical vapor deposition approach (APCVD), Shen et al. synthesized Bi_2O_3 nanowires on Au-coated Si substrates [53]. The synthesis process was carried out in a quartz tube situated inside a horizontal tube furnace using Bi $(S_2CNEt_2)_3$ as a precursor in the presence of oxygen. The synthesized Bi_2O_3 nanowires with β-Bi_2O_3 phase had diameters ranging from 50 to 100 nm, and a length of the order of tens of microns.

Geng Lin et al. reported the fabrication and photocatalytic property of α-Bi_2O_3nanoparticles by femtosecond laser ablation in ethanol at room temperature [54]. The as-synthesized material had a mean particle size of ~10 to 60 nm, almost spherical or irregular spherical shape, and a band gap of about 3.38 eV.

A ball milling process was used for preparing nanocrystalline Bi_2O_3 by Chakrabarti et al. [55]. A ball mill grinder was used for milling pure Bi_2O_3 powder to produce different particle sizes (from 194 to 36 nm).

Using microwave irradiation (MWI), Anandan et al. [47] reported a rapid and controllable synthesis of Bi_2O_3 short nanorods in aqueous solution. The crystalline structure of as-prepared nanoparticles was α-Bi_2O_3 phase, and the band gap was found to be 2.83 eV. Compared with the absorbance spectrum recorded for commercial Bi_2O_3

powders, at about 470 nm, the Bi_2O_3 nanorods exhibited a blue shift. The blue shift was, of course, due to the quantum-size effect in semiconductors as the particle size decreases. TEM analysis showed that the formation of short nanorods (~ 100 nm in diameter and several micrometers in length).

Solution-based methods were used by Cheng et al. [56] to synthesize three different phases of Bi_2O_3 (α-Bi_2O_3, β-Bi_2O_3, and δ-Bi_2O_3). Using UV-Vis diffuse reflectance spectroscopy, the band gaps were estimated to be 2.80, 2.48, and 3.01 eV for α-Bi_2O_3, β-Bi_2O_3, and δ-Bi_2O_3, respectively. PL of the three Bi_2O_3 phases was studied with the excitation wavelength at 300 nm. It was observed that both α-Bi_2O_3, δ-Bi_2O_3 showed a strong broad emission peak around 460 nm, however, β-Bi_2O_3 showed a rather lower intensity.

A facile hydrothermal approach was used for preparing β-Bi_2O_3 nanowires using commercial Bi_2O_3 and K_2SO_4 as reactants [57]. TEM results revealed that the as-prepared material diameter ranged from 30 to 100 nm and the length was up to tens of micrometres.

Kim et al. investigated the effect of the growth temperature on the β-Bi_2O_3 nanostructures synthesized by metal organic chemical vapor deposition (MOCVD). They found that the product morphology was affected by varying the substrate temperature. One-dimensional structures at a lower temperature of 400°C with a diameter of 30 – 90 nm and lengths that reached up to several micrometers were prepared; however, they obtained cluster – or film-like structures at 500°C. The PL spectrum of the sample with nanowires showed a blue emission centered at around 2.8 – 3.1 eV [58].

A simple sonochemical route was used for synthesizing nanocystallite α-Bi_2O_3. The as-synthesized material had a grain size of 40-100 nm in the presence of 0.5 g surfactant polyvinylpyrrolidone. The band gap of the prepared material was 2.85 eV. The authors also studied the photocatalytic performance of the nanocrystallyte α-Bi_2O_3 using methyl orange (MeO) as a pollutant. They found that the product can degrade 86% MeO within 100 min under visible light illumination ($\lambda > 400$ nm) [59].

Wang et al. synthesized oblique prism-like Bi_2O_3 via a simple one-step aqueous method at low temperature and ambient pressure in the presence of sodium dodecylbenzenesulfonate (SDBS) [60]. The as-prepared samples were phase-pure with a diameter of 2 µm. The direct band gap energy of the oblique prism-like Bi_2O_3 was estimated and found to be 2.83 eV. The PL spectrum of oblique prism-like Bi_2O_3 obtained at room temperature with excitation wavelength of 286 nm (4.33 eV) showed three emission bands: a strong green emission band centered at 537 nm (2.31 eV), a blue-green band at 484 nm (2.56 eV), and a blue band at 443 nm (2.80 eV).

Structural evolution of Bi_2O_3 prepared by thermal oxidation of bismuth-nanoparticles was reported [13]. At first, bismuth nanoparticles were produced via chemical reduction method. Then, the as-produced bismuth nanoparticles were thermally oxidized in air at different temperatures in the range 100-750°C to obtain nanostructured Bi_2O_3. The interesting conclusion was that the phase transition and morphology of the obtained nano-structured Bi_2O_3 were affected by the annealing temperature.

CHAPTER 3

CHARACTERIZATION TECHNIQUES

Different analytical techniques namely; X-ray diffraction (XRD), X-ray photoelectron spectroscopy (XPS), field emission scanning electron microscopy (FESEM), and spectroscopy techniques were used to characterize the nano-structured materials produced by microwave-assisted combustion method. This chapter illustrates the central ideas behind each of these techniques and their limitation.

3.1. X-ray diffraction (XRD)

XRD is an important experimental technique used for investigating all issues related to the crystalline structure of solids such as, determination of crystallinity, crystalline size (grain size), and orientation of single crystals. It is also commonly used for the identification of unknown materials and determination of the lattice constants of the crystal. The basic principle of XRD depends on the diffraction of x-ray waves by atoms of material being analyzed to give deep information about the structure of this material.

X-ray waves can be scattered by atoms, as shown in Fig. 3.1, off the atom's electrons. If the scattered x-ray waves are in phase (coherent), they interfere in a constructive way resulting diffracted beams in specific directions determined by Bragg's law:

$$2d\sin\theta = n\lambda$$

Where d is the spacing between diffracting planes (atomic planes), θ is Bragg's angle, n is the order of diffracted beam and λ is the wavelength of the x-ray beam. X-rays are used to produce diffracted patterns since their wavelength λ is selected to be the same order of magnitude as the atomic spacing size (~ 1 angstrom). Therefore, Bragg's law plays an important role in indexing x-ray diffraction patterns and for determining the crystal structure of materials.

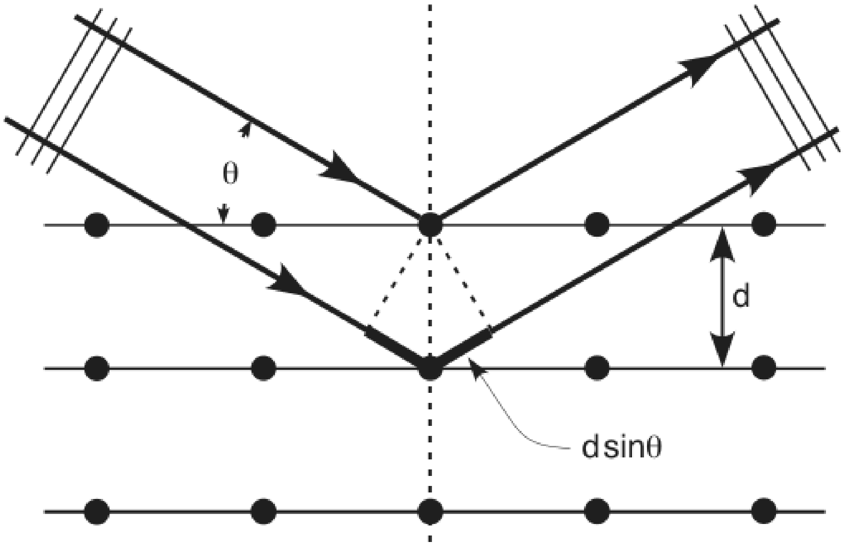

Fig. 3.1. A schematic of diffraction of x-rays by a crystal.

The three basic components of XRD diffractometer are: x-ray source, specimen and x-ray detector. In a typical XRD diffractometer, x-rays are generated by heating a tungsten filament cathode (with a current) to emit electrons that are accelerated toward the anode (target) by applying a high voltage. As the emitted electrons strike and eject an inner shell electron of the atom of the target, x-rays are produced. The beam of produced x-rays, in turn, is applied on the sample being analyzed to be diffracted and appears as spots on the diffraction patterns according to Bragg's law. The diffraction pattern is like a fingerprint of the substance and consists of a series of peaks that corresponds to the x-ray diffracted from a specific set of planes in the material being analyzed. On modern devices, peak searches are performed on a computer. The computer plots the peak intensity versus the diffraction angle 2θ, and therefore, one can compare standard patterns from the JCPDS data base with experimentally observed patterns, allowing rapid matching of patterns and material identification [61].

The crystallite size and the lattice strain can be determined by the width of the individual peaks, usually defined as the full width at half maximum (FWHM). X-ray diffraction peaks in XRD patterns can sharply arise if there are no effective factors to broaden them. But actually the broadening of these peaks is caused due to three reasons: instrumental effects, crystallite size and strain effects within the crystal lattice.

Thus, the broadening B_c due to the crystallite size and lattice strain, of the diffraction peaks exhibiting Gaussian profile, is presented as [62]

$$B_c = (B_o^2 - B_i^2)^{1/2}$$

where B_o is the observed peak broadening and B_i is the instrumental broadening.

According to Scherrer's equation [62], the crystallite size (t) can be calculated from XRD peak broadening by:

$$t = K\lambda / (B_c \cos\theta)$$

where λ is the incident x-ray wavelength, B_c is the broadening (in radians) due to the crystallite size, θ is Bragg's angle and K is a constant depends on particle geometry (usually taken to be ≈1).

XRD used in this work is a Shimadzu XRD-6000 X-ray diffractometer with the following operation conditions:

- X-ray wavelength (λ = 1.5406 Å) corresponds to $Cu\ k_{\alpha}$.
- The current and voltage used were 30 mA and 40 kV respectively.
- Scanning speed for data collection was 2 degree/min.
- The substrate used was aluminum.
- The angle scanned (2θ) was 20-80 degree.

3.2. X-ray photoelectron spectroscopy (XPS)

XPS is considered one of the most powerful analytical techniques that provide the following: identification of all elements, except H and He, present at concentrations greater than 0.1 atomic %, elemental surface composition, and information about the molecular environment such as oxidation state and covalently bonded atoms. The main components of XPS, as shown in Fig. 3.2, are x-ray gun, transfer lenses, hemispherical electron energy analyzer (HSA) which disperses the emitted photoelectrons due to their speeds and a detector for recording their intensity.

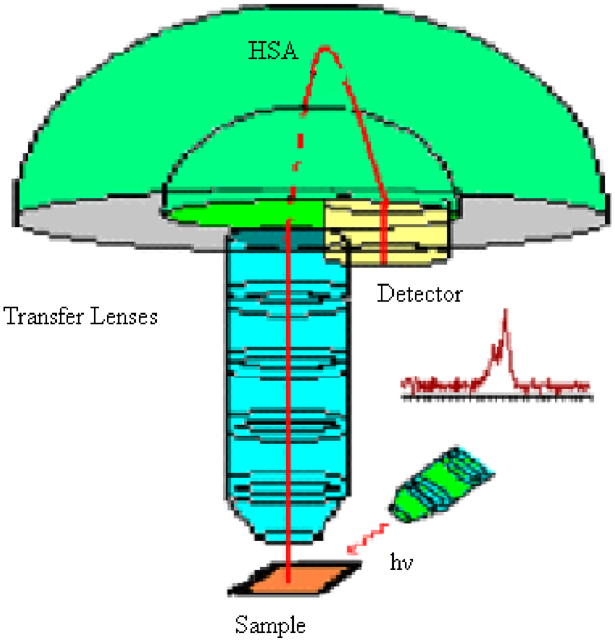

Fig. 3.2. A schematic of an XPS instrument.

In XPS, an incident beam of monochromatic x-rays irradiates the sample of study resulting in photoelectron emission from the core level of atoms on the specimen's surface with certain kinetic. The kinetic energy of the emitted photoelectron is linearly proportional to the frequency of the incident x-rays. The binding energy of each core-level electron is a characteristic of the atom and the specific orbital to which it belongs. The work principal of XPS can be expressed by the Einstein equation [63]:

$$E_B = h\nu - E_k - \Phi$$

where $h\nu$ is the energy of the incident x-ray, E_k is the kinetic energy of the emitted photoelectron and Φ is the work function, energy needed to move an electron from the

Fermi level of the solid into vacuum. The binding energies of the various elements have been measured and well tabulated in reference tables. These tables are used as a reference when studying the surface atomic composition of any sample [64]. XPS analysis was achieved using a VG Scientific MKII spectrometer with a monochromatic Aluminum $K\alpha$ (1486.6 eV) X-ray source.

3.3. Field emission scanning electron microscopy (FESEM)

FESEM can be classified as a high vacuum instrument (less than $1\text{x}10^{-7}$ Pa) that is used for visualizing small structures on the surface of a material and provides the chemical composition characterization near the surface of the sample of interest. Compared to scanning electron microscopy (SEM), the electrons emission source in the FESEM is a field emitter instead of thermionic emitter. In the thermionic emitter of SEM, a filament is heated by applying an electrical current. As the thermal energy is enough to overcome the work function of the filament material, the electrons leave the material. The main disadvantages of SEM are evaporation of cathode material and relative low resolution. Such disadvantages are overcome in the field emitter in which the electron emission is achieved by placing the filament in a huge electrical potential gradient. This modification leads to higher electron density and better resolution than with SEM device.

The basic components of the FESEM device are shown in Fig. 3.3. An electron emission source, condenser lens, scan coils, objective lens, an appropriate detector (scintillator) and photomultiplier tube. The electron emission source is a very thin and sharp tungsten tip of 20-200 nm, works as a cathode. Tow anodes are employed. Applying a potential of 3 kV to the first anode, the electrons are released. Then, they pass through a hole in it and are accelerated to their final energy by applying a high potential to the second anode. The condenser lens controls the diameter of the electron beam where a narrow beam results in better resolution. The electron beam is then deflected and focused over the sample of interest by scan coils and objective lenses, respectively. When the electron beam strikes the surface of the sample, secondary electrons are emitted. The emitted secondary electrons produce photons as they reach the scintillator. These photons are guided by a light pipe to a photomultiplier forming the basis of the video signals recorded on cathode ray tube or computer frame store that shows the FESEM image [65]. FESEM analysis was performed using a Tesccan model Lyra-3, FESEM.

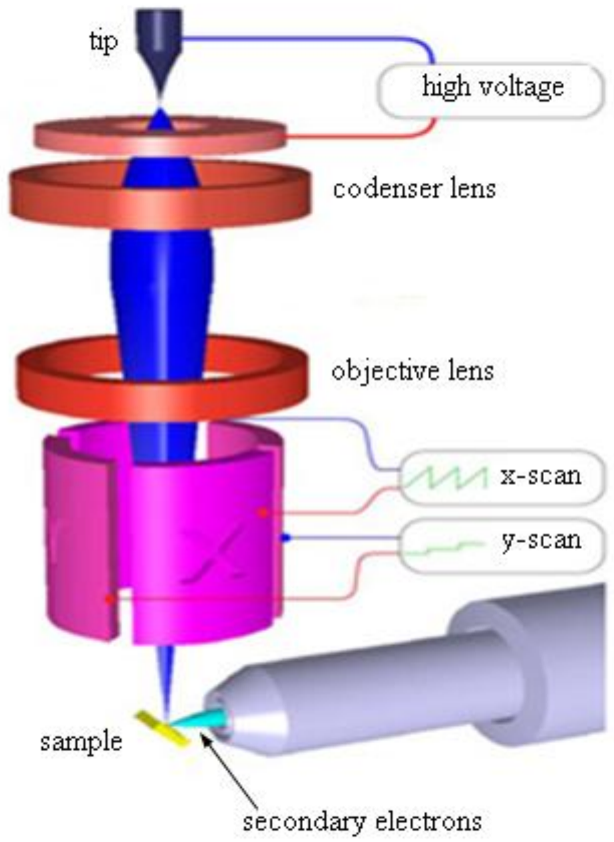

Fig. 3.3. A schematic diagram of field emission scanning electron microscopy.

3.4. UV-visible diffuse reflectance spectroscopy

One of the most common spectrophotometers is UV-visible spectrophotometer (UV-vis absorption spectrophotometer) that is used to measure transmission or absorbance of light in the UV-visible spectrum regions by semiconductors thin films as a function of a wavelength. Since the light scattered from the solid films is low, such technique can be used for extracting the band gap values of these films. However, in powder or colloidal samples the light scattering increases and the dispersed light is counted as absorbed light and the technique becomes unable to distinguish between the scattered and absorbed light. Thus, another technique called UV-visible diffuse reflectance spectroscopy is recommended to obtain the band gap of powder samples [66].The central idea of such a spectrophotometer is measuring the diffuse reflected light from the surface of the powder grains. Since the diffuse reflected spectrum results from numerous interactions between light and sample, it displays the features of the transmission or absorption spectrum.

A UV-visible diffuse reflectance spectrophotometer system consists of a light source, a tungsten/halogen lamp for the visible spectrum or a deuterium lamp for the UV spectrum, diffraction grating monochromator that splits and diffracts light into several beams of different wavelengths, target (sample) holder, and sensor. The general schematic diagram showing the linking up of the UV-visible diffuse reflectance spectrophotometer components is represented by Fig. 3.4. The spectrophotometer used in this work was (Evolution 600).

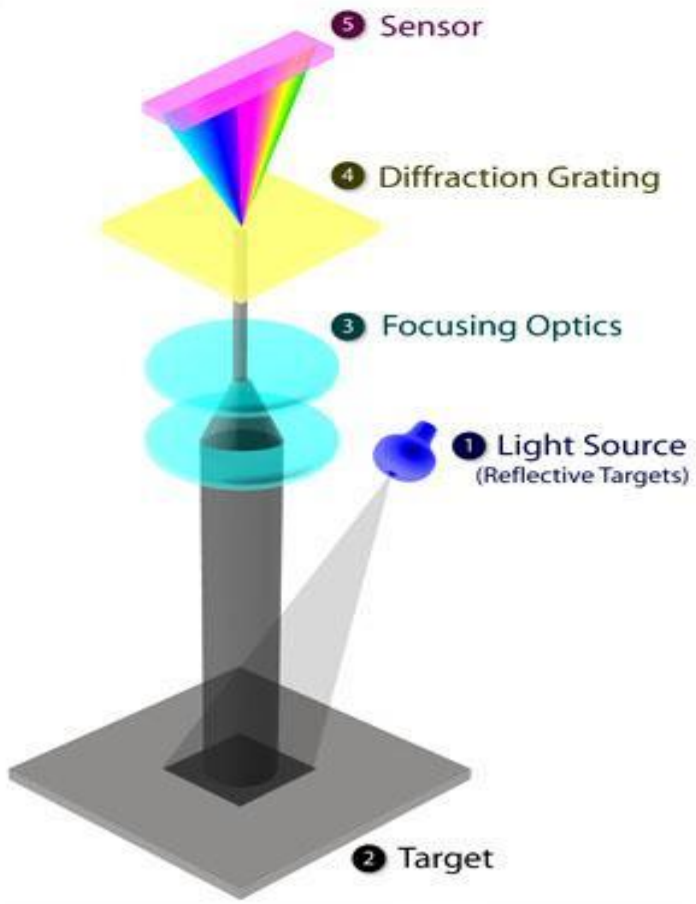

Fig. 3.4. A schematic diagram of double beam spectrophotometer.

CHAPTER 4

EXPERIMENTAL WORK

The experimental work in this thesis is presented by describing the development of microwave setup used to synthesize Bi_2O_3 nano-powder. Then, detailed explanation for the synthesis procedures of the product will be followed.

4.1. Development of microwave set up

The setup used in this study was a home-made system, Fig. 4.1, which consists of : a domestic microwave system model (MS-3443AZ, LG, 2.45GHz frequency, 1600 W), microwave susceptor (especially designed apparatus for the purpose of heating), platinum thermocouple, voltage controller, inlet and outlet tubes, funnel and filter.

In the current study, the microwave was subjected to a series of modifications that can be summarized in the following:

a) 3 mm diameter hole was drilled in the bottom of the microwave cavity for the passage of two Teflon tubes used for injecting gases inside the oven cavity.

b) The microwave susceptor, with horizontal inlet alumina tube and vertical outlet one inserted into it as shown in Fig. 4.2, was situated at the center of the microwave cavity and surrounded by thermal shield.

c) 6 mm diameter hole was drilled on the side wall of the microwave cavity for the passage of the thermocouple.

d) 7 mm diameter hole was also drilled in the top wall of microwave cavity for connecting the funnel hanged on the outlet channel with outside filter.

e) The microwave power and hence, the temperature of microwave susceptor were manually controlled by adjusting the input voltage of the magnetron power supply by a voltage controller (external dimmer stat circuit shown in Fig. 4.3).

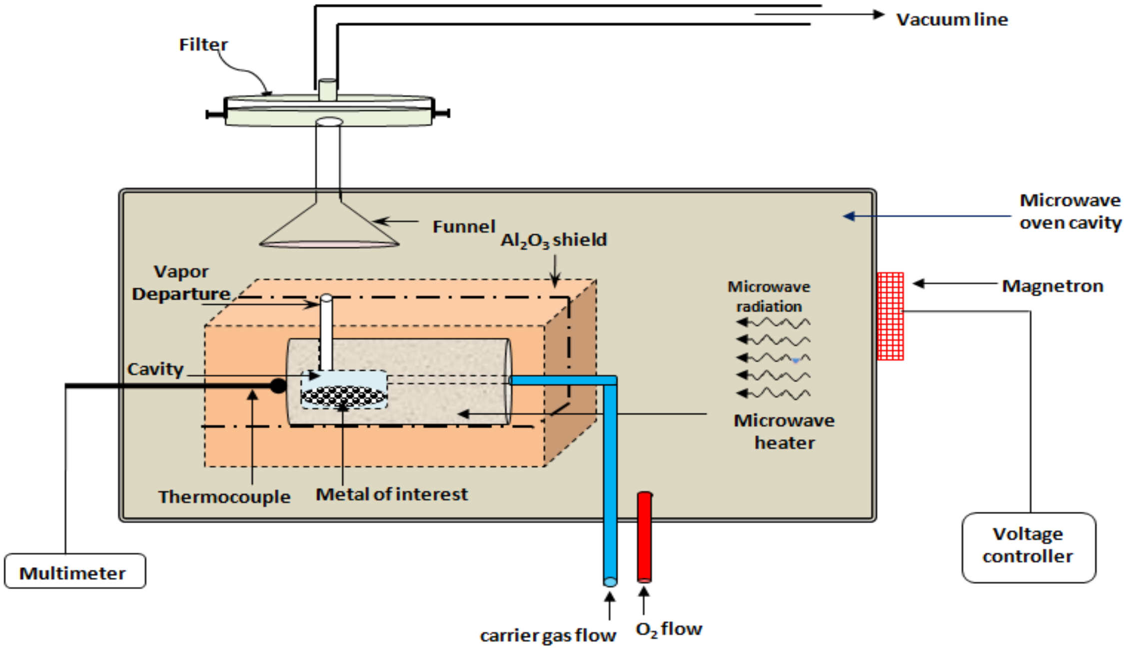

Fig. 4.1.a. A schematic of the developed microwave setup.

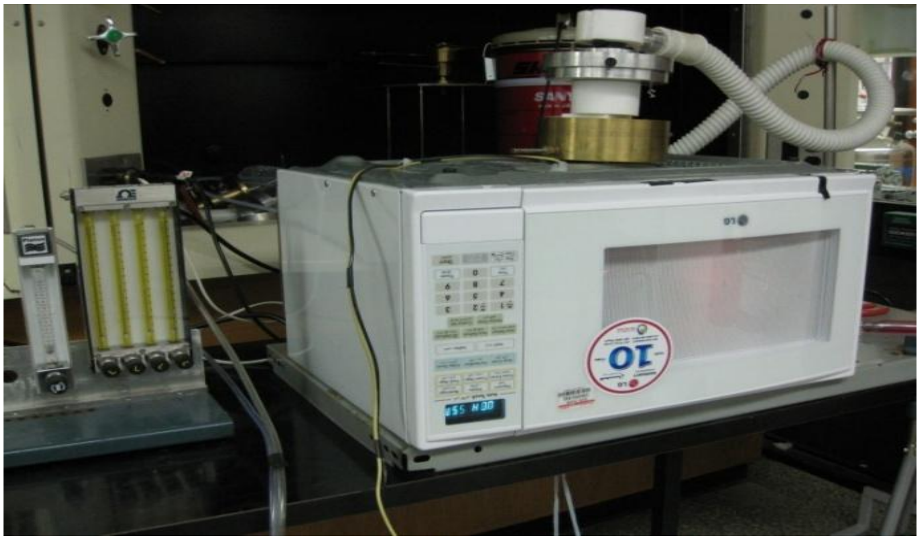

Fig. 4.1.b. Photo of the developed microwave setup.

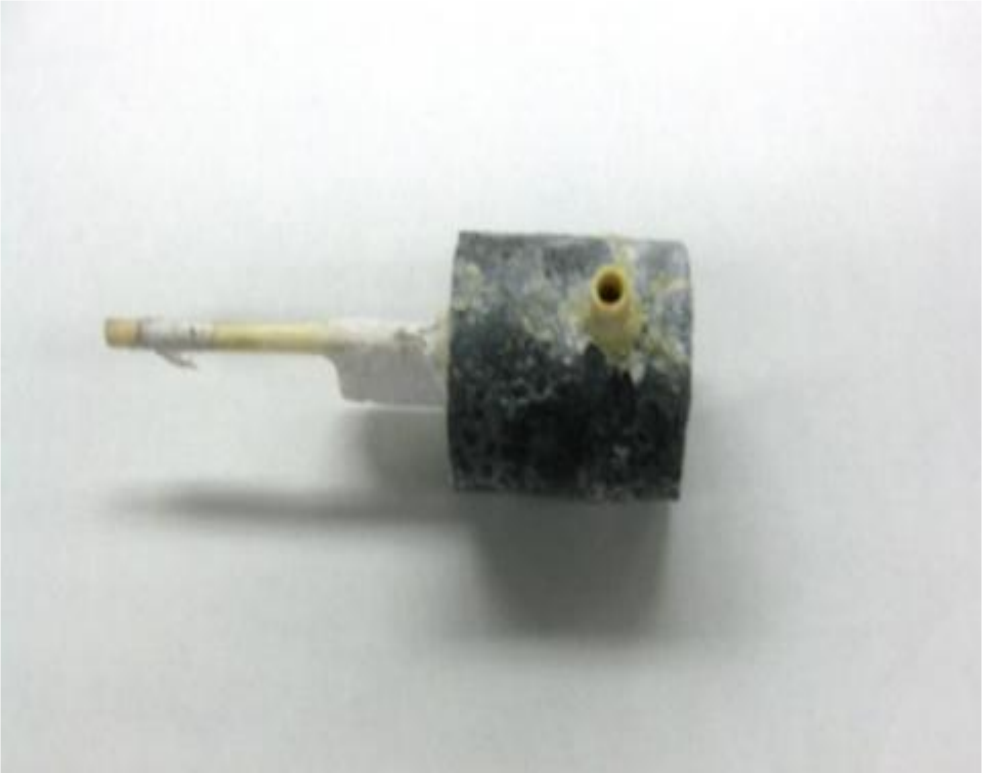

Fig. 4.2. Photo of the microwave susceptor.

Fig. 4.3. Photo of the external dimmer stat circuit.

The temperature of the microwave susceptor was monitored by a platinum- rhodium thermocouple that can measure temperatures up to 1500 °C. This thermocouple contains two different conductors; one is pure platinum conductor, and the second one that contains 13% rhodium. The thermocouple was covered by stain steel tube to be shielded from the microwave radiation and connected to a digital multimeter, as shown in Fig. (4.4.)

The multimeter receives thermal signal from the thermocouple and reads it as a voltage so it was calibrated by temperature scale device for knowing the temperature.

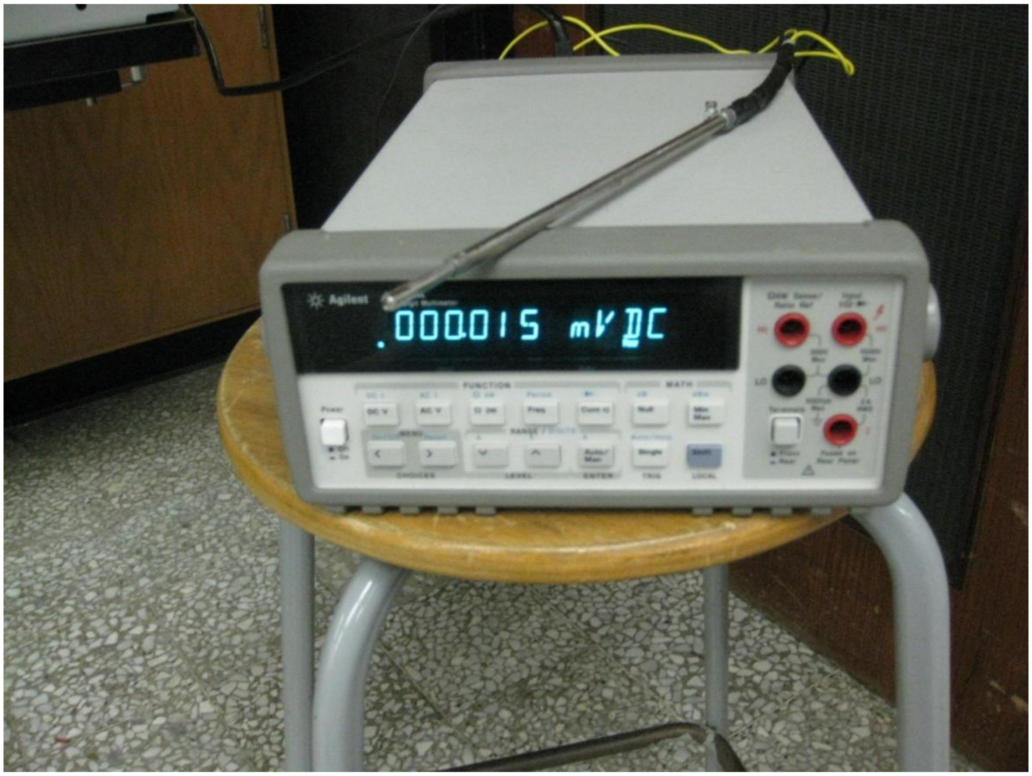

Fig. 4.4. Photo of the platinum- rhodium thermocouple connected to the digital multimeter.

The microwave susceptor was made of silicon carbide (SiC) composite material in the form of a cylinder of 5 cm length and 4.5 cm diameter. The susceptor has a small inner cavity that houses the molten metal and connected to the outside by two ceramic tubes; the horizontal tube is used to insert carrier gas to the cavity, and the other is vertically oriented tube is used as an exit to the evaporated metal. SiC is a relatively highly microwave absorbing material, and is known to be thermally and chemically stable at elevated temperatures. It has a high loss factor of 1.7 at 2.45 GHz at room temperature and about 28 at 700 °C at the same frequency. Thus it has a high efficiency to convert microwave energy to heat. The microwave susceptor was thermally shielded by fibrous alumina (Fig. 4.5), which is a very well known refractory material that is transparent to microwave radiation. A hole was drilled in one of the shield side to allow the thermocouple probe to reach the susceptor, wherein a small hole drilled to insure good contact between the thermocouple and the susceptor.

Fig. 4.5. Photo of the thermal shield made of fibrous alumina.

4.2. Synthesis procedures

In a typical experiment, small chips of high purity bismuth metal (Alpha 99.999%) were inserted into the susceptor cavity through the vertical alumina tube, and oxygen gas was injected inside the microwave cavity through one of the two teflon tubes to enhance metal vapor oxidation. Then, the microwave power was turned on for approximately 30 min in each experiment. The temperature of the susceptor was controlled by adjusting the input voltage of the magnetron power supply using dimmer stat. The susceptor temperature became white hot, when it reaches 900 °C. As the desired microwave susceptor temperature reached, the carrier gas such as nitrogen was injected into the susceptor cavity through the other Teflon tube connected with the horizontal alumina tube. The gases flow rates were controlled by gas flow meters (rotometers) shown in Fig. 4.6. The evaporation rate of the metal inside the susceptor cavity depends on its temperature and on the carrier gas flow rate. Inside the susceptor cavity the carrier gas mixes with the evaporated bismuth. Then, the mixture of evaporated bismuth and the carrier gas exit the susceptor cavity through the vertical alumina tube to oxygen rich atmosphere (the microwave cavity) to be oxidized forming nano-bismuth oxide (Bi_2O_3).

Synthesis experiments were carried out at different temperatures and varied carrier gas flow rates whereas oxygen flow rate was kept at fixed value of 1 L/min. On other hand, approximately one gram of high purity metal bismuth was approximately used in each experiment.

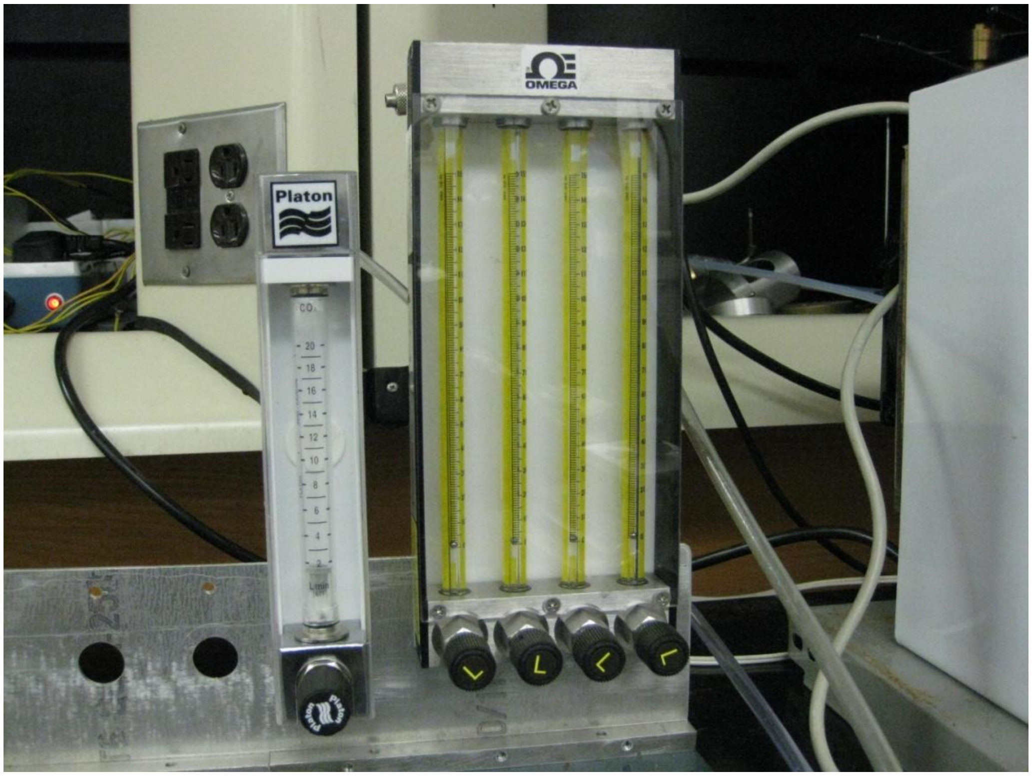

Fig. 4.6. Photo of the rotometers.

CHAPTER 5

RESULTS AND DISCUSSION

In this chapter, results of the synthesized Bi_2O_3 nano-powder will be presented. The effects of different experimental parameters such as synthesis temperature, type of carrier gas (N_2, Ar and He), and flow rates of these carrier gases on the structural, morphological, and optical properties in addition to the chemical composition of the product will be discussed.

5.1. Size controlling parameters

5.1.1. Carrier gas effect

Synthesis of Bi_2O_3 nano-powder was carried out using the carrier gases; namely, N_2, Ar, and He. The primary role of the carrier gas was to transport the evaporated material (pure elemental bismuth) and to dilute the vapor before it is oxidized outside the susceptor. We have found that at fixed flow rate and synthesis temperature, the crystallite size of the production yield was larger in the case of using He as a carrier gas compared to N_2 and Ar. However, it was comparable in the case of the carrier gases; N_2 and Ar. It was observed that when N_2 and Ar were used as carrier gases at some high flow rate, the evaporated bismuth was partially oxidized. On the other hand, the oxidation was higher when He was used as a carrier gas at the same flow rates. This observation was based on the color of the product. Partially oxidized bismuth has greenish yellow color, while completely oxidized bismuth has light yellow color. The reason behind the different oxidation is due to the fact that oxygen has different diffusion rates through different gases. N_2 and Ar gases have almost the same mass as O_2, thus oxygen has a higher possibility to bounce back when it collides with these gases. As a result, the amount of oxygen reaching bismuth vapor is not enough for complete oxidation. On the other hand, He has much smaller mass than O_2. This allows O_2 to easily diffuse through it and oxidize the bismuth vapor.

5.1.2. Synthesis temperature effect

The effect of synthesis temperature on the properties of the synthesized nanoparticles was studied for all carrier gas types at three temperatures namely; 900, 1000, and 1100°C. Temperatures below 900°C were excluded from this study since metal evaporation rate is very low. Temperatures above 1100°C were also excluded to eliminate any contamination possibility (from the susceptor) that arise at very high temperatures.

The phase characteristics and size of the as synthesized bismuth oxide nanoparticles product were determined by XRD measurements. The average crystallite size was obtained using the conventional Scherrer equation [62] while the locations of the peaks in the XRD measurements determine the phases. XRD patterns of the as synthesized Bi_2O_3 nanopowder produced at different synthesis temperatures and different flow rates of N_2, Ar and He are shown in Fig. 5.1.(a-c), Fig. 5.2.(a-c), and Fig. 5.3.(a-c), respectively. According to international Center for Diffraction Data (ICDD) files [67], polycrystalline multi-phases of tetragonal β-and monoclinic α-Bi_2O_3 were obtained, with predominance of β-phase for all carrier gases, for all flow rates and synthesis temperatures. However, the lack of presence of the XRD peaks due to bismuth metal in some samples at high flow rates may indicate that bismuth resides in interstitial positions within the Bi_2O_3 crystal. Thus, it may not be detected through XRD. The average crystallite sizes of the as-synthesized nano-powder were in the range of 19-86 nm, 25-175 nm and 18-133 nm for the cases when N_2, Ar and He, were used as carrier gases, respectively as shown in Table 5.1.

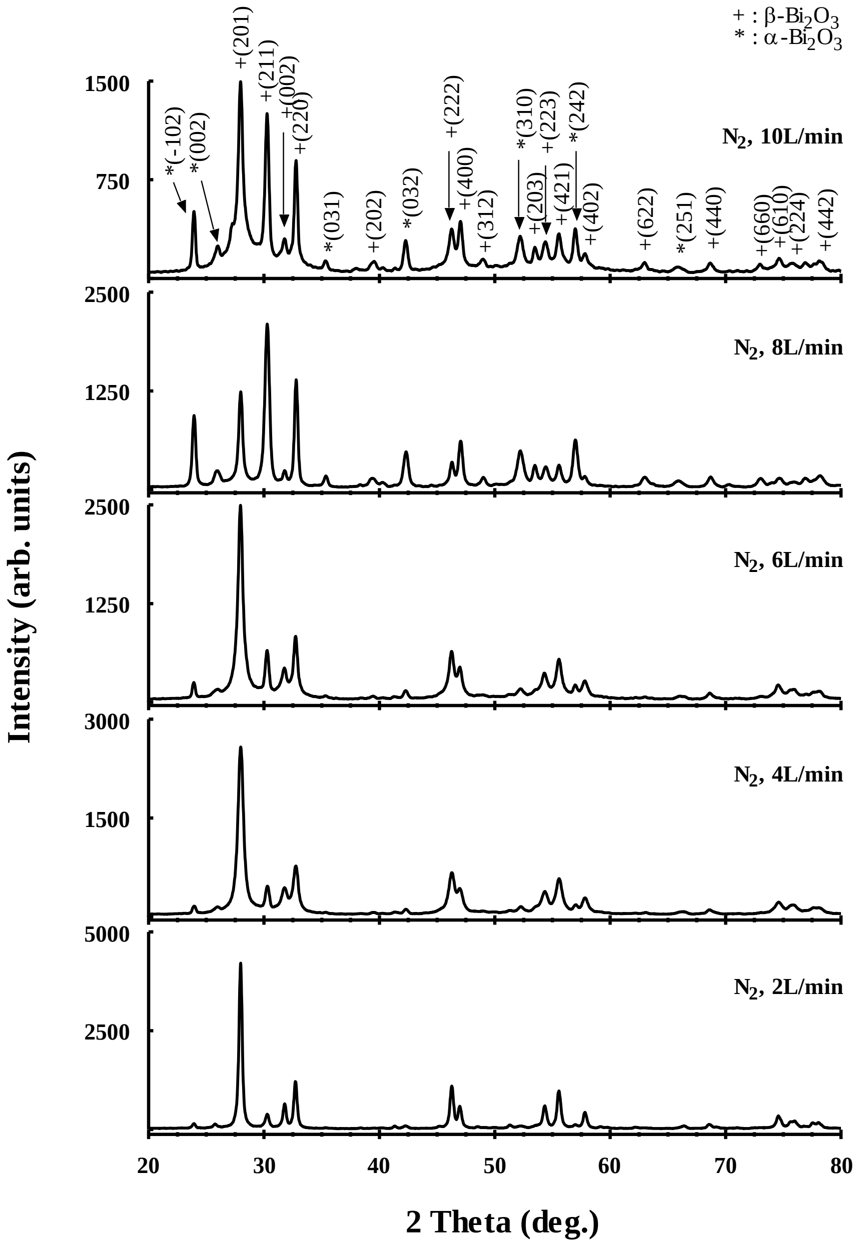

Fig. 5.1.a. XRD patterns of mixed-phases of Bi_2O_3 (β-, and α-Bi_2O_3) powders prepared by MWC at synthesis temperature 900°C and different N_2 flow rates. N_2 flow rate is indicated on each pattern.

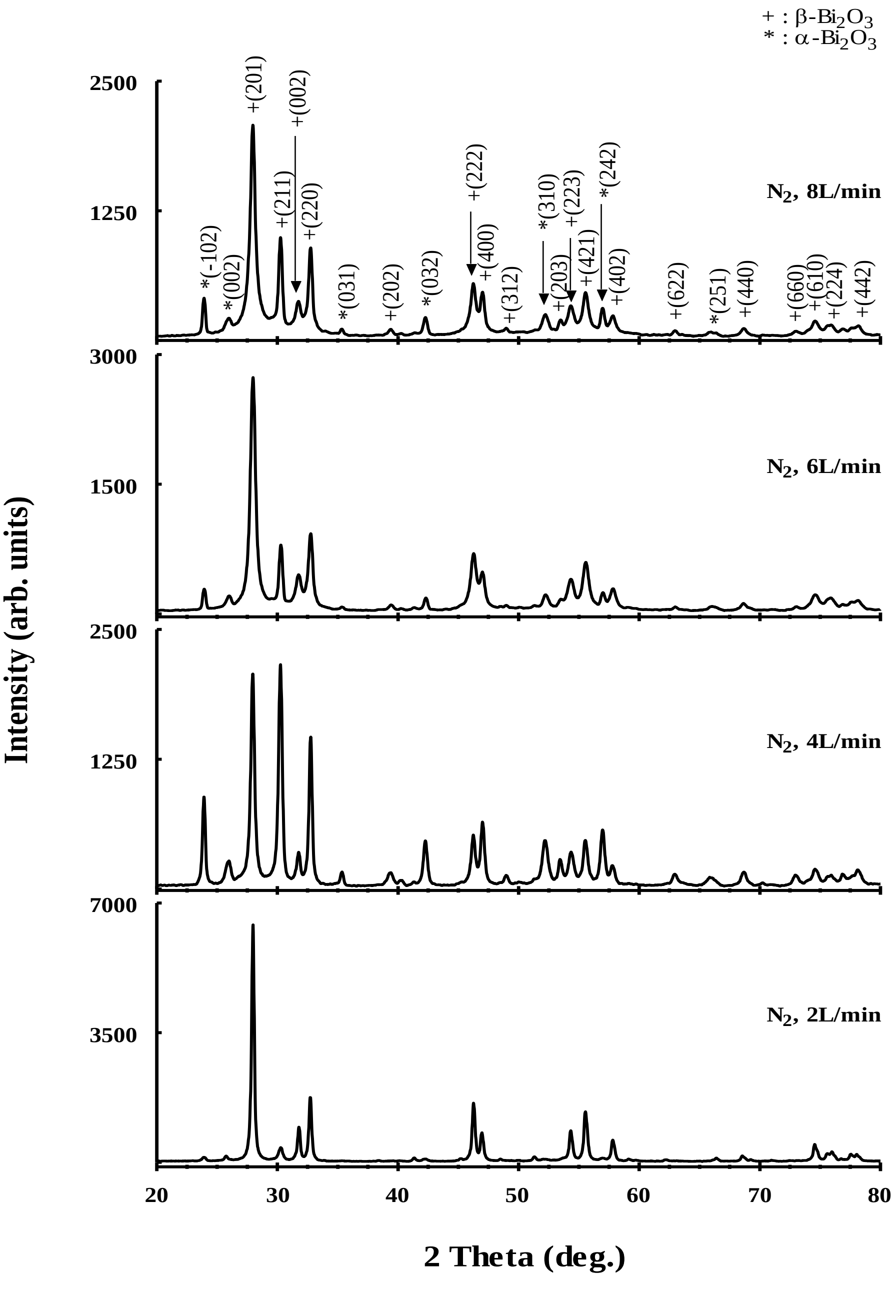

Fig. 5.1.b. XRD patterns of mixed-phases of Bi_2O_3 (β-, and α-Bi_2O_3) powders prepared by MWC at synthesis temperature 1000°C and different N_2 flow rates. N_2 flow rate is indicated on each pattern.

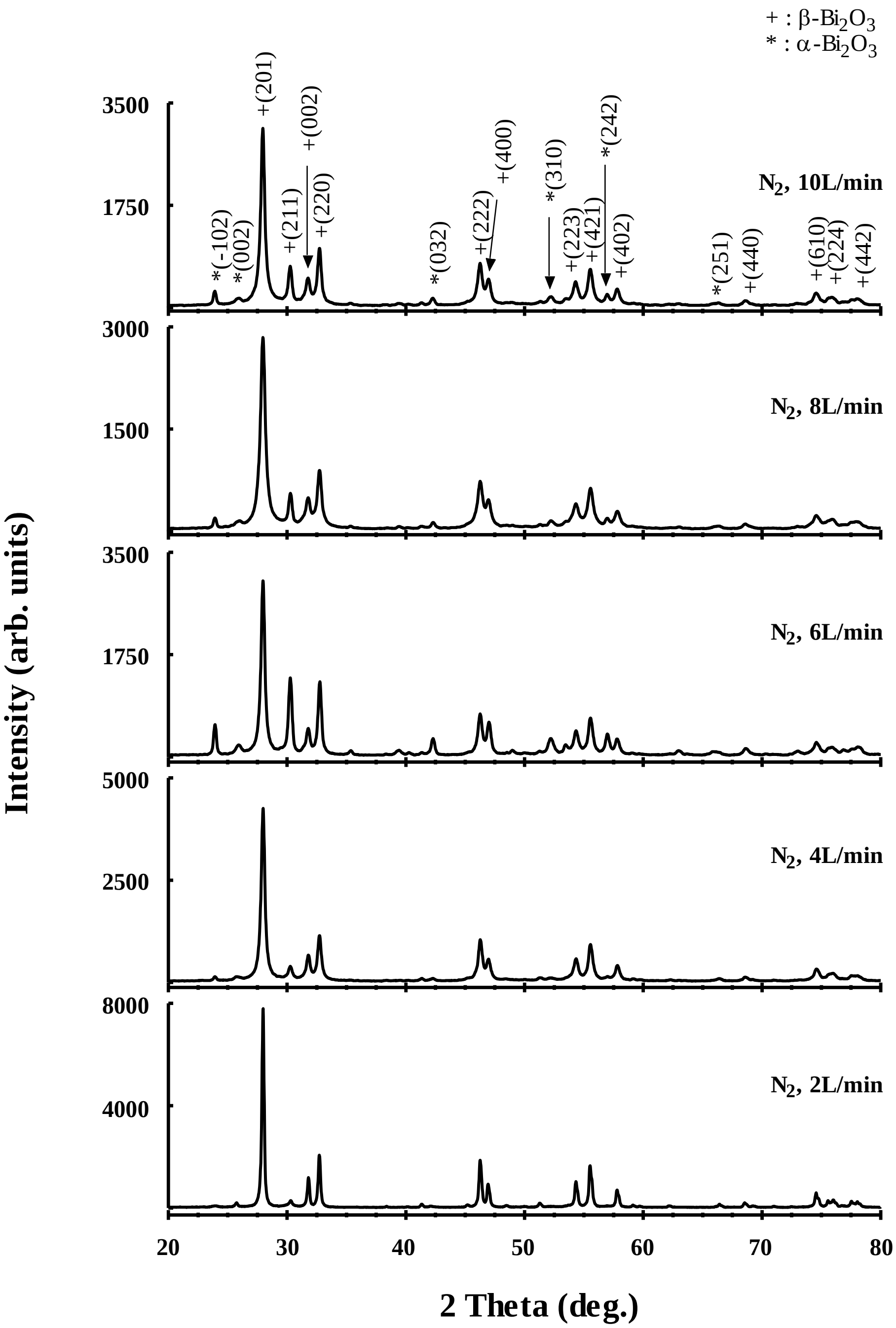

Fig. 5.1.c. XRD patterns of mixed-phases of Bi_2O_3 (β-, and α-Bi_2O_3) powders prepared by MWC at synthesis temperature 1100°C and different N_2 flow rates. N_2 flow rate is indicated on each pattern.

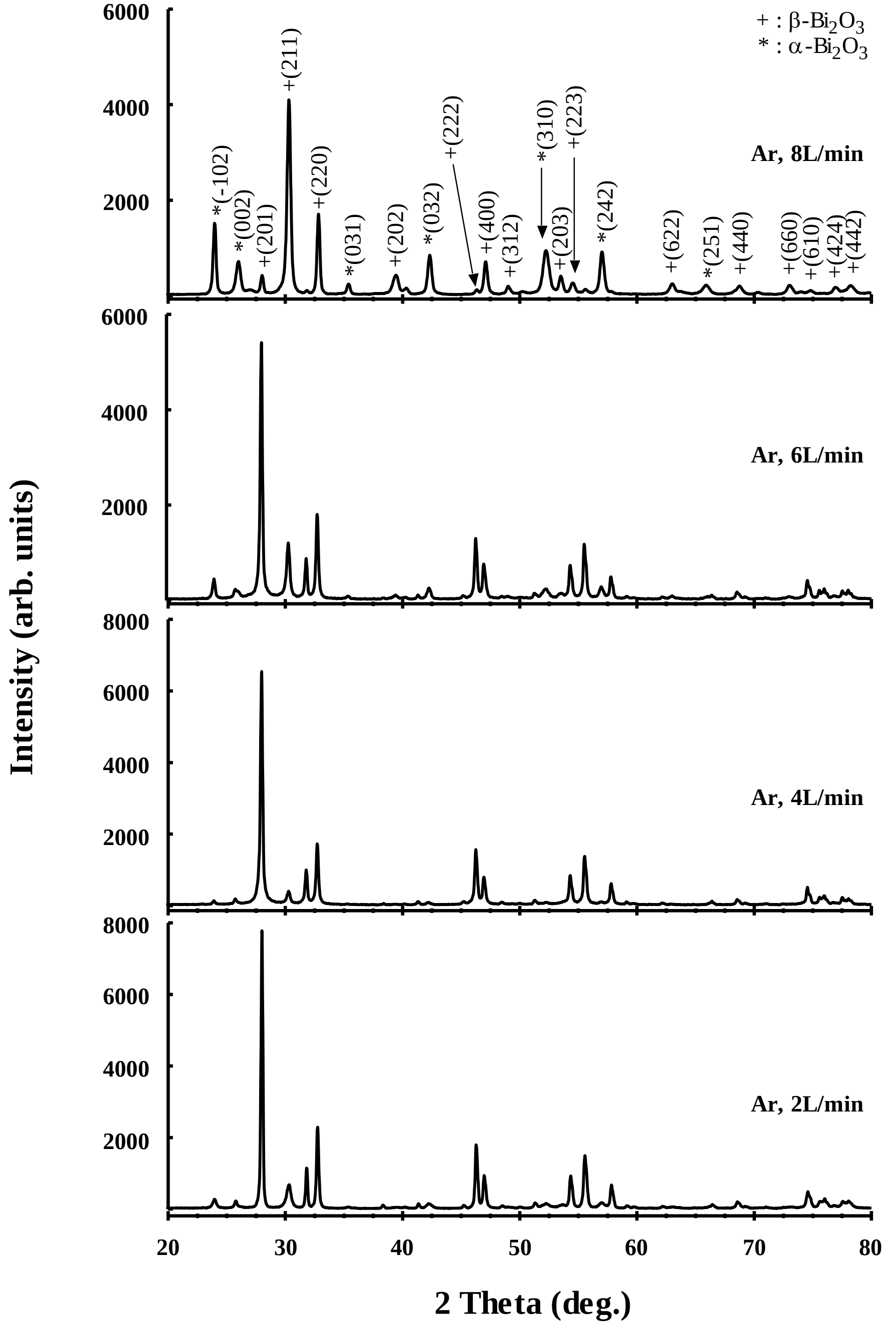

Fig. 5.2.a. XRD patterns of mixed-phases of Bi_2O_3 (β-, and α-Bi_2O_3) powders prepared by MWC at synthesis temperature 900°C and different Ar flow rates. Ar flow rate is indicated on each pattern.

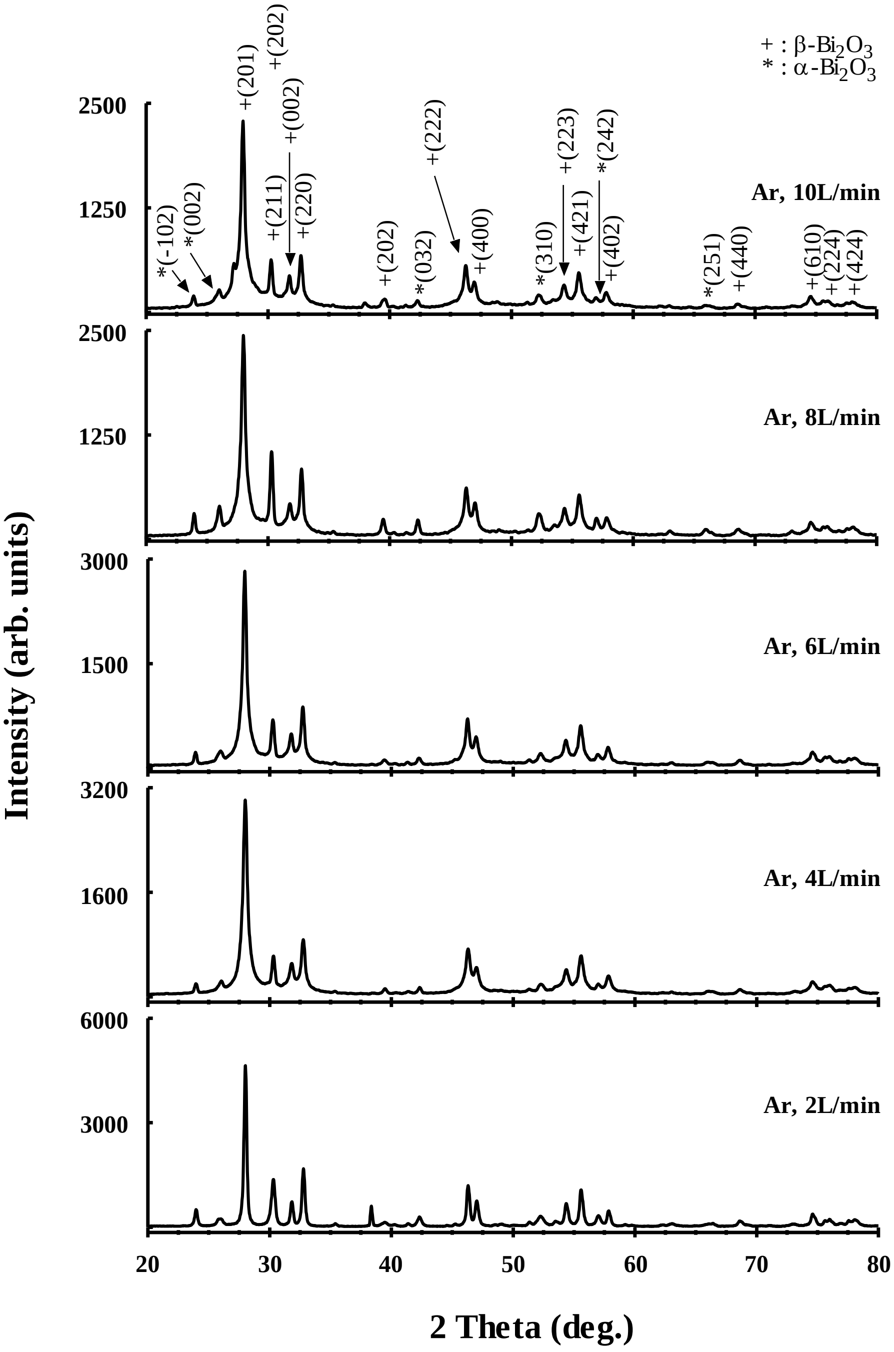

Fig. 5.2.b. XRD patterns of mixed-phases of Bi_2O_3 (β-, and α-Bi_2O_3) powders prepared by MWC at synthesis temperature 1000°C and different Ar flow rates. Ar flow rate is indicated on each pattern.

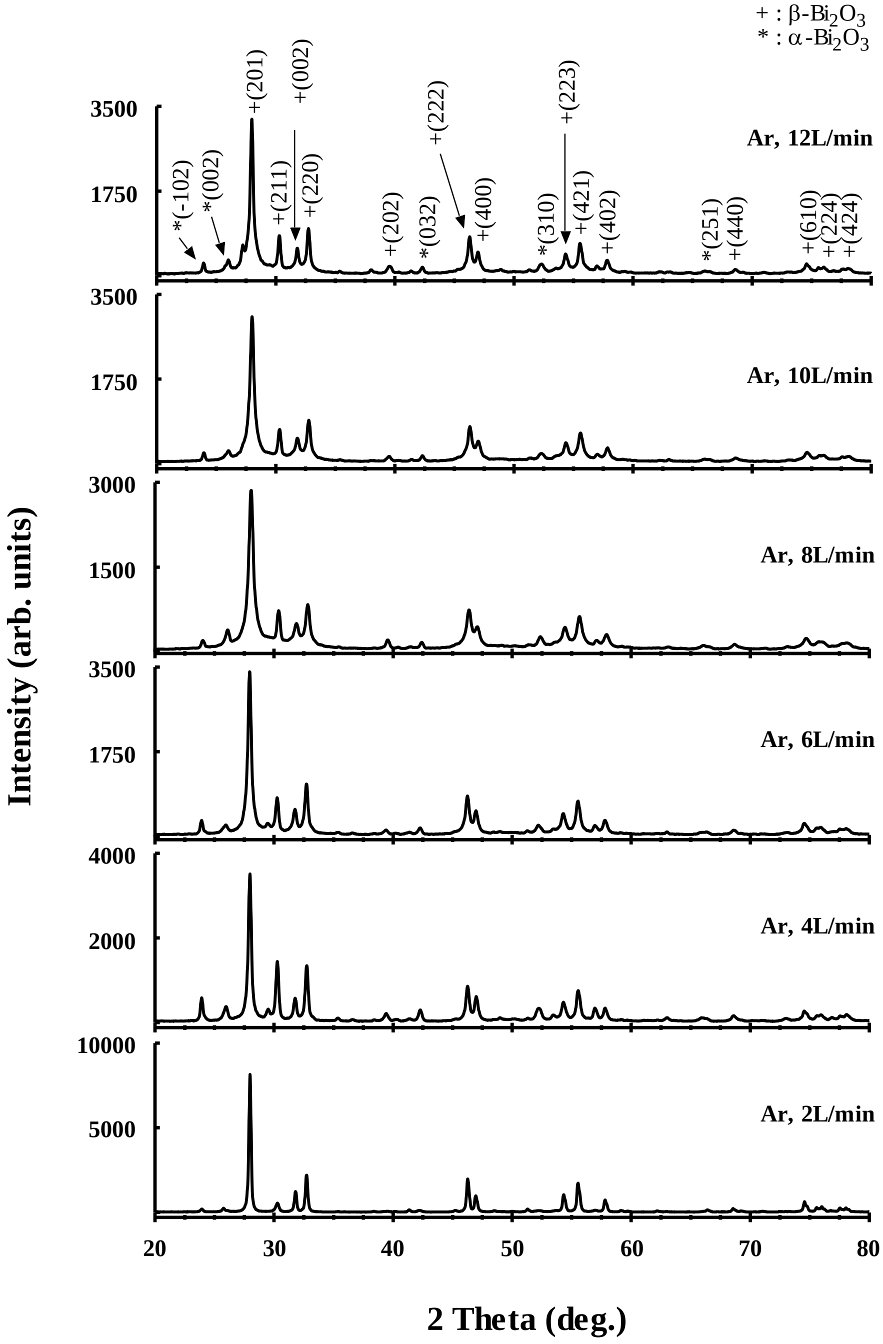

Fig. 5.2.c. XRD patterns of mixed-phases of Bi_2O_3 (β-, and α-Bi_2O_3) powders prepared by MWC at synthesis temperature 1100°C and different Ar flow rates. Ar flow rate is indicated on each pattern.

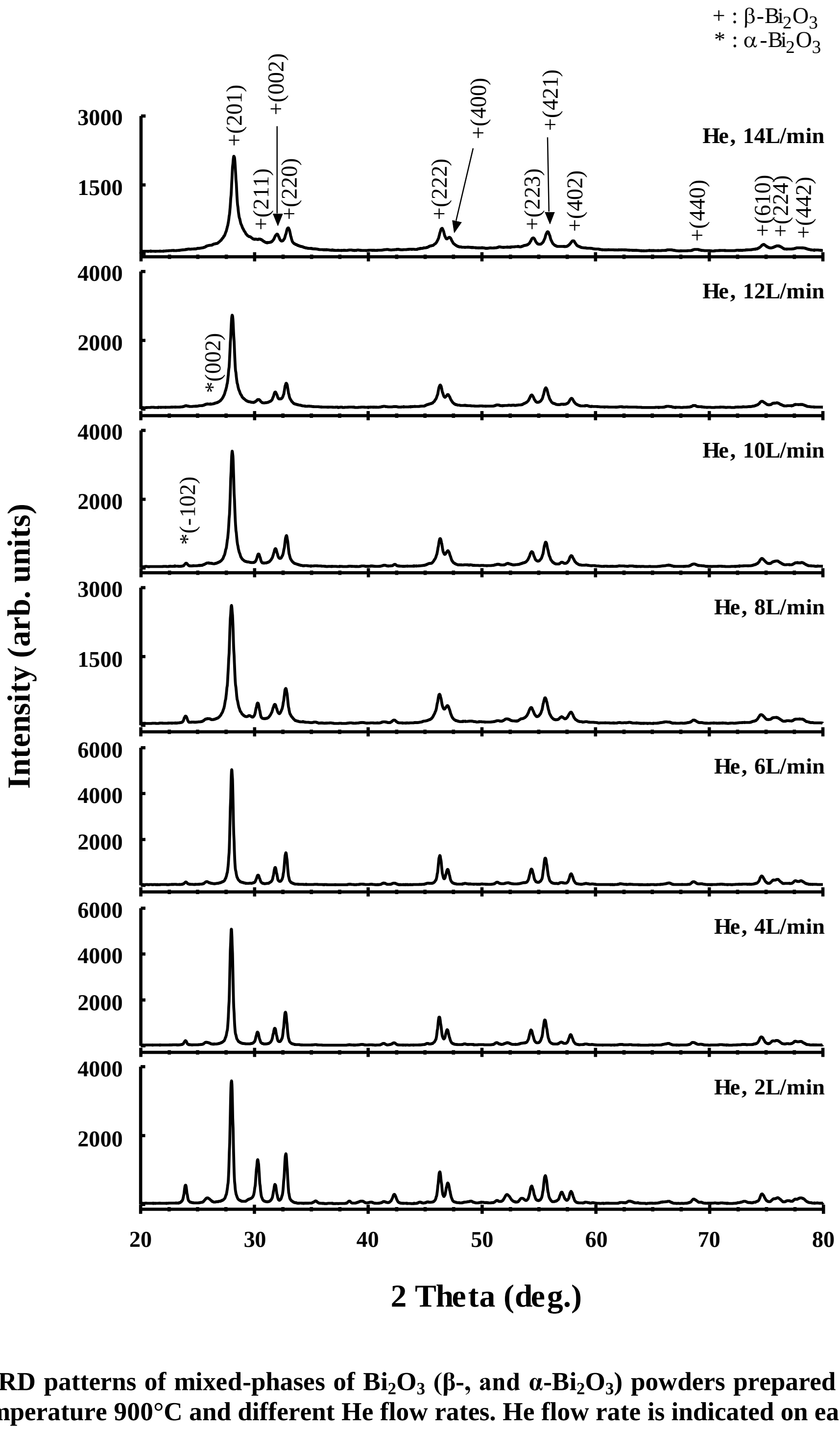

Fig. 5.3.a. XRD patterns of mixed-phases of Bi_2O_3 (β-, and α-Bi_2O_3) powders prepared by MWC at synthesis temperature 900°C and different He flow rates. He flow rate is indicated on each pattern.

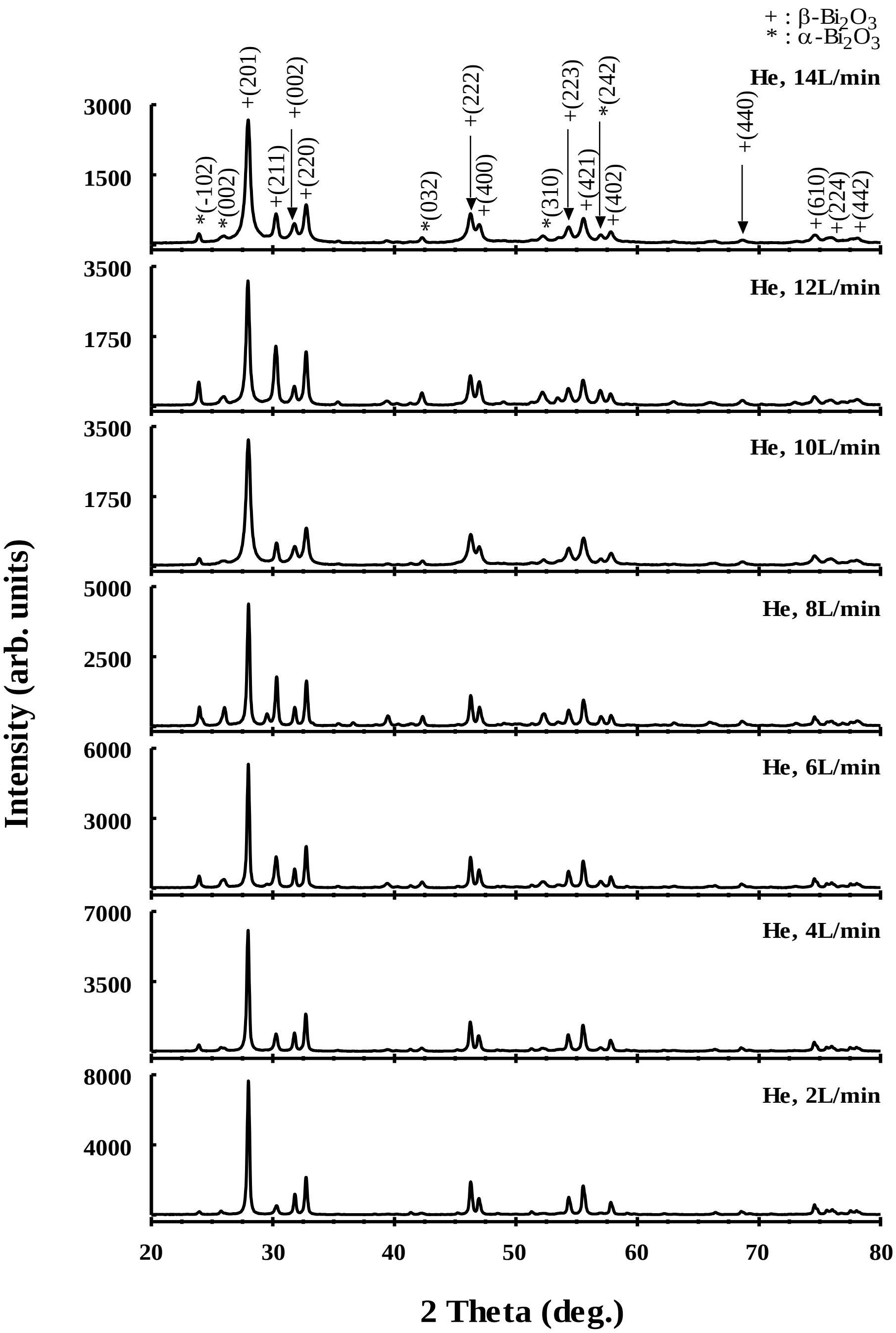

Fig. 5.3.b. XRD patterns of mixed-phases of Bi_2O_3 (β-, and α-Bi_2O_3) powders prepared by MWC at synthesis temperature 1000°C and different He flow rates. He flow rate is indicated on each pattern.

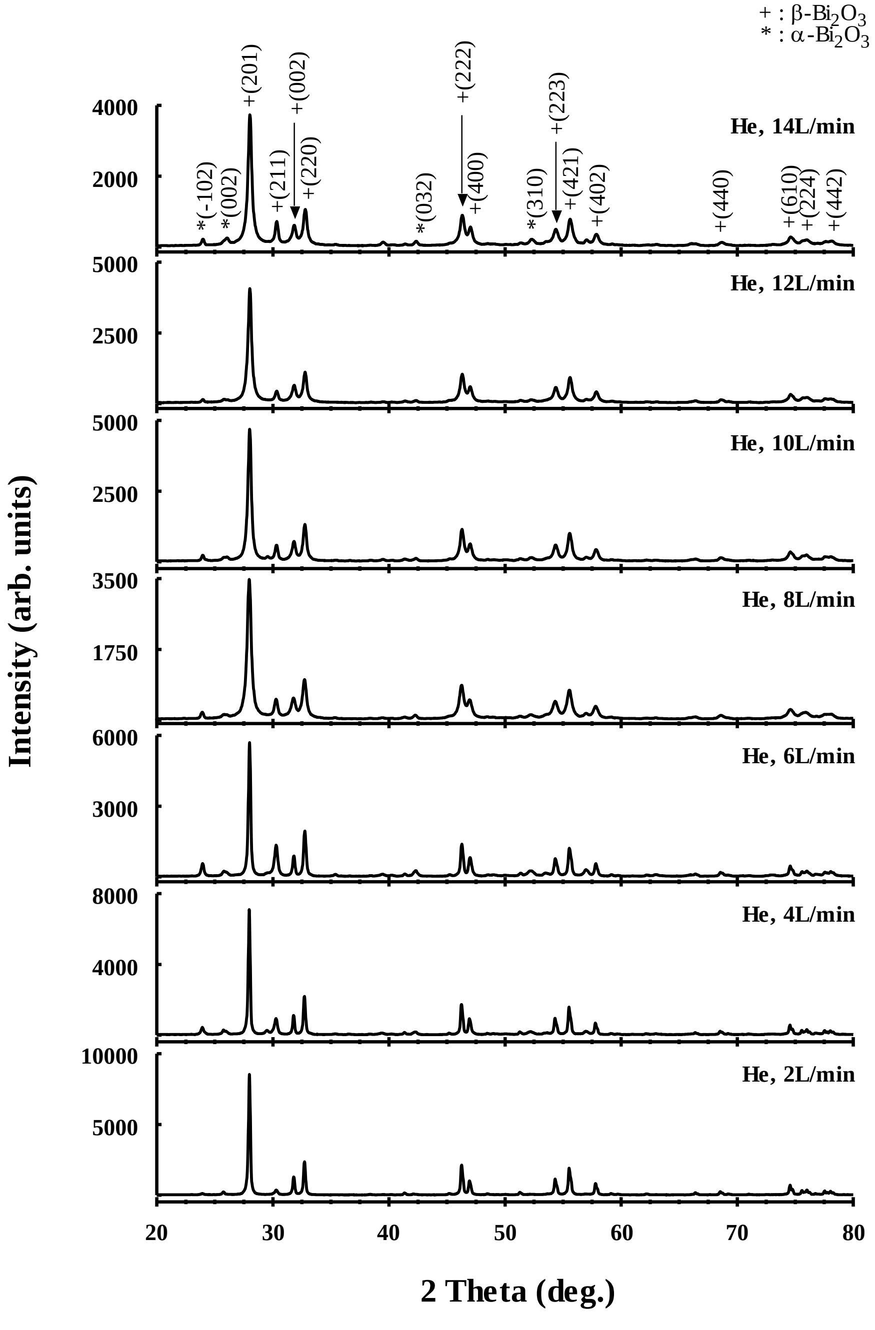

Fig. 5.3.c. XRD patterns of mixed-phases of Bi_2O_3 (β-, and α-Bi_2O_3) powders prepared by MWC at synthesis temperature 1100°C and different He flow rates. He flow rate is indicated on each pattern.

Table 5.1. Crystallite size values of all Bi_2O_3 samples, as measured by XRD.

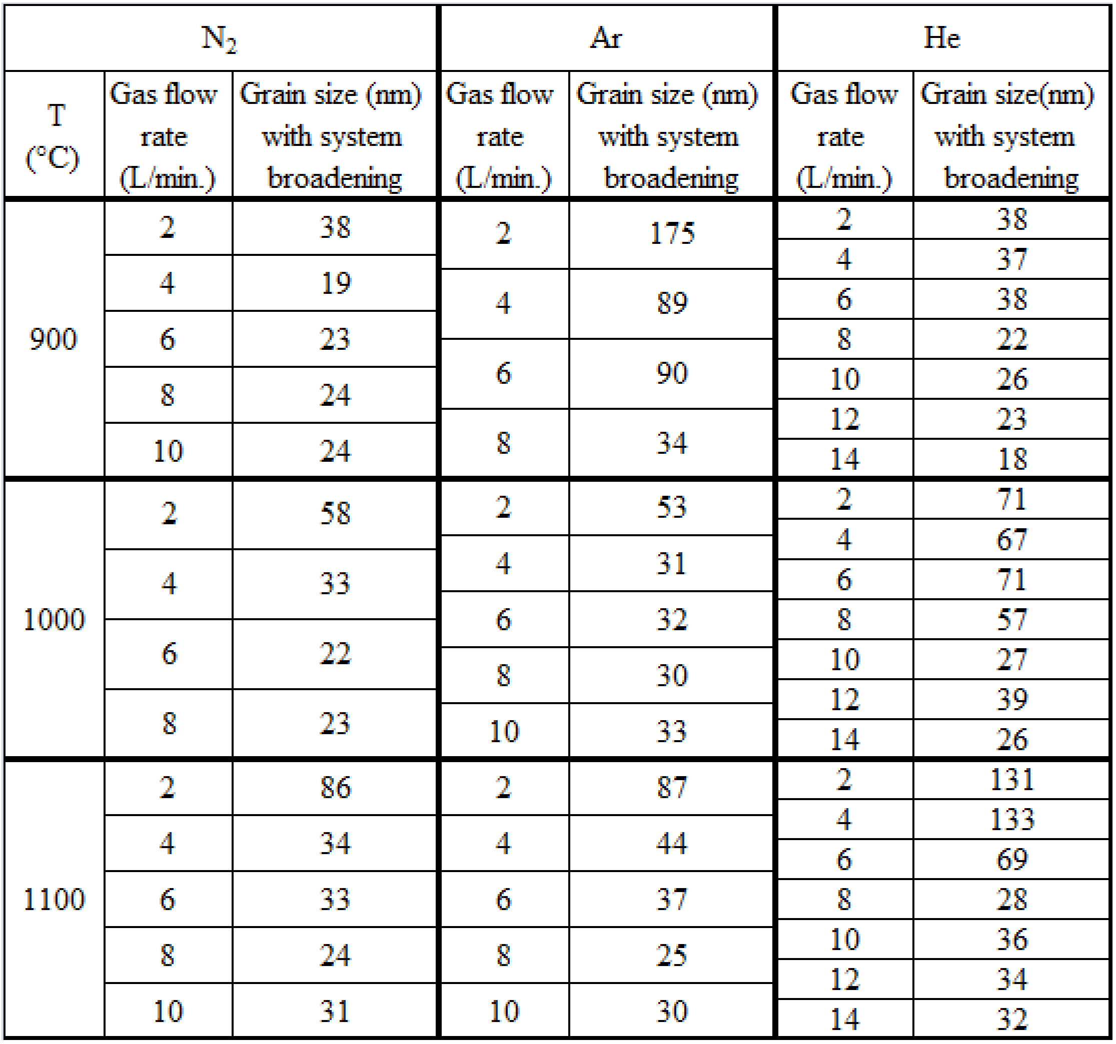

	N_2		Ar		He	
T (°C)	Gas flow rate (L/min.)	Grain size (nm) with system broadening	Gas flow rate (L/min.)	Grain size (nm) with system broadening	Gas flow rate (L/min.)	Grain size(nm) with system broadening
900	2	38	2	175	2	38
	4	19	4	89	4	37
	6	23	6	90	6	38
	8	24	8	34	8	22
	10	24			10	26
					12	23
					14	18
1000	2	58	2	53	2	71
	4	33	4	31	4	67
	6	22	6	32	6	71
	8	23	8	30	8	57
			10	33	10	27
					12	39
					14	26
1100	2	86	2	87	2	131
	4	34	4	44	4	133
	6	33	6	37	6	69
	8	24	8	25	8	28
	10	31	10	30	10	36
					12	34
					14	32

It was found that at a fixed carrier gas flow rate, the mean crystallite size of the powder increased when the synthesis temperature increased, except at a synthesis temperature of 900°C in the case of Ar, where we noticed that the crystallite size increased compared to that at 1000°C and 1100°C, for some reason that we don' know. This result was expected, since at high synthesis temperature the evaporation rate is high and results in higher growth rate due to the increase in vapor density. Variation of the mean crystallite size with the synthesis temperature at fixed flow rate of N_2, Ar and He is shown in Fig. 5.4.

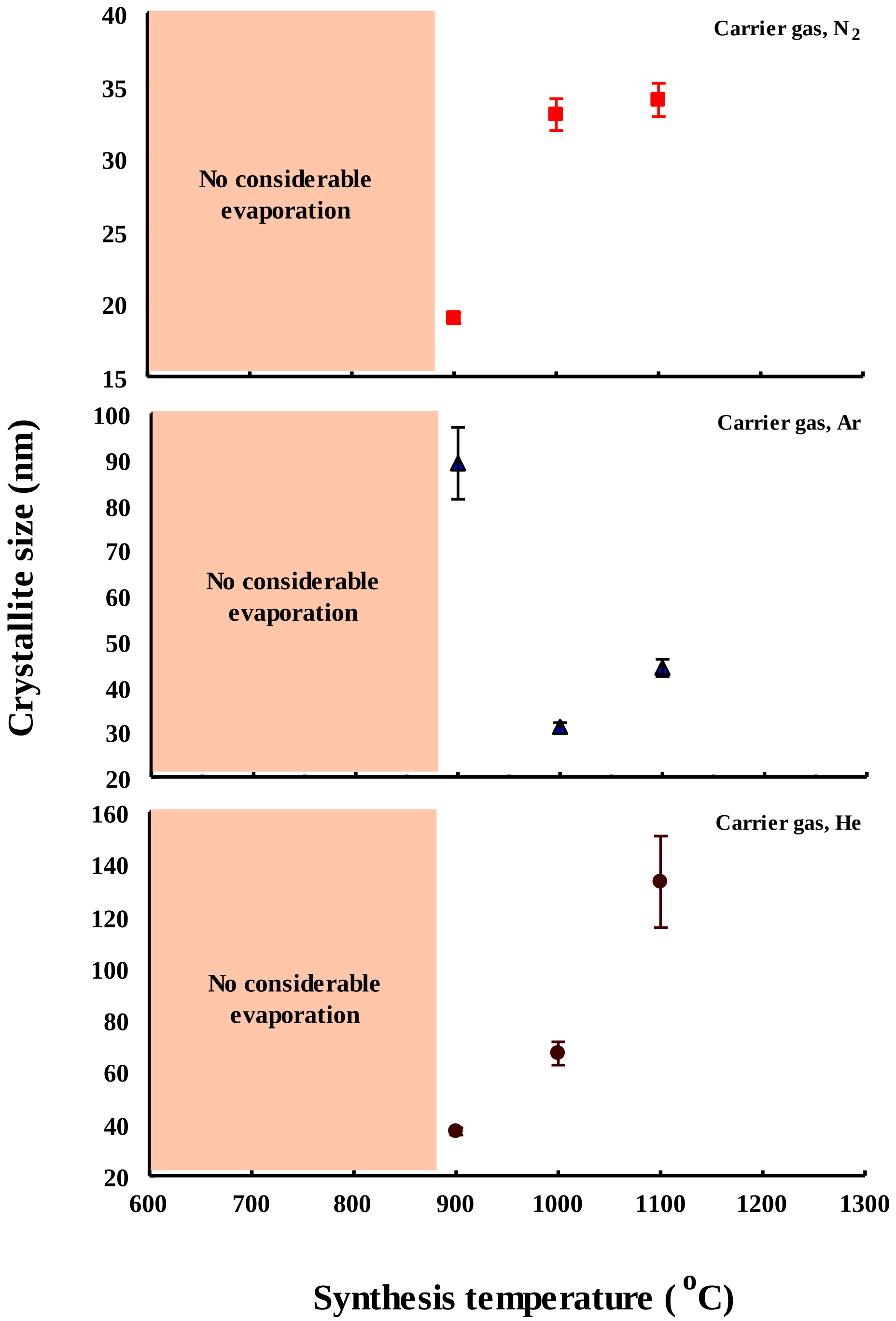

Fig. 5.4. Variation of crystallite size of the prepared Bi_2O_3 powder with different synthesis temperatures at 4L/min flow rate of N_2, Ar and He.

It can also be observed that although the crystallite size increased as the synthesis temperature increased for all carrier gases, the greatest increase was in the case of He compared to N_2. This effect can be attributed to the atomic mass of each carrier gas. It is well known that the collision rate is determined by the mean free path of the particles. The presence of a carrier gas with metal vapor will affect the vapor droplet mobility, thus its growth rate. This screening depends on the carrier gas molar mass and its pressure. The effect of carrier gas atomic mass on the nucleation rate can be understood from the fact that the absorbed momentum in collision depends on the masses of the colliding particle. The smaller/larger mass will absorb small/large amount from the larger/small mass. Thus, the smaller atomic mass of the carrier gas the larger the metal droplet size and vice versa [68].

5.1.3. Carrier gas flow rate effect

The effect of carrier gas flow rate on the properties of the synthesized bismuth oxide powder was investigated by fixing the gas type and the synthesis temperature and changing the carrier gas flow rates. As can be seen from Fig. 5.5, the mean crystallite size of the powder generally decreases when the carrier gas flow rate increases. This observation can be attributed to the reduction in the metal vapor density before it exits to the microwave cavity. This result is in good agreement with the previous study carried by Al-Quraishi [48]. However, at the highest flow rate of N_2 and Ar, the mean crystallite size of the product increased. This may be due to the low oxidation rate resulting from the high quantity of the carrier gas in the microwave cavity which leads to larger metal droplet since metal bismuth has very low melting point. So, as the metal droplet moves outside the microwave susceptor it has greater chance to grow if it is not oxidized since it is still in the liquid phase. It has also been observed by ref. [48] that, under similar circumstances when mixed metal and metal oxide produce, the mean crystallite size of the metal nanoparticle was larger than that of the metal oxide. Metal oxides generally have higher melting points than metals, thus it may be formed from the oxidization of metal droplets and instantaneously solidified, whereas metal droplets stay for long time in the liquid phase outside the microwave susceptor. As a result, the growth rate of metal oxide nanoparticles would be less than the growth of metal nanoparticles.

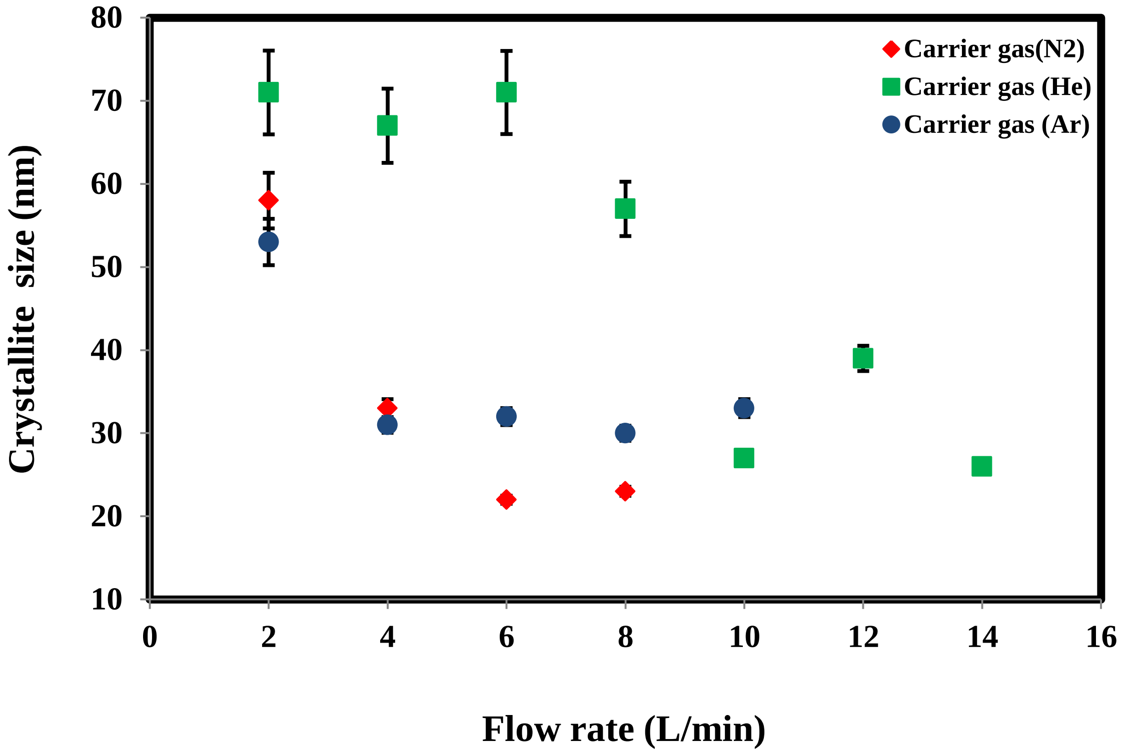

Fig. 5.5. Crystallite size of the prepared Bi_2O_3 powder versus different flow rates of N_2, Ar and He at a fixed synthesis temperature of 1000°C.

5.2. Optical studies

5.2.1. UV- visible diffuse reflectance study

To study the optical properties of the product, The normal incidence diffuse reflectance of the Bi_2O_3 powder was measured over the wavelength range 200–800 nm for all carrier gases; N_2 (Fig. 5.6), Ar (Fig. 5.7) and He (Fig. 5.8). The plateaus (maximum value) of diffuse reflectance are given in Table 5.2.

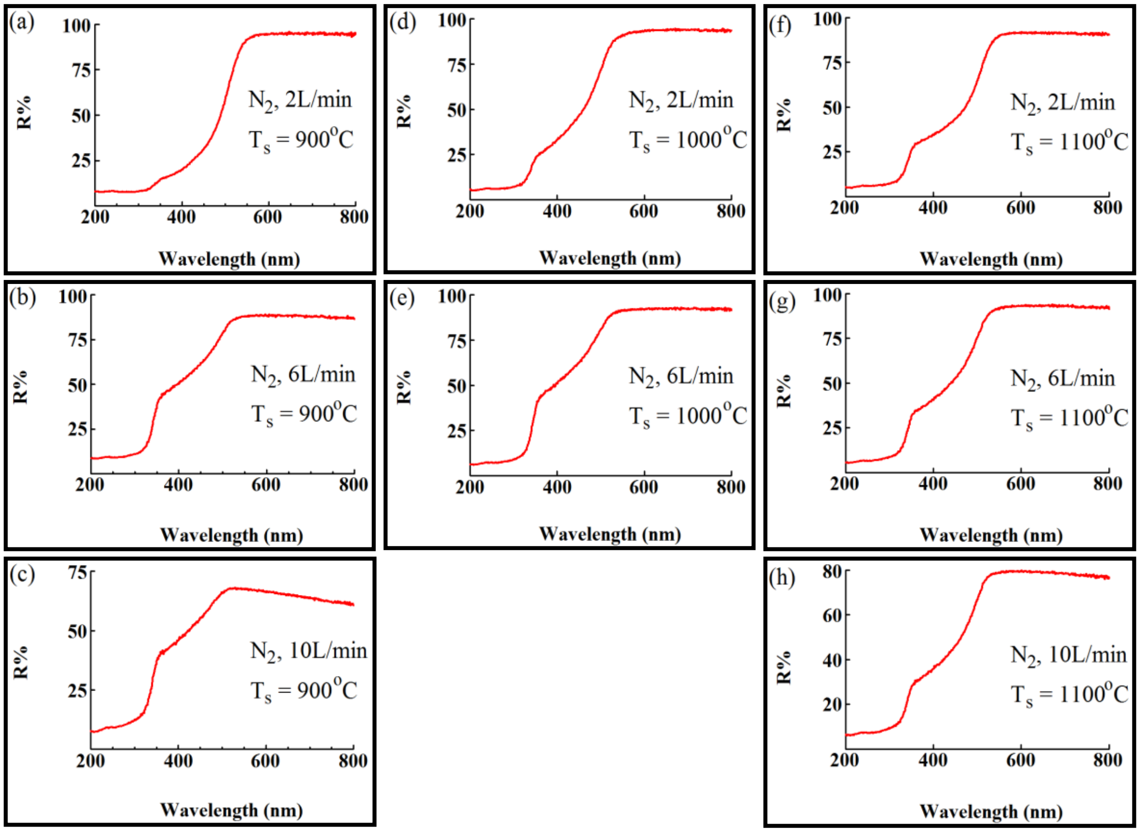

Fig. 5.6.(a-h). Diffuse reflectance spectra of the Bi_2O_3 powders prepared at different synthesis temperatures; 900, 1000 and 1100°C and different flow rates of N_2.

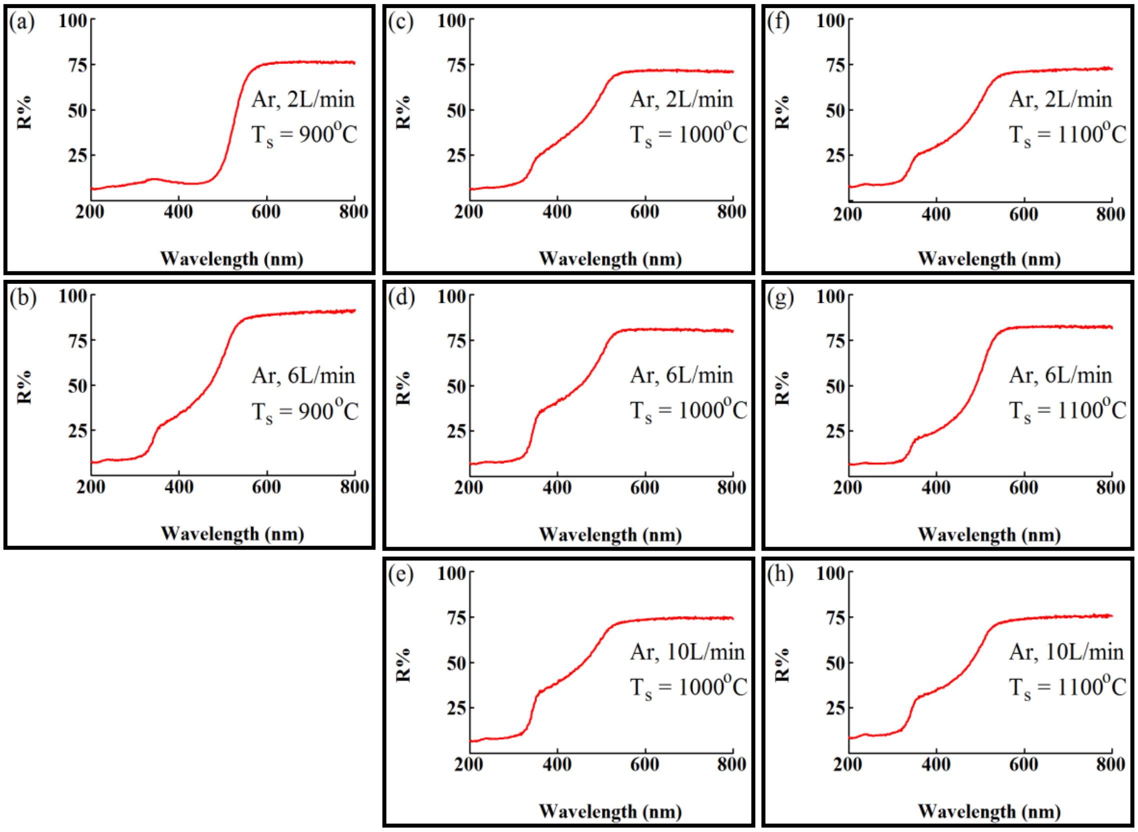

Fig. 5.7.(a-h). Diffuse reflectance spectra of the Bi_2O_3 powders prepared at different synthesis temperatures; 900, 1000 and 1100°C and different flow rates of Ar.

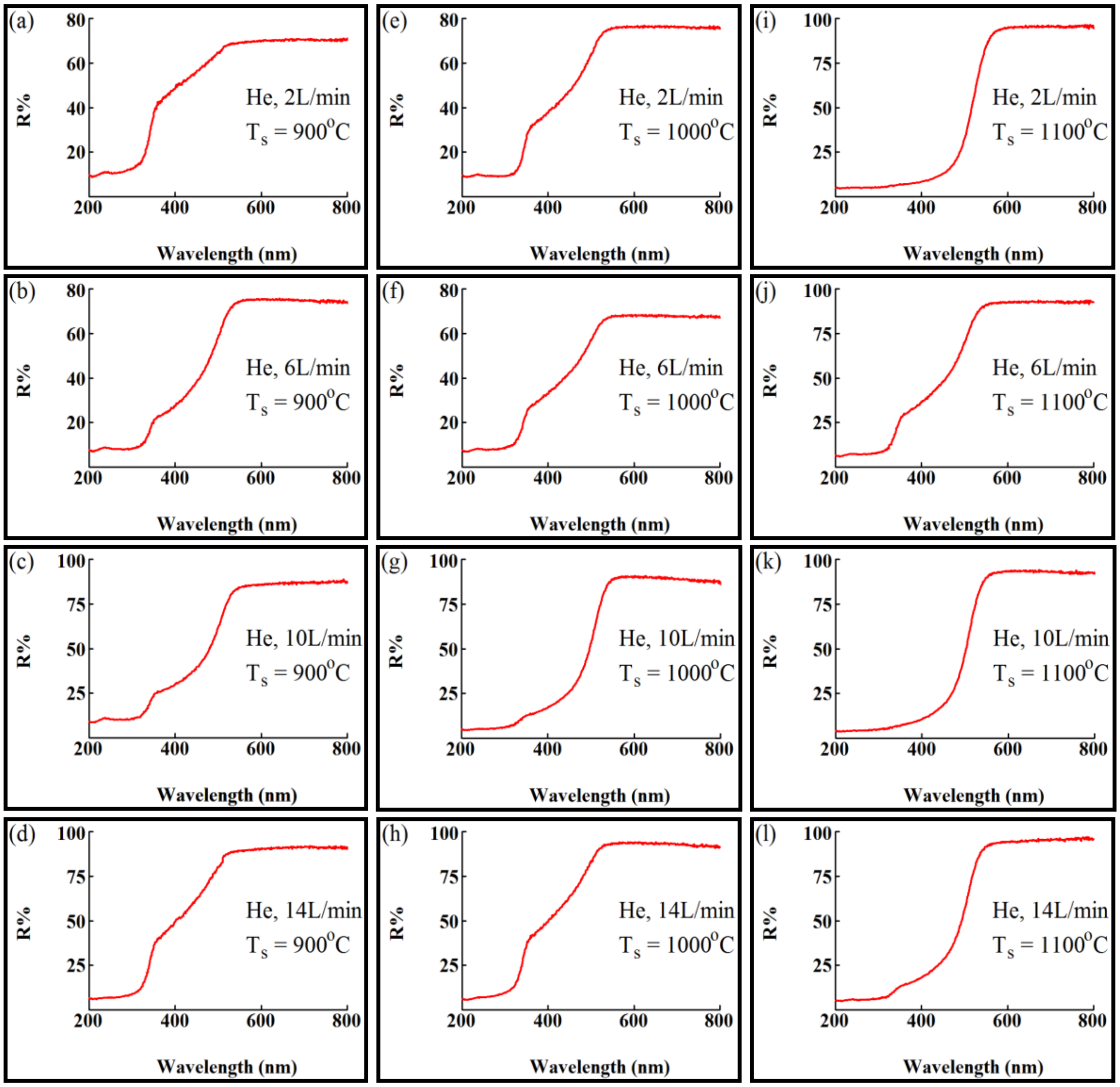

Fig. 5.8.(a-l). Diffuse reflectance spectra of the Bi_2O_3 powders prepared at different synthesis temperatures; 900, 1000 and 1100°C and different flow rates of He.

Table 5.2. The maximum values of diffuse reflectance of some samples of Bi_2O_3 powder.

Carrier gas	**Synthesis temperature (°C)**	**Flow rate (L/min)**	**R%**
N_2	900	2	94
		6	88
		10	67
	1000	2	94
		6	92
	1100	2	90
		6	92
		10	76
Ar	900	2	76
		6	90
	1000	2	71
		6	81
		10	74
	1100	2	72
		6	82
		10	75
He	900	2	70
		6	74
		10	87
		14	90
	1000	2	76
		6	67
		10	88
		14	93
	1100	2	95
		6	92
		10	93
		14	96

The Kubelka-Munk absorption coefficient (K) was calculated for each spectrum through the following relation [66]:

$$K/S = (1-R_\infty)/2\,R_\infty$$

where $R_\infty = R_{sample} / R_{standar}$. In the parabolic band structure, the band gap E_g of the semiconductor is related to the absorption coefficient α through the conventional Tauc relation [69]:

$$\alpha\, h\nu = B\,(h\nu - E_g)^{\eta}$$

where α is the linear absorption coefficient, $h\nu$ is the energy of the incident light, B is a constant . For transitions being direct allowed, direct forbidden, indirect allowed and indirect forbidden, η is 1/2, 3/2, 2 and 3, respectively. As the material of interest scatters in perfectly diffuse manner, the relation between K and α becomes ($K = 2\alpha$). In this case, the Tauc relation takes the new form,

$$K\, h\nu = A\,(h\nu - E_g)^{\eta}$$

where the Kubelka-Munk scattering coefficient S is considered as constant with respect to wavelength [66]. Hence, the optical direct band gap E_g of each sample was estimated by extrapolating the linear part of a plot of $(K\,h\nu)^2$ versus $h\nu$ that intercepts $h\nu$ axis at $K = 0$

5.2.1.1. Carrier gas flow rate and synthesis temperature effects.

Fig. 5.9, Fig. 5.10, and Fig. 5.11 show the plots of $(Kh\nu)^2$ against $h\nu$ for the estimation of the direct band gaps of the products in the presence of the carrier gases N_2, Ar and He, respectively at different synthesis temperatures, 900, 1000 and 1100°C. For each carrier gas, the band gap was obtained at each synthesis temperature and different flow rates. It can be observed from the figures that the band gap increases with the increase in the carrier gas flow rate at all synthesis temperatures. This increase in the values of the band gap is due to the reduction of the crystallite size. This increase may be attributed to the quantum size effect which results in the modification of the band structure, narrowing of both the conduction and valance bands [55]. Table 5.3 summarizes the band gap values of the investigated samples.

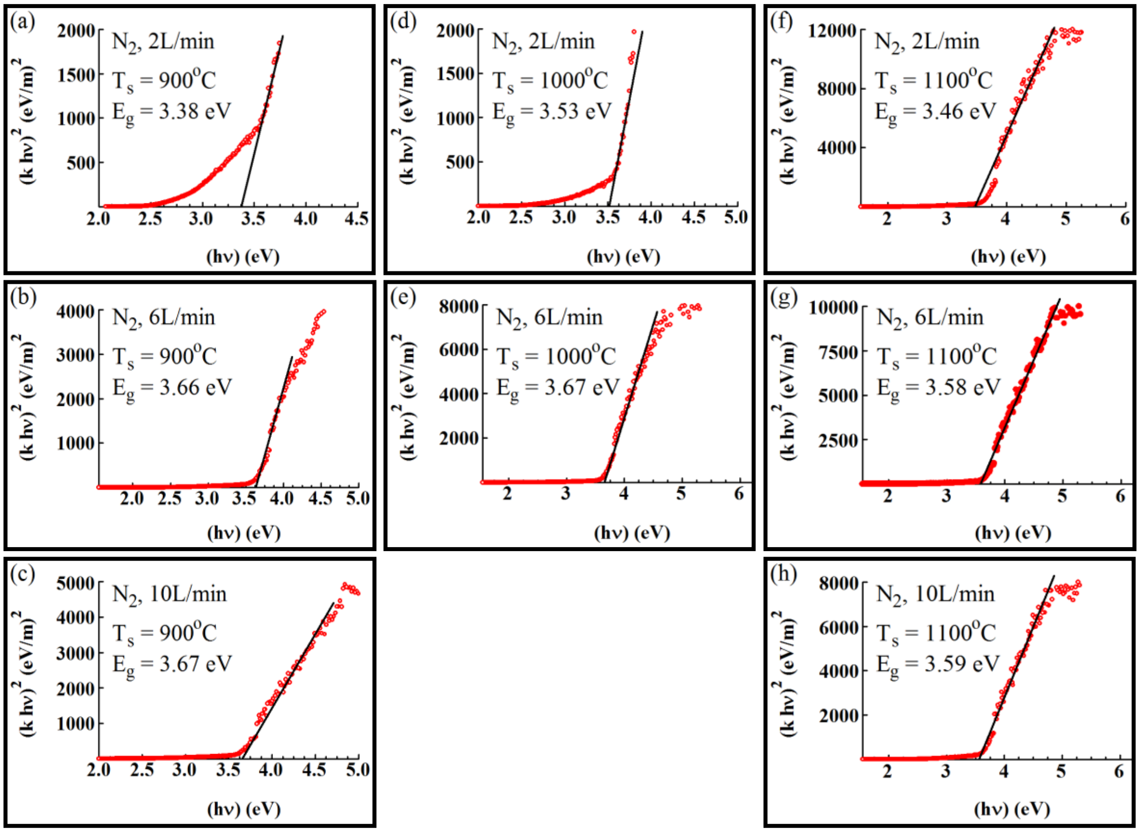

Fig. 5.9.(a-h). (Khν)^2 versus hν for the determination of band gap of Bi_2O_3 powder synthesized in the presence of N_2 as carrier gas. N_2 flow rate and synthesis temperature are indicated on each pattern.

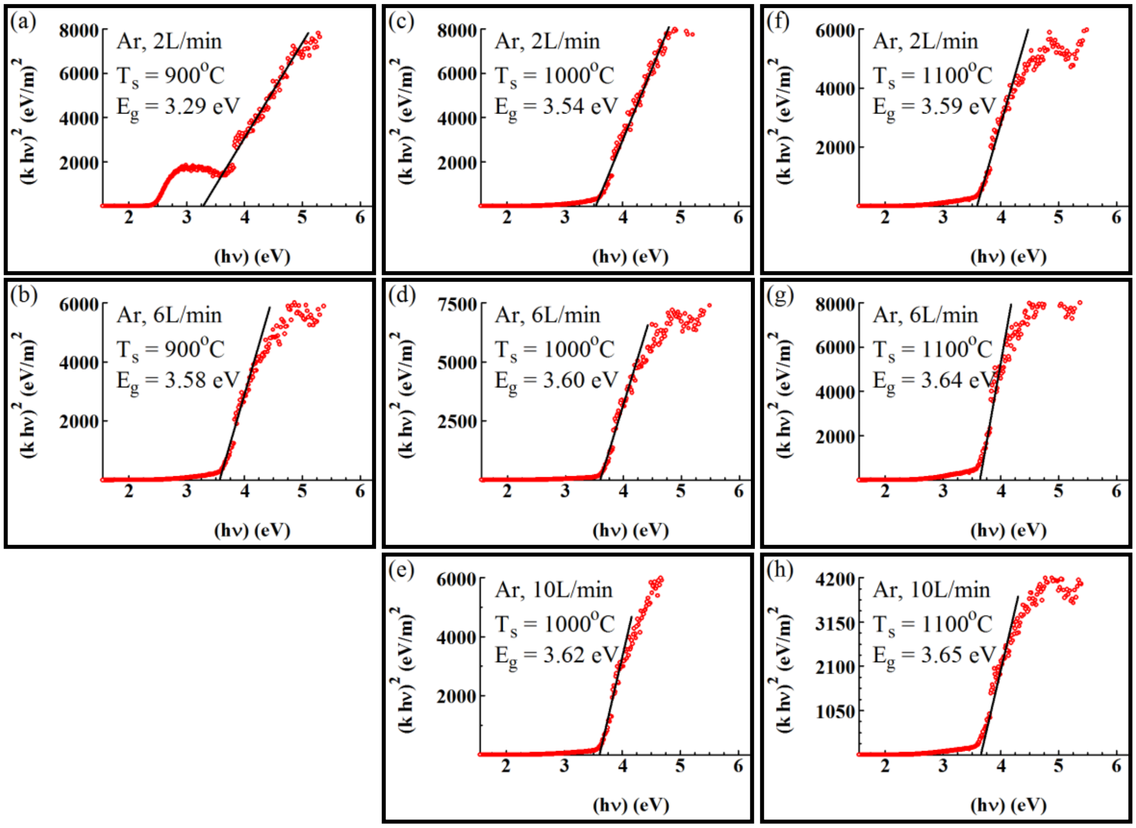

Fig. 5.10.(a-h). $(Kh\nu)^2$ versus hν for the determination of band gap of Bi_2O_3 powder synthesized in the presence of Ar as carrier gas. Ar flow rate and synthesis temperature are indicated on each pattern.

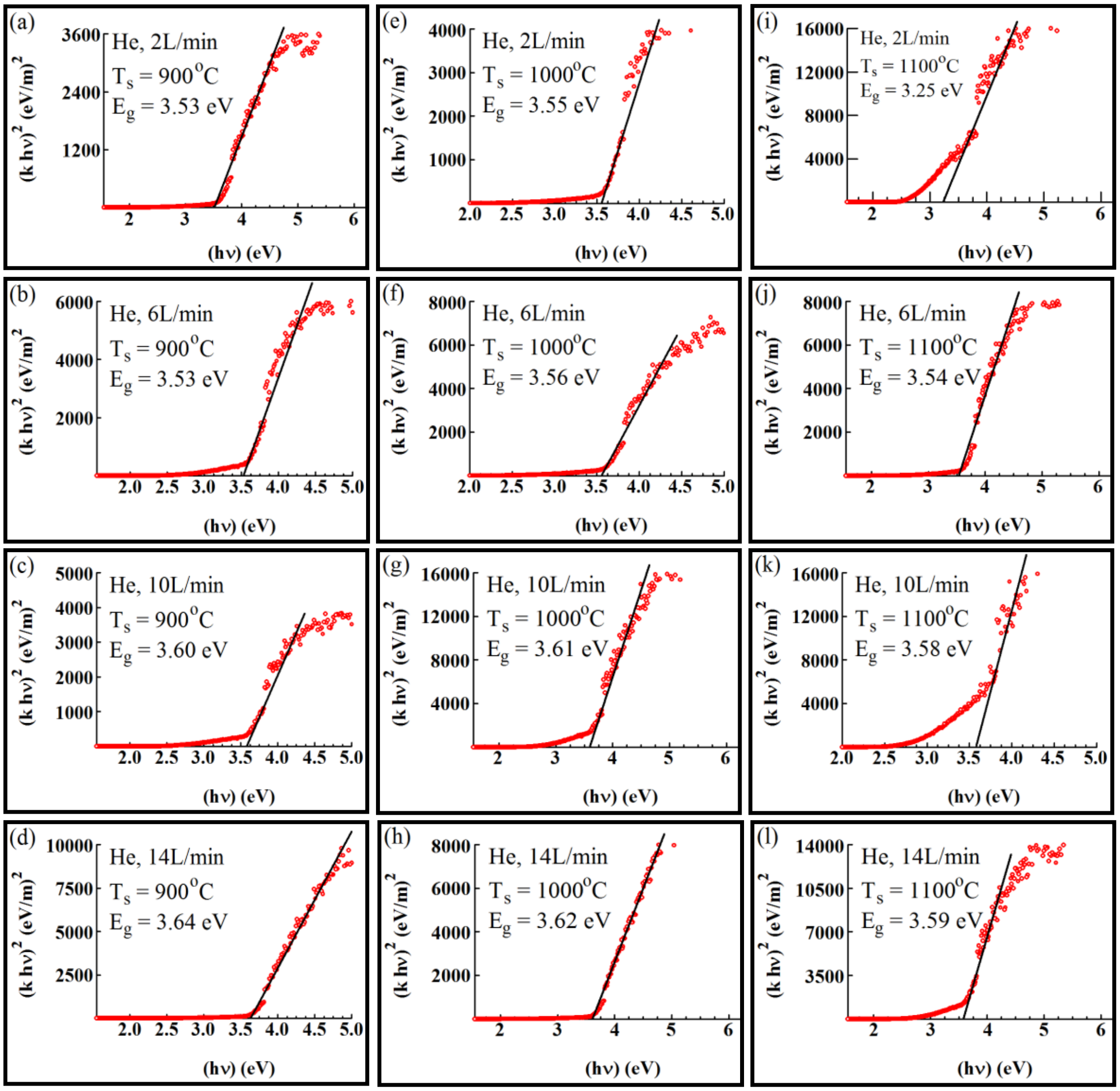

Fig. 5.11.(a-l). $(Kh\nu)^2$ versus hν for the determination of band gap of Bi_2O_3 powder synthesized in the presence of He as carrier gas. He flow rate and synthesis temperature are indicated on each pattern.

Table 5.3. Band gap values of some samples of the prepared Bi_2O_3 powder.

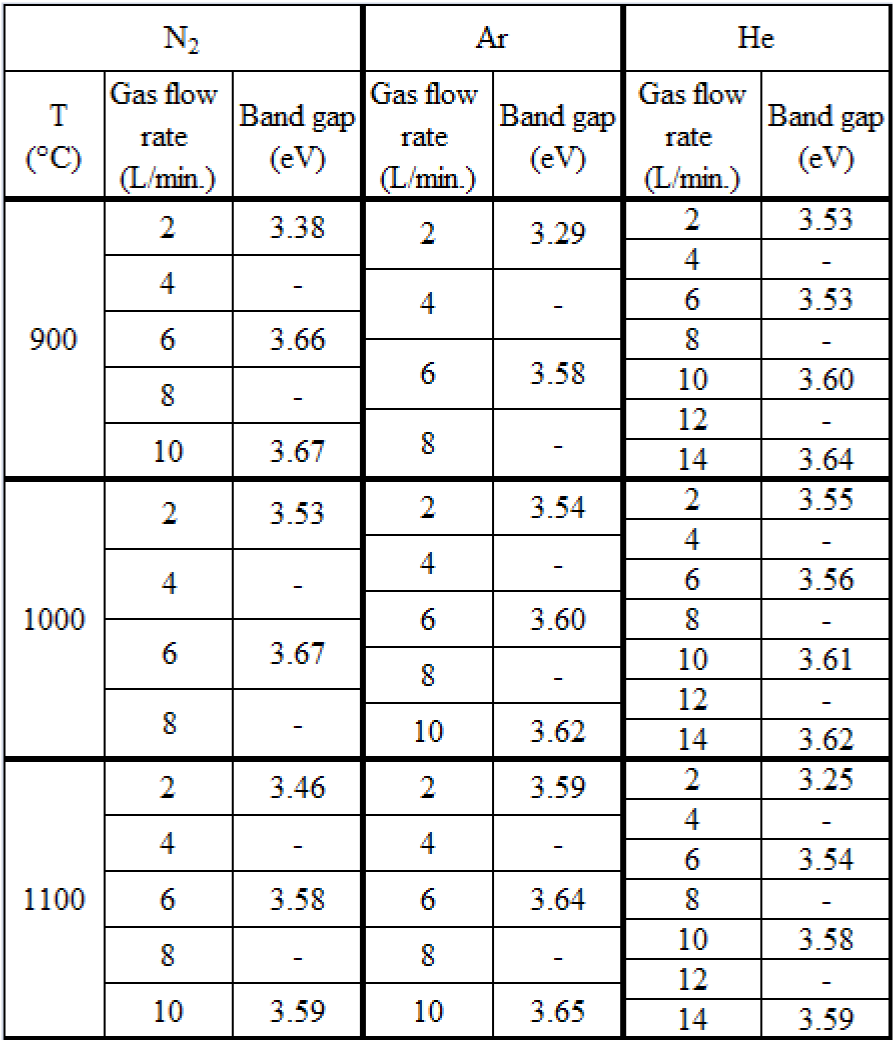

	N_2		Ar		He	
T (°C)	Gas flow rate (L/min.)	Band gap (eV)	Gas flow rate (L/min.)	Band gap (eV)	Gas flow rate (L/min.)	Band gap (eV)
900	2	3.38	2	3.29	2	3.53
	4	-	4	-	4	-
	6	3.66	6	3.58	6	3.53
	8	-	8	-	8	-
	10	3.67			10	3.60
					12	-
					14	3.64
1000	2	3.53	2	3.54	2	3.55
	4	-	4	-	4	-
	6	3.67	6	3.60	6	3.56
	8	-	8	-	8	-
			10	3.62	10	3.61
					12	-
					14	3.62
1100	2	3.46	2	3.59	2	3.25
	4	-	4	-	4	-
	6	3.58	6	3.64	6	3.54
	8	-	8	-	8	-
	10	3.59	10	3.65	10	3.58
					12	-
					14	3.59

The variation of the band gap with the flow rate of the carrier gas at all synthesis temperatures is shown in Fig. 5.12, Fig. 5.13 and Fig. 5.14 using N_2, Ar and He as carrier gases, respectively. As can be seen from the figures, the band gaps of the products were found to be in the range of 3.38 - 3.67 eV in the case of N_2 while they were in the range of 3.29 - 3.65 eV and 3.25 - 3.64 eV in the case of Ar and He, respectively. These values are in accordance with those reported for Bi_2O_3 [54, 70-71].

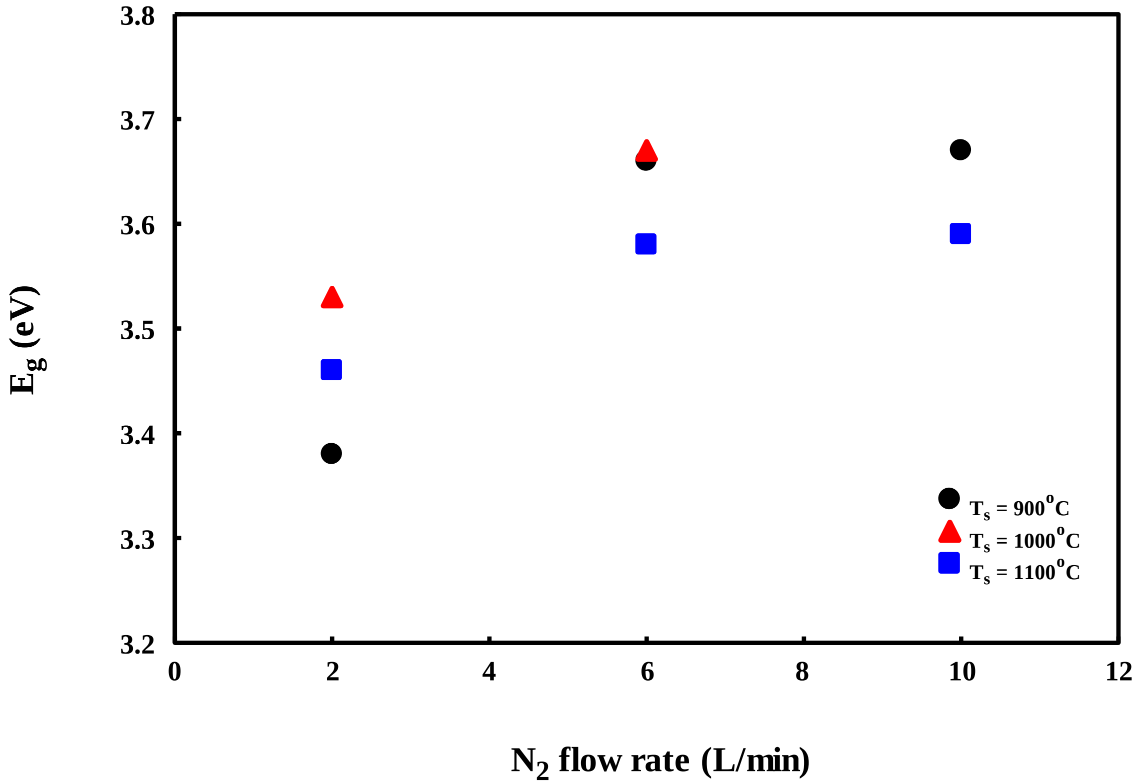

Fig. 5.12. Variation of band gap of the as- prepared Bi_2O_3 powder with N_2 flow rates.

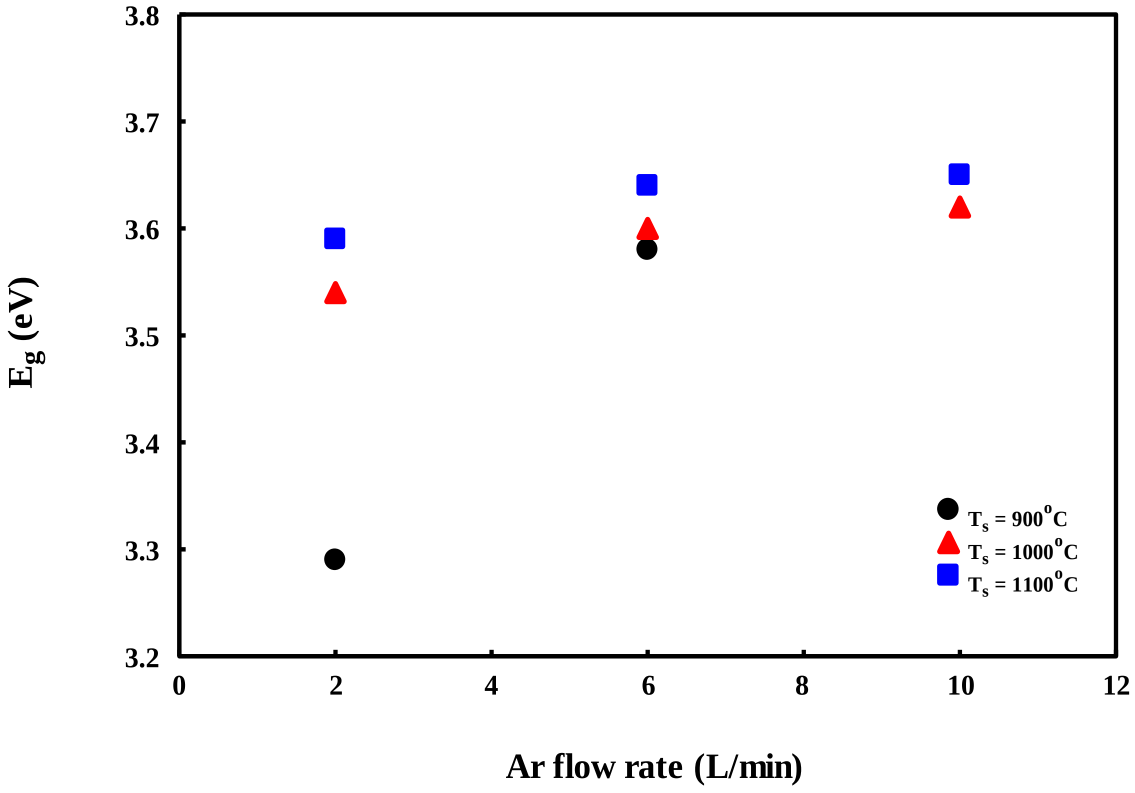

Fig. 5.13. Variation of band gap of the as- prepared Bi_2O_3 powder with Ar flow rates.

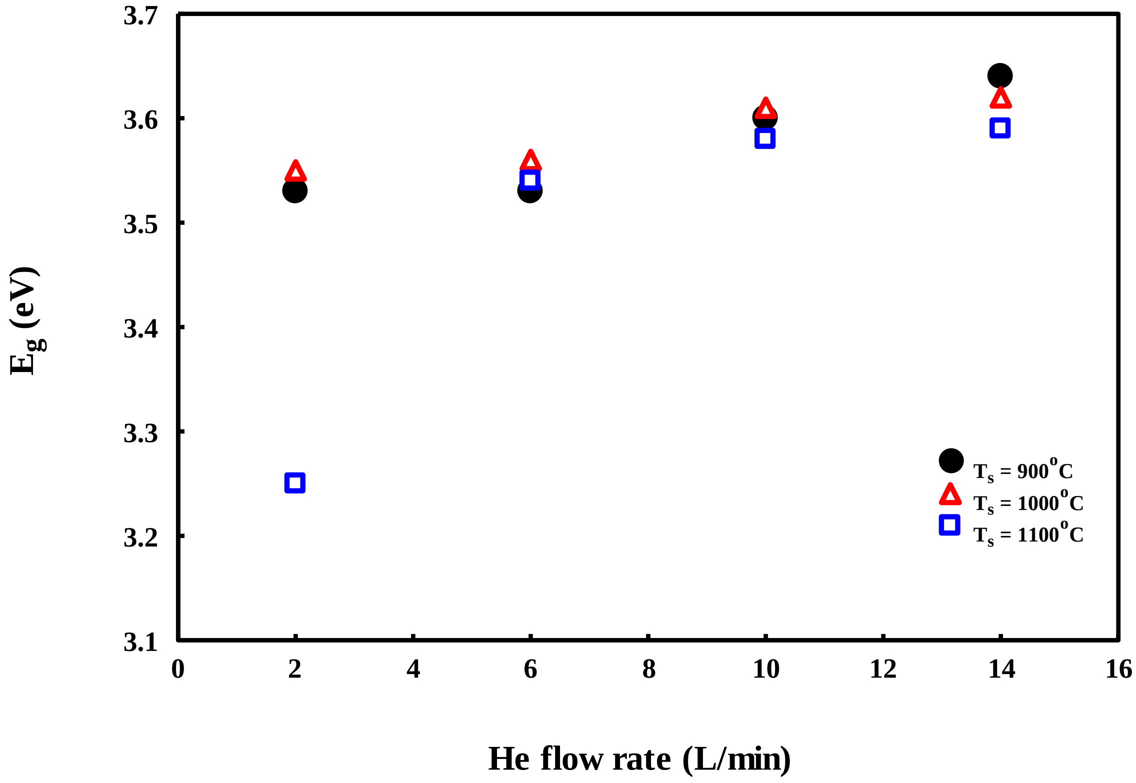

Fig. 5.14. Variation of band gap of the as- prepared Bi_2O_3 powder with He flow rates.

5.2.1.2. Carrier gas effect

The effect of the kind of the carrier gas on the optical properties of the as-prepared Bi_2O_3 powder can be inferred from the variation of the values of the band gap with the carrier gases type at fixed temperatures and fixed flow rate as shown in Fig. (5.15), Fig. (5.16) and Fig. (5.17). This variation comes from the fact that the crystallite size of the particle and the concentration of different phases of Bi_2O_3 are affected by the nature of the interaction between bismuth and oxygen due to the kind of carrier gas, which in turn affects the values of band gap of the product.

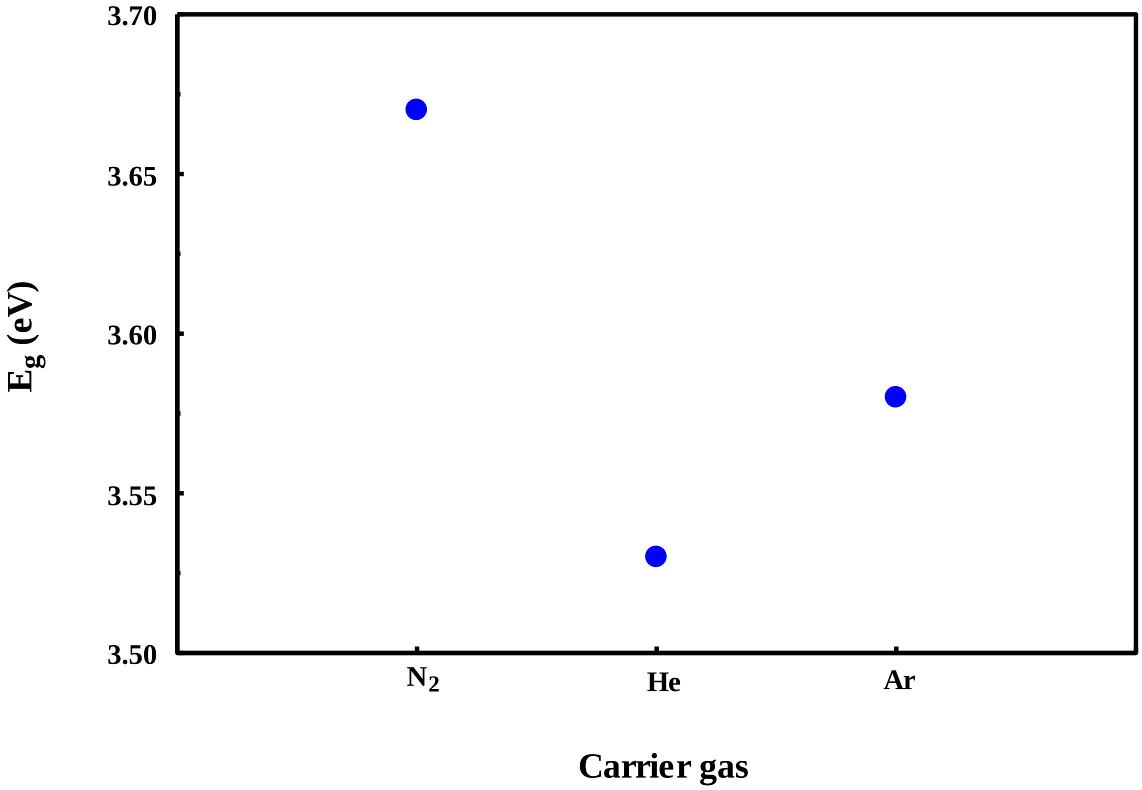

Fig. 5.15. Variation of band gap of the as- prepared Bi_2O_3 powder with the carrier gas at a synthesis temperature of 900°C and a fixed flow rate of 6L/min.

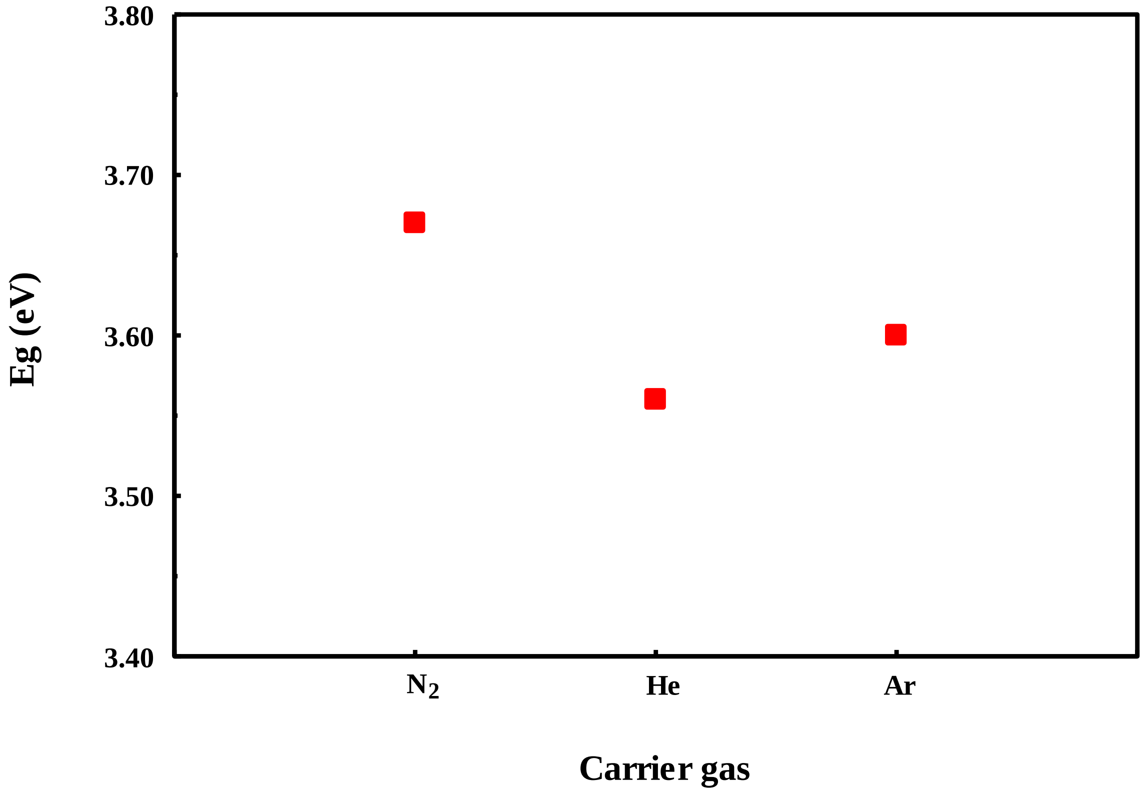

Fig. 5.16. Variation of band gap of the as- prepared Bi_2O_3 powder with the carrier gas at a synthesis temperature of 1000°C and a fixed flow rate of 6L/min.

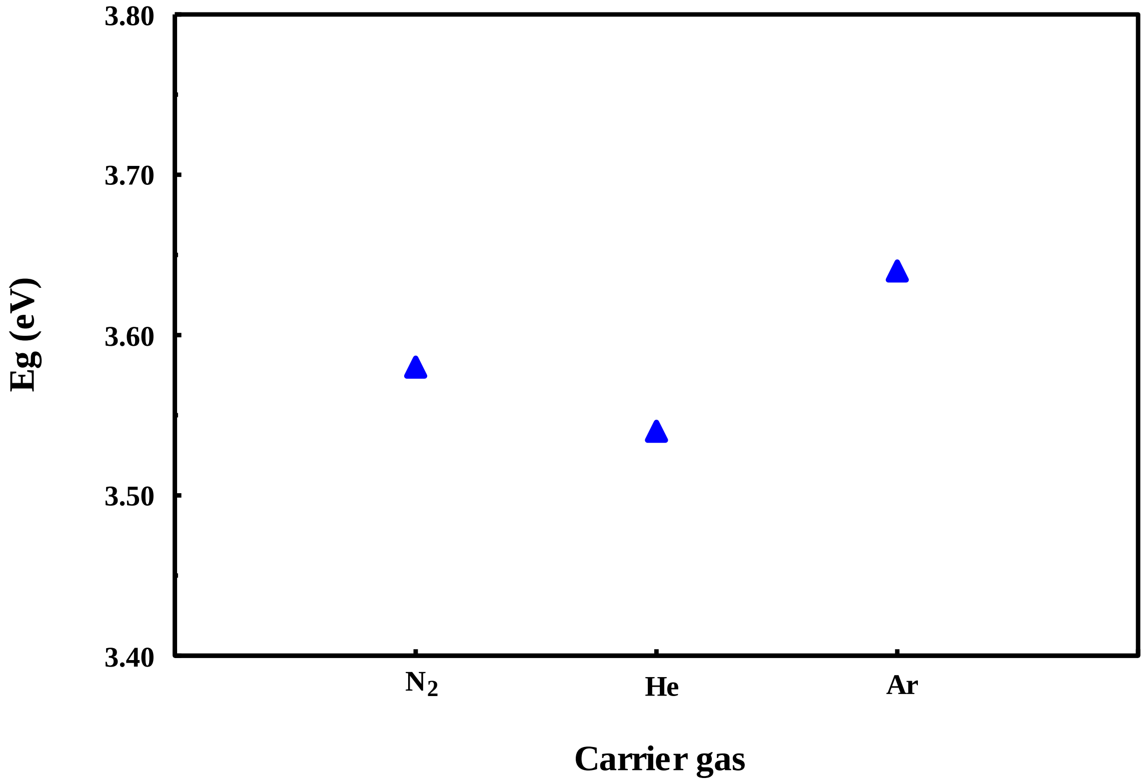

Fig. 5.17. Variation of band gap of the as- prepared Bi_2O_3 powder with the carrier gas at a synthesis temperature of 1100°C and a fixed flow rate of 6L/min.

5.3. Surface morphological analysis

A field emission scaning electron microscope (FESEM) was used for the characterization of some samples of Bi_2O_3 nanopowders prepared at a fixed synthesis temperature and different flow rates of the carrier gases. Fig. 5.18 shows a high magnification of the micrograph of the samples synthesized at N_2 flow rates of 2L/min (a), 6L/min (b) and a fixed synthesis temperature of 1000°C. Particles of plate-like morpholory are observed in the two samples.

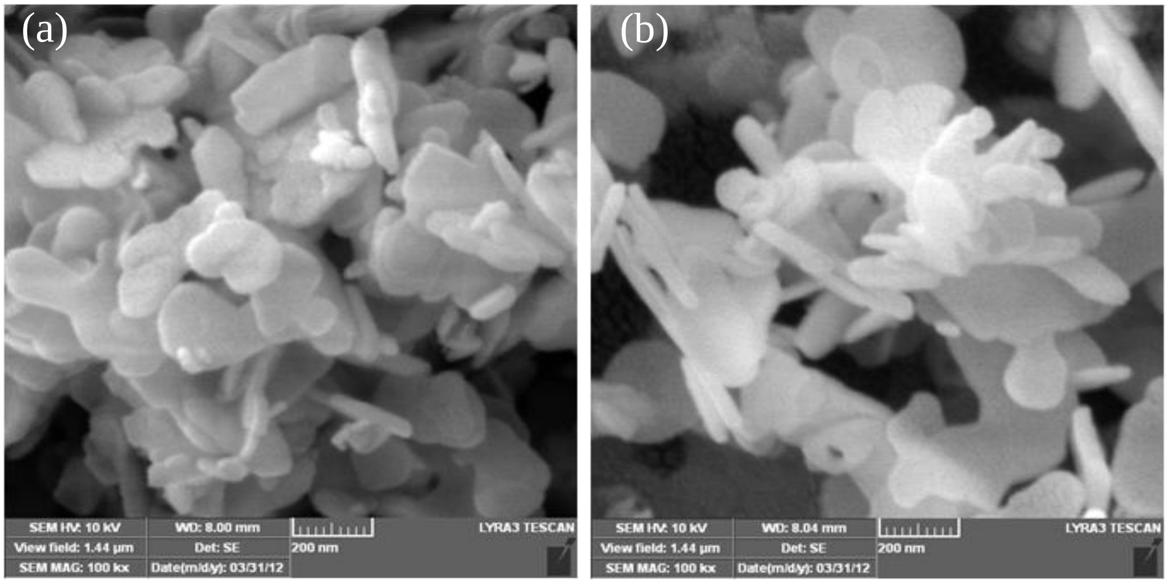

Fig. 5.18. FESEM image of highly magnified area of Bi_2O_3 powder synthesized at (a) 2L/min and (b) 6L/min flow rates of N_2 and a fixed synthesis temperature of 1000°C.

When using Ar as a carrier gas at 2L/min and 6L/min flow rates, same morphology was obtained as shown in Fig. 5.19.(a) and Fig. 5.19.(b), respectively.

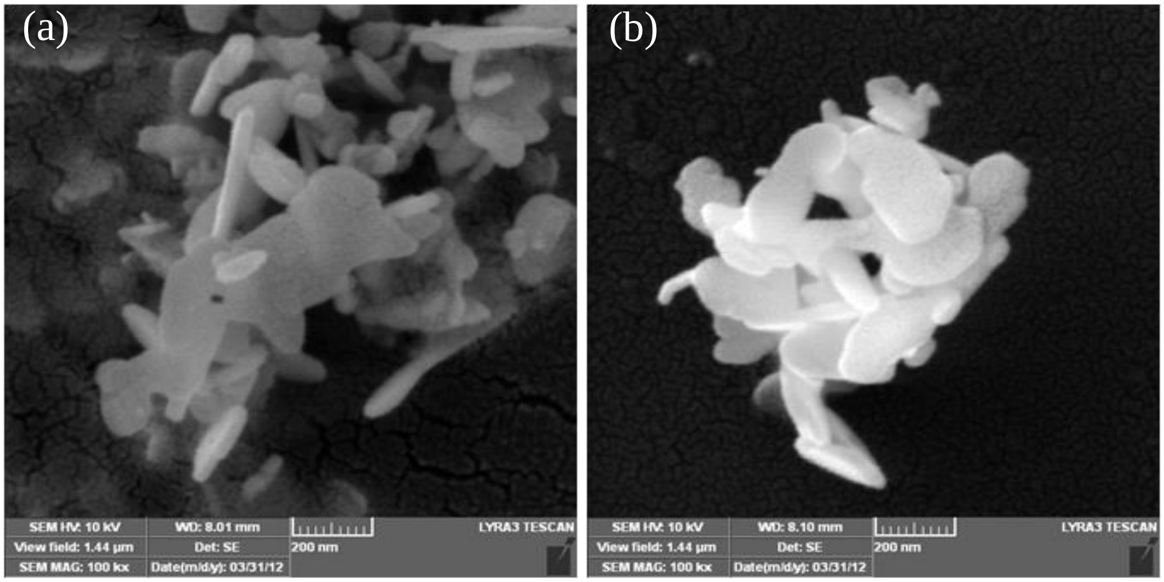

Fig. 5.19. FESEM image of highly magnified area of Bi_2O_3 powder synthesized at (a) 2L/min and (b) 6L/min flow rates of Ar and a fixed synthesis temperature of 1000°C.

Similarly, when He at flow rates of 2 L/min (Fig. 5.20.(a)) and 14L/min (Fig. 5.20.(b)) was used as a carrier gas we observed the formation of plate-like particles with an apparent agglomeration at the flow rate of 2L/min. Thus, There is no remarkable effect for the type and flow rate of the carrier gas on the morphology of the prepared Bi_2O_3 powder.

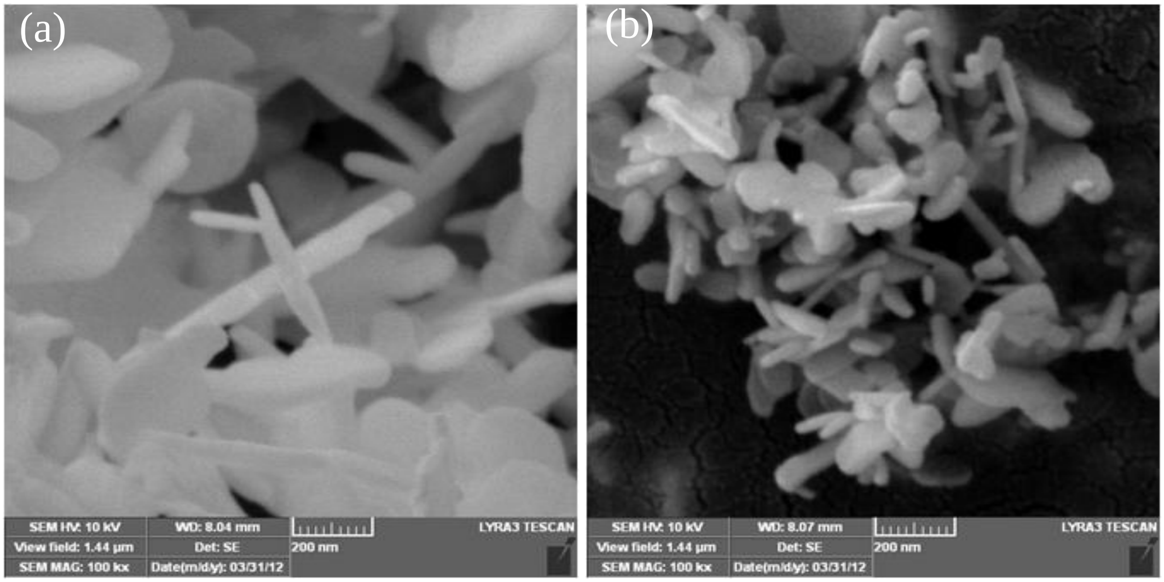

Fig. 5.20. FESEM image of highly magnified area of Bi_2O_3 powder synthesized at (a) 2L/min and (b) 14L/min flow rates of He and a fixed synthesis temperature of 1000°C.

The chemical composision of the product was performed by Energy Dispersive X-ray Spectroscopy (EDS) analysis (EDX detector, Model OXFORD, X-Max). The EDS spectra of Bi_2O_3 nano-powder synthesized at synthesis temperature 1000 °C and N_2 of flow rate 6L/min, Ar of flow rate 6L/min and He of flow rate 14L/min are shown in Fig. 5.21.(a), Fig. 5.21.(b) and Fig. 5.21.(c), respectively. Each spectrum indicates that the product contains only Bi and O. The other peaks in each spectrum correspond to C, Cu that come from the copper tape used in the sample holder and Au peaks originated from the Au coating that was used to avoid charging.

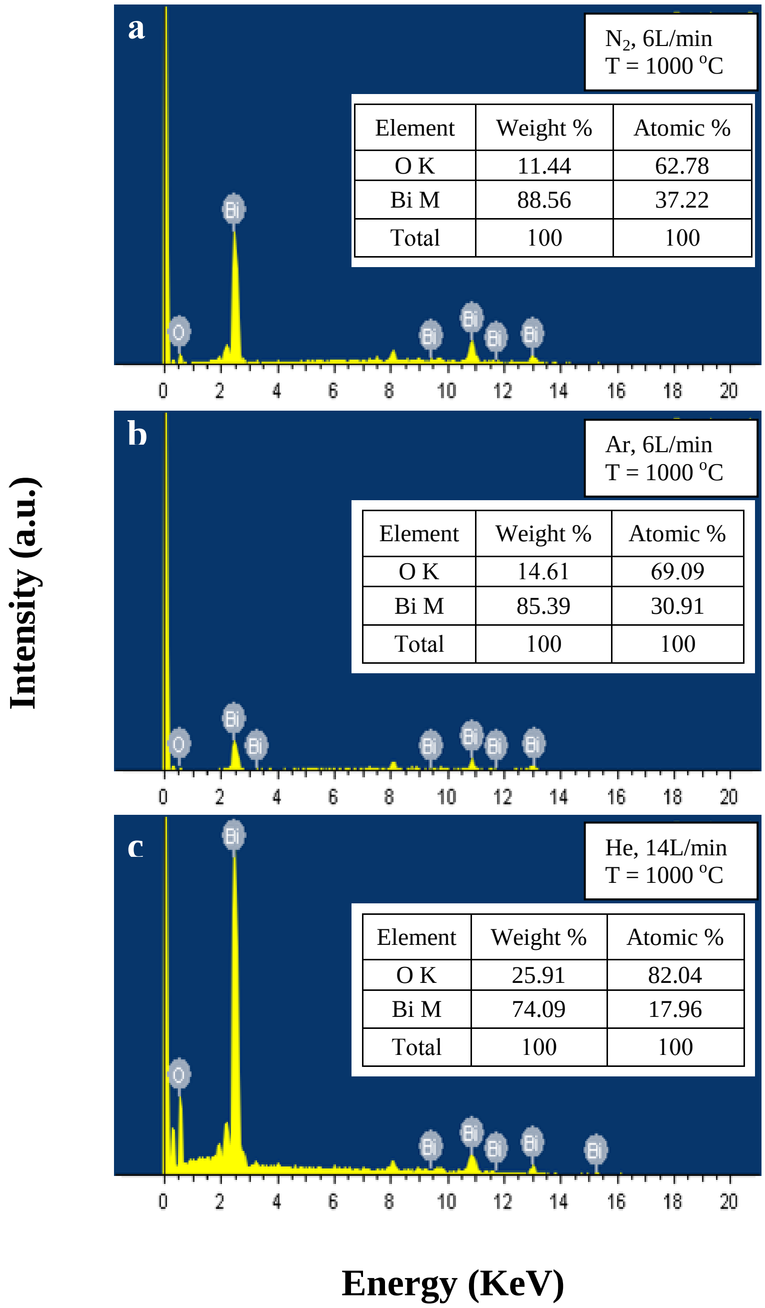

Element	Weight %	Atomic %
O K	11.44	62.78
Bi M	88.56	37.22
Total	100	100

Element	Weight %	Atomic %
O K	14.61	69.09
Bi M	85.39	30.91
Total	100	100

Element	Weight %	Atomic %
O K	25.91	82.04
Bi M	74.09	17.96
Total	100	100

Fig. 5.21. EDS spectra of Bi_2O_3 powder produced at a fixed synthesis temperature of 1000°C, N_2 flow rate of 6L/min (a), Ar flow rate of 6L/min (b) and He flow rate of 14L/min (c).

5.4. Chemical analysis

To investigate the main constituents of the product, three representative samples were studied by XPS technique. These three samples were prepared at a synthesis temperature of 1000 °C and different carrier gases, N_2 of flow rate 2L/min, Ar of flow rate 2L/min and He of flow rate 4 L/min. The XPS survey of these samples was performed for a wide binding energy (BE) range (0-1200 eV) as shown in Figs. 5.22, 5.23, and 5.24, respectively.

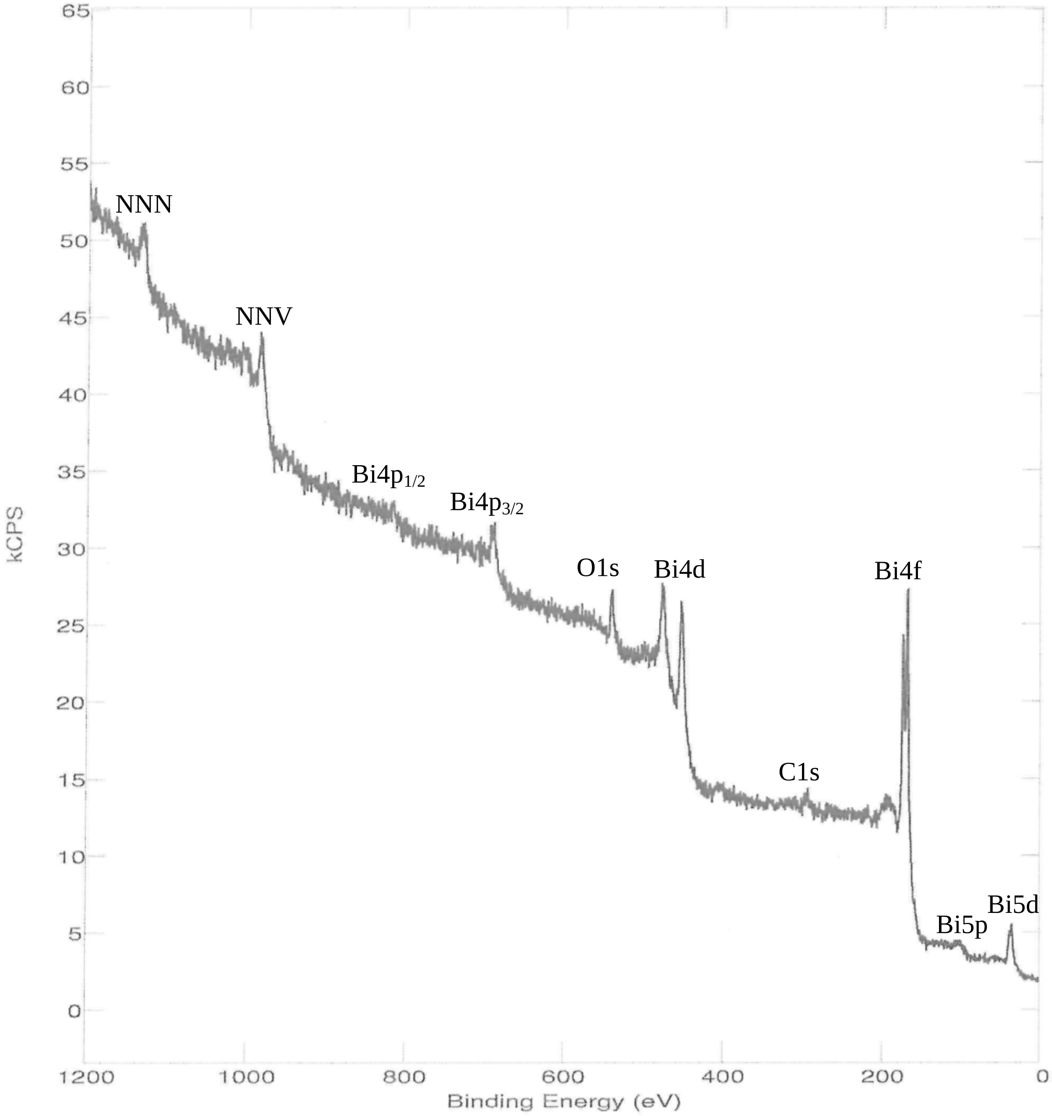

Fig. 5.22. XPS survey for the surface of Bi_2O_3 powder prepared at a synthesis temperature of 1000°C in the presence of N_2 of flow rate 2L/min as a carrier gas.

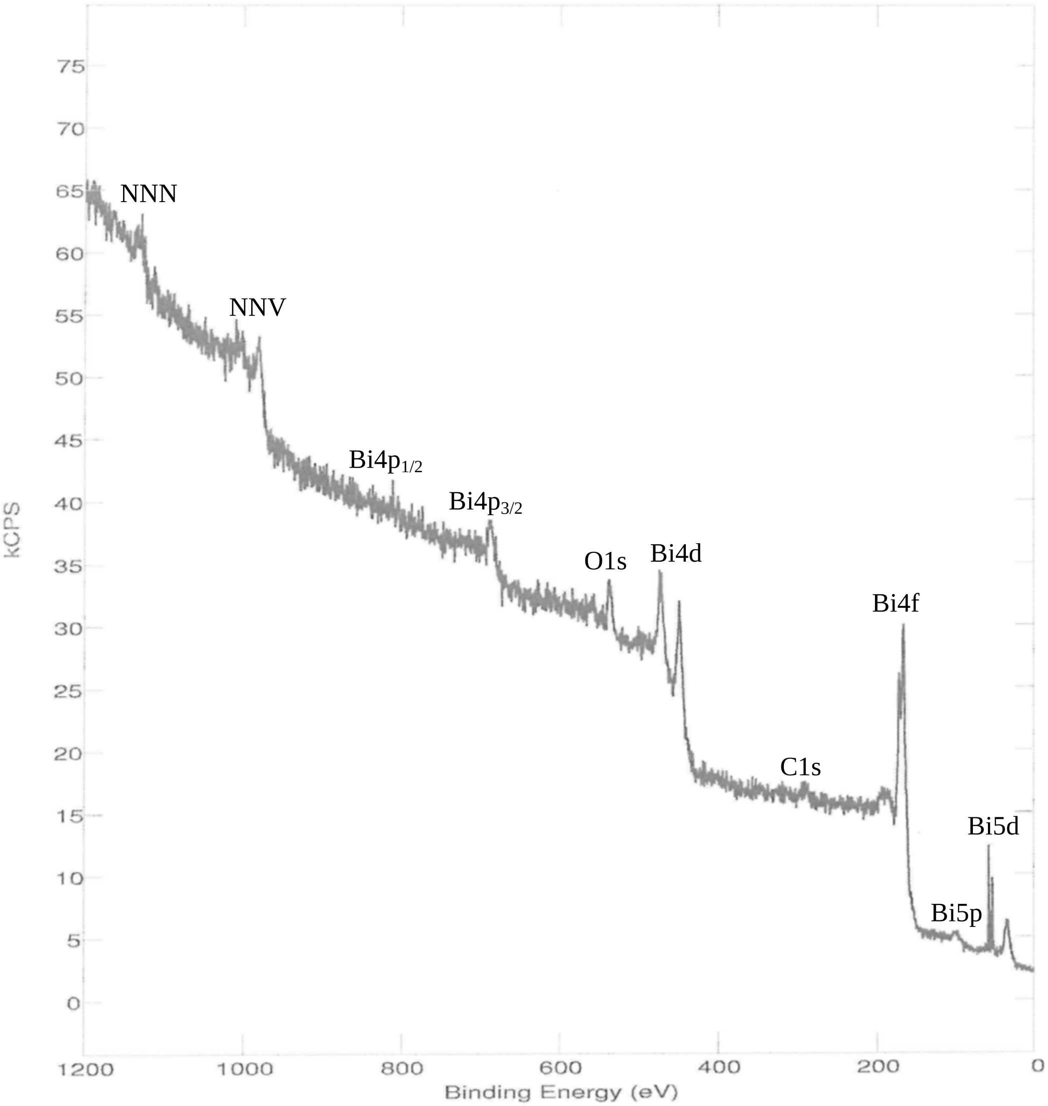

Fig. 5.23. XPS survey for the surface of Bi_2O_3 powder prepared at a synthesis temperature of 1000°C in the presence of Ar of flow rate 2L/min as a carrier gas.

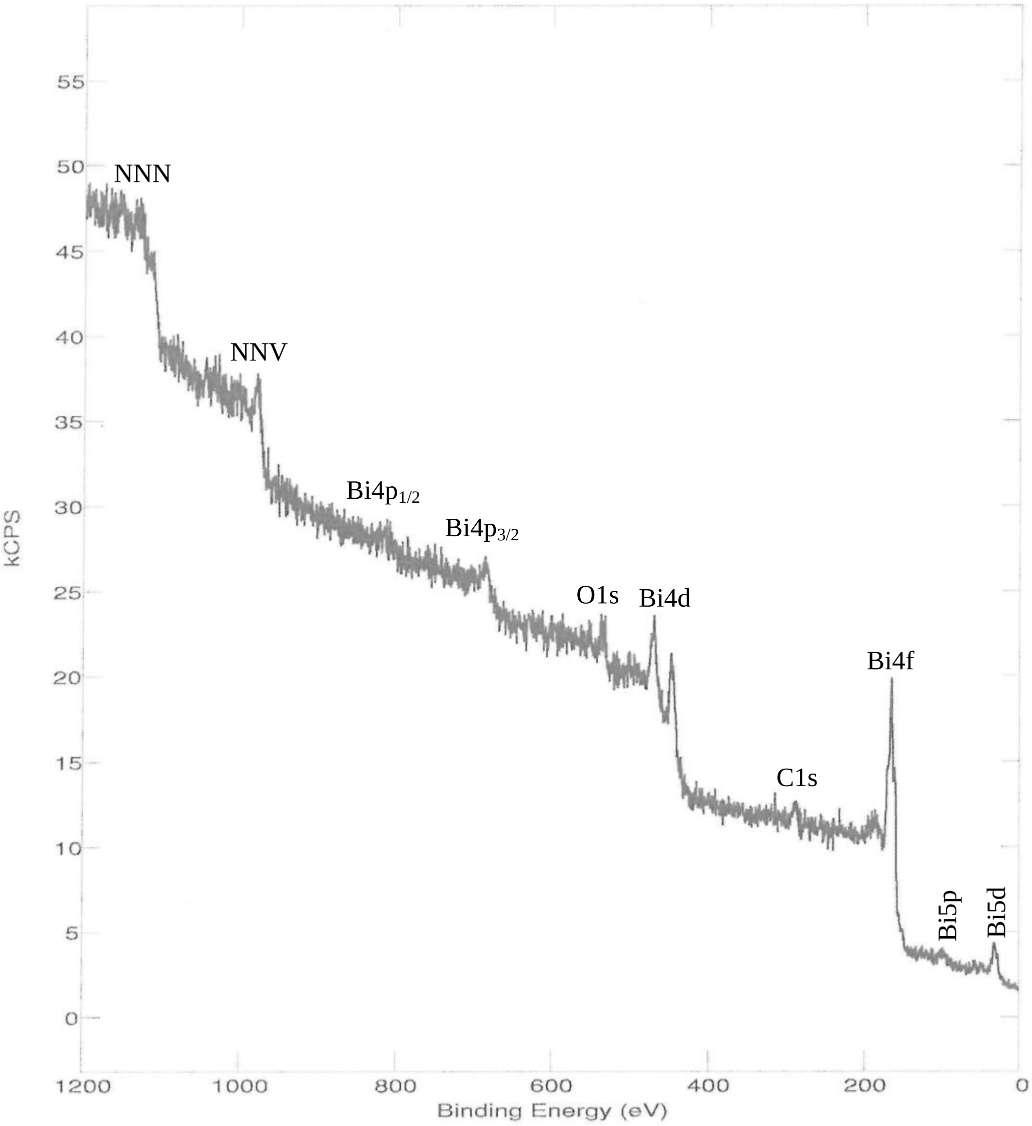

Fig. 5.24. XPS survey for the surface of Bi_2O_3 powder prepared at a synthesis temperature of 1000°C in the presence of He of flow rate 4L/min as a carrier gas.

It can be observed from the above three figures that the constituent elements of the product are Bi and O as well as C that comes from the carbon tape used in the sample holder.

The chemical state of the product was studied by resolution of the Bi4f and O 1s spectra of each sample to their components. The charging shift in the binding energies obtained in the XPS studies were corrected using the C 1s peak at a binding energy of 284.50 eV as a reference for samples prepared using the carrier gases N_2 and Ar while in case of He, the reference was the O 1s peak at a binding energy of 531 eV (because in this sample the C1s peak was not existent). For each sample, the Bi4f spectrum was resolved into four components. For samples synthesized using N_2 as a carrier gas, the $Bi4f_{5/2}$ peak was resolved into two components at binding energies of at 164.41 eV and 161.88 eV, as well as the $Bi4f_{7/2}$ peak at binding energies of 158.54 eV and 156.12 eV, as shown in Fig. 5.25. Similarly for the samples synthesized with Ar as carrier gas, the $Bi4f_{5/2}$ peak was resolved into two components at binding energies of 164.88 eV and 161.08 eV and the $Bi4f_{7/2}$ peak at binding energies of 158.32 eV and 156.17 eV, as shown in Fig. 5.26. In case of He, the two components of $Bi4f_{5/2}$ peak were located at 164.43 eV and 161.83 eV as well as the two components of $Bi4f_{7/2}$ peak at 158.17 eV and 156.20 eV as shown in Fig. 5.27. In all cases, the higher binding energy component in each peak is attributed to Bi-O bond found in Bi_2O_3 [56, 72-76] while the lower binding energy component is due to the other Bi-O bond [72]. It can be concluded that there are no remarkable differences in the binding energy values of $Bi4f_{5/2}$ and $Bi4f_{7/2}$ with the variation of the carrier gas.

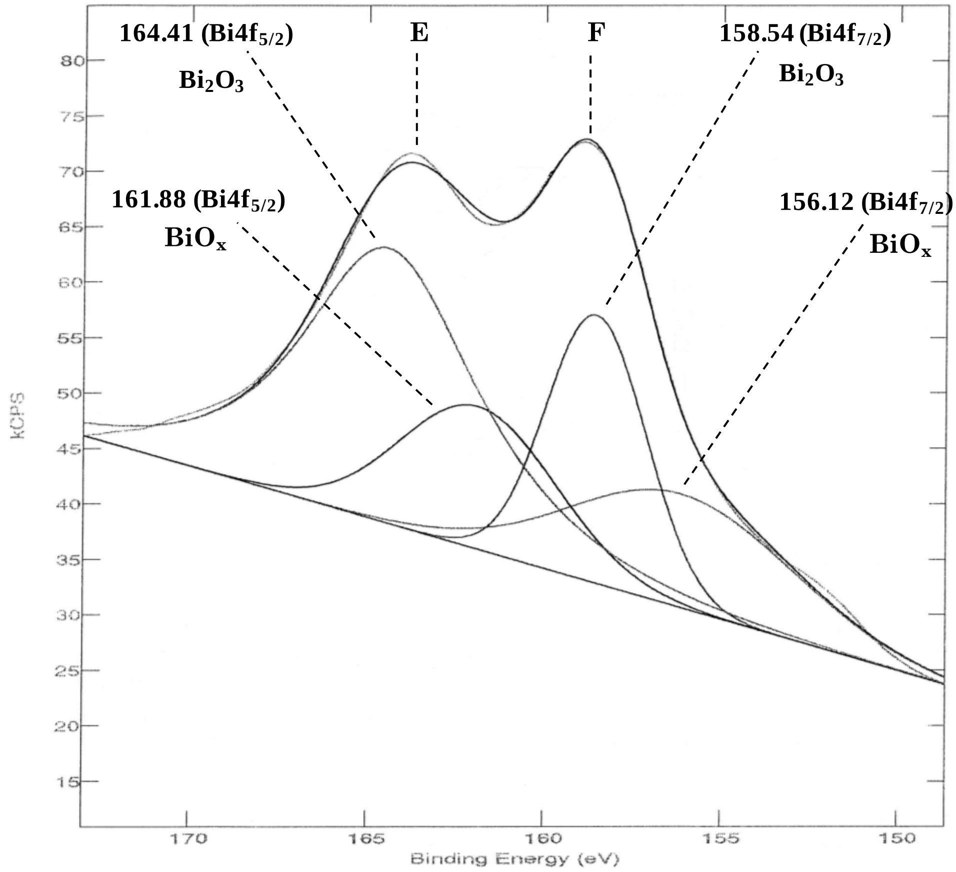

Fig. 5.25. XPS spectrum of Bi4f for Bi_2O_3 powder prepared at a synthesis temperature of 1000°C in the presence of N_2 of flow rate 2L/min as a carrier gas. (E) indicates to the experimental curve which is resolved into four peaks and (F) indicates to the fitting.

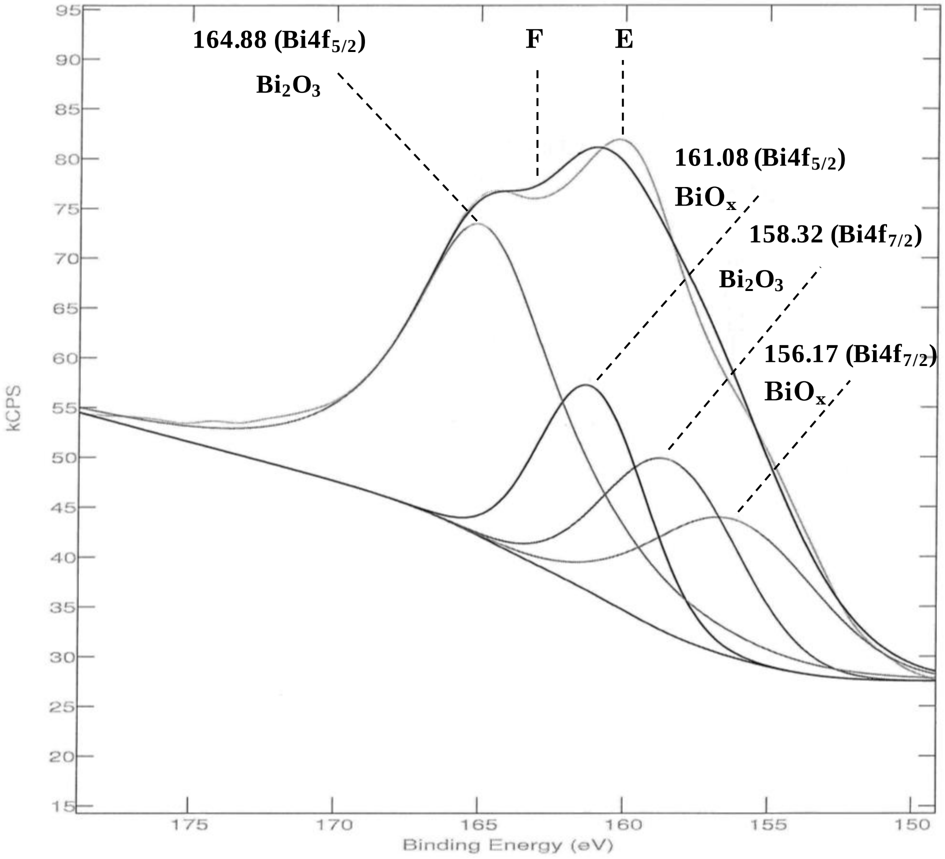

Fig. 5.26. XPS spectrum of Bi4f for Bi_2O_3 powder prepared at a synthesis temperature of 1000°C in the presence of Ar of flow rate 2L/min as a carrier gas. (E) indicates to the experimental curve which is resolved into four peaks and (F) indicates to the fitting.

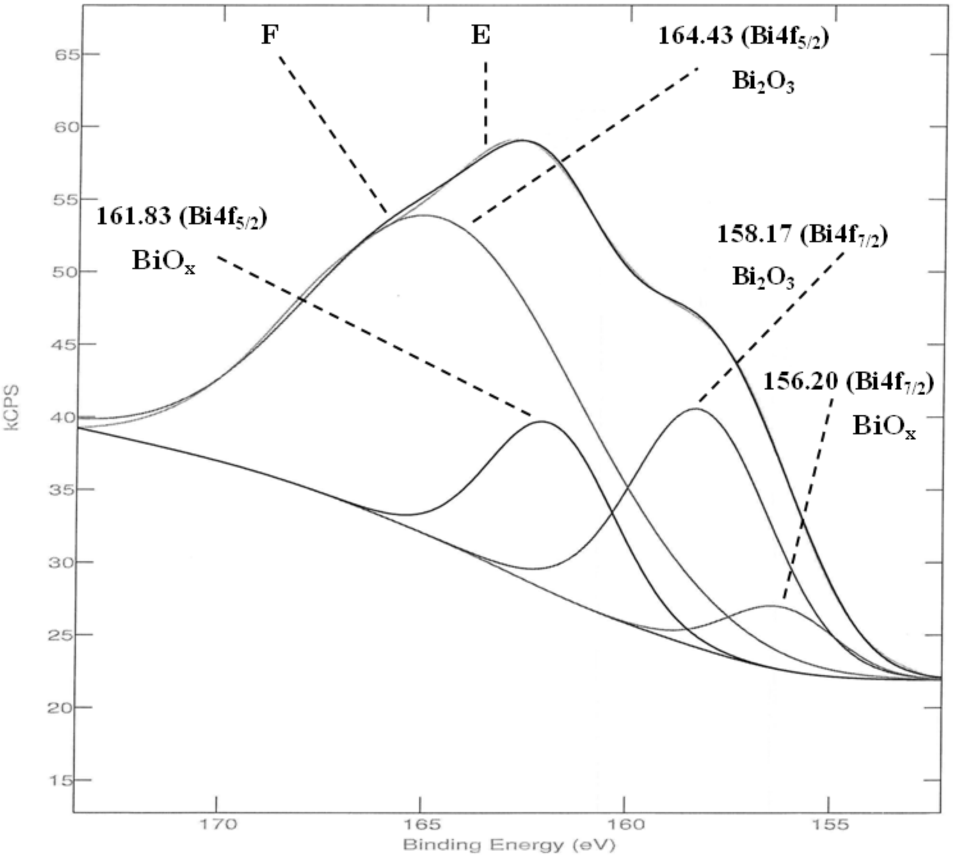

Fig. 5.27. XPS spectrum of Bi4f for Bi_2O_3 powder prepared at a synthesis temperature of 1000°C in the presence of He of flow rate 4L/min as a carrier gas. (E) indicates to the experimental curve which is resolved into four peaks and (F) indicates to the fitting.

We can get an estimate of the stoichiometry of bismuth oxide powder through analysis of Bi4f$_{5/2}$ peaks. The values of BE, full-width at half maximum and weight of each component of Bi4f$_{5/2}$ peak are listed in Table 5.4.

Table 5.4. Resolved Bi4f$_{5/2}$ peaks of bismuth oxide powders prepared at a synthesis temperature of 1000°C and different flow rates of N_2, Ar and He.

Carrier gas	Bi4f$_{5/2}$							
	C1				C2			
	BE (eV)	*Γ* (eV)	Area	*f*	*BE* (eV)	*Γ* (eV)	Area	*f*
N_2 (2L/min)	164.41	5.98	157030	0.69	161.88	5.20	70721.4	0.31
Ar(2L/min)	164.88	6.31	234462	0.71	161.08	4.30	94542.1	0.29
He(4L/min)	164.43	8.09	181867	0.80	161.83	3.61	44466.9	0.20

BE is the binding energy, Γ is the full-width at half maximum and *f* is the weight or percentage of a component to the total peak and C stands for the component.

The formation of bismuth oxide was also confirmed by resolving the O1s peaks of each sample. Fig. 5.28 shows the resolution of O1s peak into three components located at binding energies, 529.11 eV, 525.52 eV and 522.42 eV in the case of N_2. The higher binding energy component (529.11 eV) close to that previously reported results [77], which is attributed to O^{-2} of bismuth oxide and the other two peaks are of unknown origin. In the case of Ar, the higher binding energy component that corresponds to O^{-2} of bismuth oxide was shifted to higher value located at 530.51 eV as shown in Fig. 5.29. The two peaks located at lower binding energies, 526.97 eV and 524.52 eV are also of unknown origin. Finally, the O1s binding energy components in case of He (Fig. 5.30) are located at 531.92 eV, 530.52 eV and 527.67 eV. The first component may be attributed to oxygen incorporated into the samples from atmospheric moisture whereas the second is attributable to O^{-2} of bismuth oxide [56, 73] and the other is unknown.

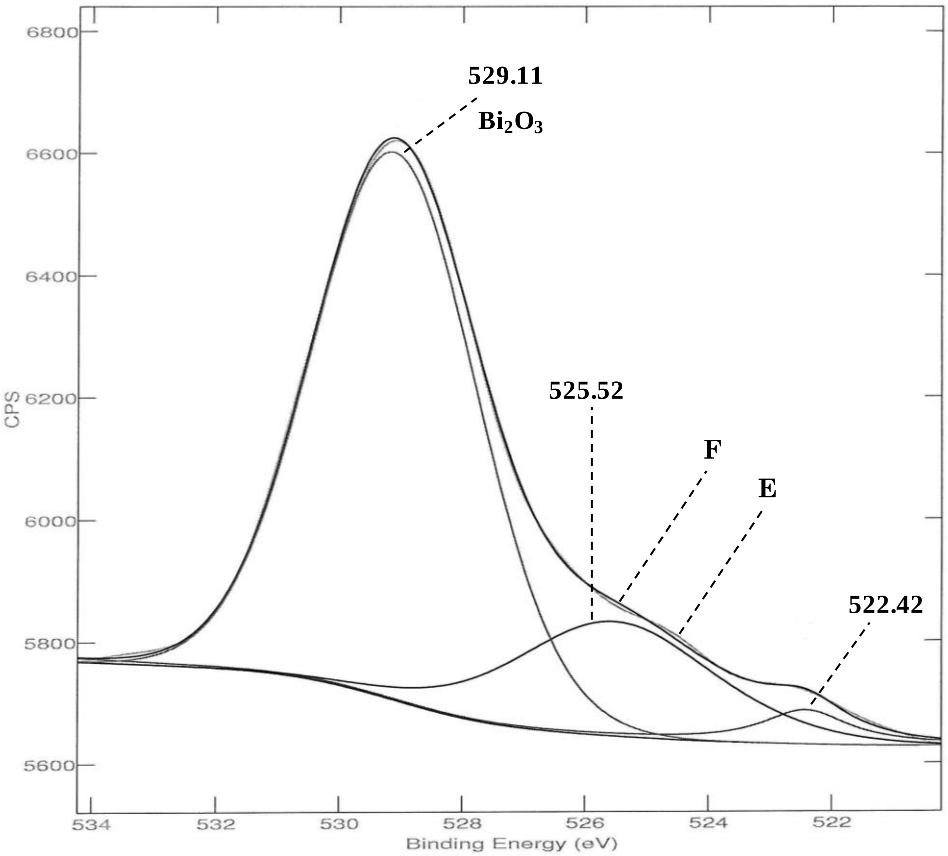

Fig. 5.28. XPS spectrum of O1s region for Bi_2O_3 powder prepared at a synthesis temperature of 1000°C in the presence of N_2 of flow rate 2L/min as a carrier gas. (E) indicates to the experimental curve which is deconvoluted into three peaks and (F) indicates to the fitting.

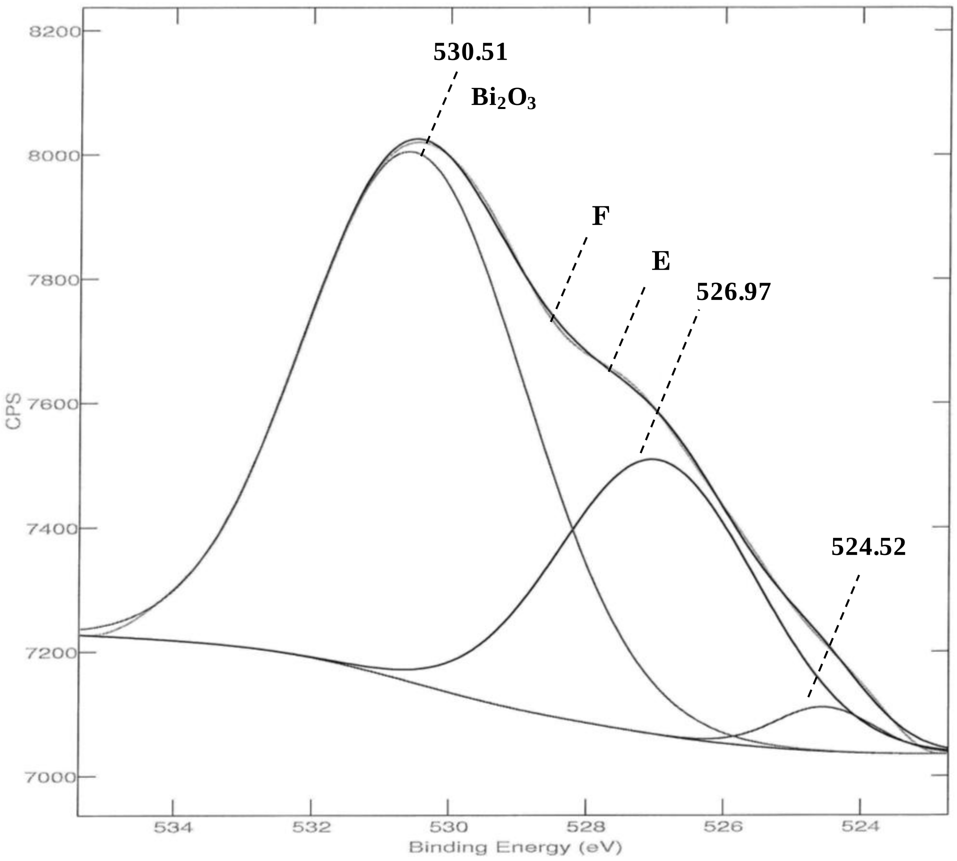

Fig. 5.29. XPS spectrum of O1s region for Bi_2O_3 powder prepared at a synthesis temperature of 1000°C in the presence of Ar of flow rate 2L/min as a carrier gas. (E) indicates to the experimental curve which is resolved into three peaks and (F) indicates to the fitting.

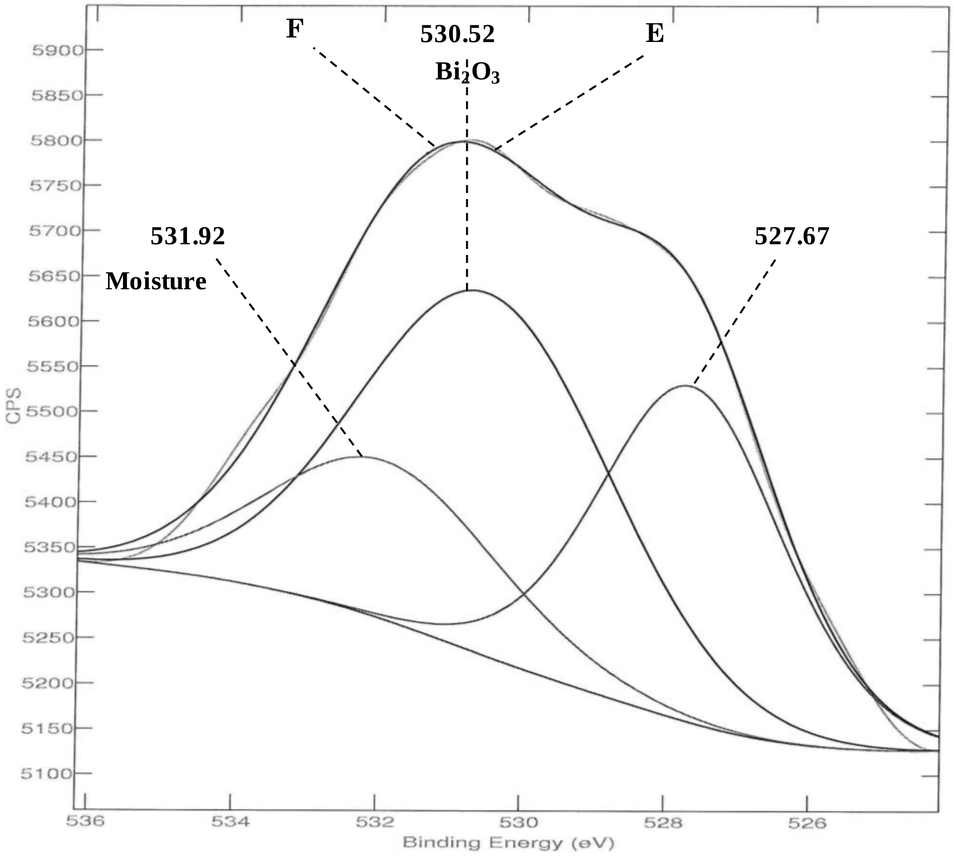

Fig. 5.30. XPS spectrum of O1s region for Bi_2O_3 powder prepared at a synthesis temperature of 1000°C in the presence of He of flow rate 4L/min as a carrier gas. (E) indicates to the experimental curve which is resolved into three peaks and (F) indicates to the fitting.

CONCLUSION

In summary, a modified domestic microwave oven and especially designed SiC composite microwave heater were used for synthesizing metal oxide nanoparticles. Bismuth oxide powder was synthesized via this setup and the effects of different experimental parameters such as synthesis temperature, carrier gases, namely; nitrogen, argon and helium, and flow rates of these carrier gases on the structural, optical, morphological and chemical properties of the as-synthesized bismuth oxide nano-powders were investigated.

It was found that the synthesized powders are of predominantly polycrystalline β-Bi_2O_3 phase and α- Bi_2O_3 phase as inferred from the XRD results. The ratio of the two phases varies with the variation of synthesis parameters. The prepared powder had average crystallite sizes in the range of 19 - 86 nm, 25 - 175 nm and 18 - 133 nm for the cases when nitrogen, argon and helium, were used as carrier gases respectively. These results showed that the average crystallite size decreases with the increase in the flow rate of each type of the carrier gas. The optical properties of the synthesized Bi_2O_3 powder were investigated and their optical gaps were estimated to be in the range of 3.38 - 3.67 eV, 3.29 - 3.65 e V and 3.25 - 3.64 eV for the casees when the carrier gases were N_2, Ar and He, respectively. The estimated band gap values of the Bi_2O_3 powders increases with the increase of the carrier gas flow rate. This is consistent with the idea that the crystallite size of the Bi_2O_3 particles is decreased with the increase in the flow rate of the carrier gas.

The formation of plate-like Bi_2O_3 powders was observed in the samples prepared at a fixed synthesis temperature of 1000°C and flow rates of N_2 (2 and 6L/min), Ar (2 and 6L/min), and He (2 and 14L/min).

On other hand, the purity of product was confirmed by EDS analysis which showed that the synthesized Bi_2O_3 nano-powder contains only Bi and O. Finally, XPS surface analysis revealed that Bi_2O_3 was obtained. The results showed that no considerable effect for the type and flow rate of the carrier gas on the binding energies of the components of the product yield.

REFERENCES

1. E. Gazit, Plenty of room for biology at the bottom: an introduction to bionanotechnology, Imperial Collage Press, London (2007).

2. J. Pelley, M. Saner, International approaches to the regulatory governance of nanotechnology, Regulatory Governance Initiative, Carleton University, Canada (2009).

3. K. E. Drexler, Engines of creation: The coming era of nanotechnology, published by Anchor press, New York (1986) and K. E. Drexler: Molecular machinery and manufacturing with applications to computation, MIT PhD thesis, Wiley, New York (1991).

4. G. Cao, Nanostructures & nanomaterials: synthesis, properties and applications, Imperial Collage Press, London (2004).

5. Ph. Buffat, J-P. Bore1, Size effect on the melting temperature of gold particles, Physical Review A, 13/6 (1976) 2287.

6. W. W. Gerberich, W. M. Mook, C. R. Perrey, C. B. Carter, M. I. Baskes, R. Mukherjee, A. Gidwani, J. Heberlein, P. H. McMurry, S. L. Girshick, Superhard silicon nanospheres, Journal of the Mechanics and Physics of Solids, 51 (2003) 979.

7. J. A. Eastman, U. S. Choi, S. Li, L. J. Thompson, S. Lee, Enhanced thermal conductivity through the development of nanofulids, Materials Research Society Symposium - Proceedings, 457 (1997) 3.

8. A. I. Gusev, A. A. Rempel, Nanocrystalline materials, Cambridge International Science Publishing (2004).

9. M. J. Pitkethy, Nanoparticles as building blocks, Materials Today, 6 (2003) 36.

10. F. C. Krebs, Fabrication and processing of polymer solar cells: A review of printing and coating techniques, Solar Energy Materials & Solar Cells, 93 (2009) 394.

11. M. T. Swihart, Vapor-phase synthesis of nanoparticles, Current Opinion in Colloid and Interface Science, 8 (2003) 127.

12. J. Will, A. Mitterdorfer, C. Kleinlogel, D. Perednis, L. J. Gauckler, Fabrication of thin electrolytes for second-generation solid oxide fuel cells, Solid State Ionics, 131 (2000) 79.

13. A. J. Salazar-Pérez , M. A. Camacho-López, R. A. Morales-Luckie, V. Sánchez-Mendieta, F. Ureña-Núñez, J. Arenas-Alatorre, Structural evolution of Bi_2O_3 prepared by thermal oxidation of bismuth nano-particles, Superficies y Vacío, 18/3 (2005) 4.

14. R. H. J. Hannink, A. J. Hill, Nanostructure control of materials, Woodhead publishing Limited, Cambridge, England (2006).

15. B. Günther, A. Kumpmann, Ultrafine oxide powders prepared by inert gas evaporation, Nanostructured Materials, 1 (1992) 27.

16. S. Terauchi, N. Koshizaki, H. Umehara, Fabriacation of Au nanoparticles by radio-frequency magnetron sputtering, Nanostructured Materials, 5/1 (1995) 71.

17. H. Hahn, Gas phase synthesis of nanocrystalline materials, Nanostructured Materials, 9 (1997) 3.

18. D. Vollath, Nanomaterials: an introduction to synthesis, properties and application, WILEY-VCH Verlag GmbH & Co. KGaA, Weinheim (2008).

19. N. E. Leadbeater, Microwave heating as a tool for sustainable chemistry, CRC Press, Taylor & Francis Group, LLC, New York (2011).

20. National Materials Advisory Board, National Research Council, Microwave processing of materials, Publication NMAB-473 National Academy Press, Washington, USA (1994).

21. D. E. Clark, D. C. Folz, J. K. West, Processing materials with microwave energy, Materials Science and Engineering A, 287 (2000) 153.

22. K. A. Malinger, K. Laubernds, Y-C. Son, S. L. Suib, Effects of microwave processing on chemical, physical, and catalytic properties of todorokite-type manganese oxide, Chem. Mater., 16 (2004) 4296.

23. L. Kumari, J-H. Lin, Y-R. Ma, Synthesis of bismuth oxide nanostructures by an oxidative metal vapour phase deposition technique, Nanotechnology, 18 (2007) 295605.

24. N. Cornei, N. Tancret, F. Abraham, O. Mentré, New ϵ-Bi_2O_3 Metastable Polymorph, Inorganic Chemistry, 45 (2006) 4886.

25. P. Shuk, H. D. Wiemhöfer, U. Guth, W. Göpel, M. Greenblatt, Oxide ion conducting solid electrolytes based on Bi_2O_3, Solid State Ionics, 89 (1996) 179.

26. L. Leonite, M. Caraman, M. Alexe, C. Harnagea, Structural and optical characteristics of bismuth oxide thin films, Surface Science, 507-510 (2002) 480.

27. V. Fruth, M. Popa, D. Berger , R. Ramer, M. Gartner , A. Ciulei, M. Zaharescu, Deposition and characterization of bismuth oxide thin films, Journal of the European Ceramic Society, 25 (2005) 2171.

28. H. T. Fan, X. M. Teng, S. S. Pan, C. Ye, G. H. Li, L. D. Zhang, Optical properties of δ- Bi_2O_3 thin films grown by reactive sputtering, Applied Physics Letters, 87 (2005) 231916.

29. R. L. Thayer, C. A. Randall, S. Trolier-McKinstry, Medium permittivity bismuth zinc niobate thin film capacitors, Journal of Applied Physics, 94/3 (2003) 1941.

30. N. M. Sammes, G. A. Tompsett, H. Näfe, F. Aldinger, Bismuth based oxide electrolytes - structure and ionic conductivity, Journal of the European Ceramic Society, 19 (1999) 1801.

31. L. Leonite, M. Caraman, G. I. Rusu, On the photoconductivity of Bi_2O_3 in thin films, Journal of Optoelectronics Advanced Materials, 2/4 (2000) 385.

32. E. Kanazawa, G. Sakai, K. Shimanoe, Y. Kanmura, Y. Teraoka, N. Miura, N. Yamazoe, Metal oxide semiconductor N_2O sensor for medical use, Sensors and Actuators B, 77 (2001) 72.

33. P. M. Sirimanne, K. Takahashi, N. Sonoyama, T. Sakata, Photocurrent enhancement of wide band gap Bi_2O_3 by Bi_2S_3 over layers, Solar Energy Materials & Solar Cells, 73 (2002) 175.

34. A. Pan, A. Ghosh, A new family of lead-bismuthate glass with a large transmitting window, Journal of Non-Crystalline Solids, 271 (2000) 157.

35. E. N. Voskresenskaya, L. I. Kurteeva, A. G. Anshits, Solid solutions of bismuth oxide as promising catalysts for oxidative coupling of methane, Applied Catalysis A: General, 90 (1992) 209.

36. A. P. Finlayson, E. Ward, V. N. Tsaneva, B. A. Glowacki, Bi_2O_3-WO_3 compounds for photocatalytic applications by solid state and viscous processing, Journal of Power Sources, 145 (2005) 667.

37. S. Park, H. Kim, C. Lee, Synthesis of very straight bismuth oxide nanowires by using thermal evaporation of bismuth powders, Journal of Korean Physical Society, 53/4 (2008) 1965.

38. S-N. Ding, D. Shan, H-G. Xue, S. Cosnier, A promising biosensing-platform based on bismuth oxide polycrystalline-modified electrode: characterization and its application in development of amperometric glucose sensor, Bioelectrochemistry, 79 (2010) 218.

39. MSDS Number B3456.

40. J. Kersten, E. Lombard, C. Carlier, Protection barrier against ionizing rays of the γ type and/or x-rays – United state patent 5,059,807 (1991).

41. L. Miersch, T. Rüffer, H. Lang, S. Schulze, M. Hietschold, D. Zahn, M. Mehring, A novel water-soluble hexanuclear bismuth oxido cluster – synthesis, structure and complexation with polyacrylate, European Journal of Inorganic Chemistry, (2010) 4763.

42. B. G. Hardy, C. Hagen, G. Ferguson, D. J. V. Norman, X-ray detection of the presence and/or condition of polymer components, United State Patent 0255511 A1, (2006).

43. T. P. Gujar , V. R. Shinde , C. D. Lokhande , S-H. Han, Fibrous nanorod network of bismuth oxide by chemical method, Materials Science and Engineering B, 133 (2006) 177.

44. W. Dong, C. Zhu, Optical properties of surface-modified Bi_2O_3 nanoparticles, Journal of Physics and Chemistry of Solids, 64 (2003) 265.

45. L. Kumari, J-H. Lin, Y-R. Ma, One-dimensional Bi_2O_3 nanohooks: synthesis, characterization and optical properties, Journal of Physics: Condensed Matter, 19 (2007) 406204.

46. H. W. Kim, J. H. Myung, S. H. Shim, One-dimensional structures of Bi_2O_3 synthesized via metalorganic chemical vapor deposition process, Solid State Communications, 137 (2006) 196.

47. S. Anandan, J. J. Wu, Microwave assisted rapid synthesis of Bi_2O_3 short nanorods, Materials Letters, 63 (2009) 2387.

48. Al-Quraishi, Method for synthesizing metal oxide, United State Patent 7, 601, 324 B1 (2009).

49. L. Mädler, S. E. Pratsinis, Bismuth oxide nanoparticles by flame spray pyrolysis, J. Am. Ceram. Soc., 85/7 (2002) 1713.

50. W. Li, Facile synthesis of monodisperse Bi_2O_3 nanoparticles, Materials Chemistry and Physics, 99 (2006) 174.

51. M. Anilkumar, R. Pasricha, V. Ravi, Synthesis of bismuth oxide nanoparticles by citrate gel method, Ceramics International, 31 (2005) 889.

52. F. I. López-Salinas, G. A. Martínez-Castañón, J. R. Martínez-Mendoza, F. Ruiz, Synthesis and characterization of nanostructured powders of Bi_2O_3, BiOCl and Bi, Materials Letters, 64 (2010) 1555.

53. X-P. Shen, S-K. Wu, H. Zhao, Q. Liu, Synthesis of single-crystalline Bi_2O_3 nanowires by atmospheric pressure chemical vapor deposition approach, Physica E, 39 (2007) 133.

54. G. Lin, D. Tan, F. Luo, D. Chen, Q. Zhao, J. Qiu, Z. Xu, Fabrication and photocatalytic property of α-Bi_2O_3 nanoparticles by femtosecond laser ablation in liquid, Journal of Alloys and Compounds, 507 (2010) L43.

55. M. Chakrabarti, S. Dutta, S. Chttapadhyay, A. Sarkar, D. Sanyal, A, Chakrabarti, Grain size dependence of optical properties and positron annihilation parameters in Bi_2O_3 powder, Nanotechnology, 15 (2004) 1792.

56. H. Cheng, B. Huang, J. Lu, Z. Wang, B. Xu, X. Qin, X. Zhang, Y. Dai, Synergistic effect of crystal and electronic structures on the visible-light-driven photocatalytic performances of Bi_2O_3 polymorphs, Physical Chemistry Chemical Physics, 12 (2010) 15468.

57. L. Liu, J. Jiang, S. Jin, Z. Xia, M. Tang, Hydrothermal synthesis of β-bismuth oxide nanowires from particles, Crystal Engineering Community, 13 (2011) 2529.

58. H. W. Kim, J. W. Lee, C. Lee, Temperature-controlled fabrication of crystalline β-Bi_2O_3 nanowires through an MOCVD process, Journal of the Korean Physical Society, 50/5 (2007) 1308.

59. L. Zhang, W. Wang, J. Yang, Z. Chen, W. Zhang, L. Zhou, S. Liu, Sonochemical synthesis of nanocrystallite Bi_2O_3 as a visible-light-driven photocatalyst, Applied Catalysis A: General, 308 (2006) 105.

60. Y. Wang, J. Zhao, Z. Wang, A simple low-temperature fabrication of oblique prism-like bismuth oxide via a one-step aqueous process, Colloids and Surfaces A: Physicochemical and Engineering Aaspects, 377 (2011) 409.

61. C. Suryanarayana, M. G. Norton, X-ray diffraction: a practical approach, Plenum Press, New York (1998).

62. B. R. Rehani, P. B. Joshi, K. N. Lad, A. Pratap, Crystallite size estimation of elemental and composite silver nano-powders using XRD principles, Indian Journal of Pure & Applied Physics, 44 (2006) 157.

63. J. C. Vickerman, I. S. Gilmore, Surface analysis - the principal techniques, 2nd Edition, John Wiley & Sons, Ltd., UK (2009).

64. R. W. Kelsall, I. W. Hamley, M. Geoghegan, Nanoscale science and technology, John Wiley & Sons, Ltd., England (2005).

65. I. F. Ferguson, Auger microprobe analysis, published under the Adam Hilger Imprint by IOP Publishing Ltd., England (1989).

66. A. E. Morales, E. S´. Mora, U. Pal, Use of diffuse reflectance spectroscopy for optical characterization of un-supported nanostructures, Revista Mexicana de Física S, 53/5 (2007) 18.

67. ICDD files: (00-027-0050 and 01-074-2351) for β-Bi_2O_3 and (01-072-0398, 00-002-0988 and 00-014-0699) for α-Bi_2O_3.

68. E. Leslie, Sparks, M. J. Pilat, Effect of diffusiophoresis on particle collection by wet scrubbers, Atmospheric Environment Pergamon Press, 4 (1970) 651.

69. S. M. A. Durrani, E. E. Khawaja, M. A. Salim, M. F. Al-Kuhaili, A. M. Al-Shukri, Effect of preparation conditions on the optical and thermochromic properties of thin films of tungsten oxide, Solar Energy Materials & Solar Cells, 71 (2002) 313.

70. S. Condurache-Bota, G. I. Rusu, N. Tigau, R. Drasovean, C. Gheorghies, Structural and optical characterization of thermally oxidized bismuth films, Revue Roumaine de Chimie, 54/3 (2009) 205.

71. K. Brezesinski, R. Ostermann, P. Hartmann, J. Perlich, T. Brezesinski, Exceptional photocatalytic activity of ordered mesoporous β-Bi_2O_3 thin films and electrospun nanofiber mats, Chem. Mater., 22 (2010) 3079.

72. E. Husson, J. M. Bény, C. Proust, R. Benoit, R. Erre, Y. Vaills, K. Belkhader, Raman and Brillouin scattering and XPS spectroscopy in $NaPb_{0.5}Bi_{0.33}PO_4$ glass - Evolution as a function of temperature, Journal of Non-Crystalline Solids, 238 (1998) 66.

73. Y. Dai, Y. Wang, J. Yao, Q. Wang, L. Liu, W. Chu, G. Wang, Phosgene-free synthesis of phenyl isocyanate by catalytic decomposition of methyl N-phenyl carbamate over Bi_2O_3 catalyst, Catal. Lett., 123 (2008) 307.

74. C. Wang, C. Shao, L. Wang, L. Zhang, X. Li, Y. Liu, Electrospinning preparation, characterization and photocatalytic properties of Bi_2O_3 nanofibers, Journal of Colloid and Interface Science, 333 (2009) 242.

75. D. Barreca, F. Morazzoni, G. A. Rizzi, R. Scotti, E. Tondello, Molecular oxygen interaction with Bi_2O_3: a spectroscopic and spectromagnetic investigation, Phys. Chem. Chem. Phys., 3 (2001) 1743.

76. V. Simon, M. Todea, A. F. Takács, M. Neumann, S. Simon, XPS study on silica–bismuthate glasses and glass ceramics, Solid State Communications, 141 (2007) 42.

77. H. Bando, K. Koizumi, Y. Oikawa, K. Daikohara, V. A. Kulbachinskii, H. Ozaki, The time-dependent process of oxidation of the surface of Bi_2Te_3 studied by x-ray photoelectron spectroscopy, J. Phys.: Condens. Matter, 12 (2000) 5607.

VITA

Full Name:	Abdulmajeed Hasan Yahya Hendi
Place & date of Birth:	Hajja, Yemen, 1975
Nationality:	Yemeni
Present address:	Physics Department, King Fahd University of Petroleum & Minerals, Dhahran 31261, Saudi Arabia
Permanent address:	Hajja University, Physics Department, Hajja, R. O. Yemen
Email:	abutsneem@yahoo.com

Education:

- Master of Science in Physics from King Fahd University of Petroleum & Minerals, Saudi Arabia, April 2012
- Bachelor of Education in Physics from Sana’a University, Yemen, June 1998

Position held:

- Graduate assistant at Physics department, Sana’a University, Yemen, (2000-2006)

Conference Publication:

- **Abdul Majeed H. Yahya**, “*Synthesis and Characterization of Bismuth Oxide Nano-Powder produced by Microwave-assisted Combustion Method*”, **Second Scientific Conference**, Jeddah, Saudi Arabia, 28-31 March 2011